

ADVERTIMENT. La consulta d'aquesta tesi queda condicionada a l'acceptació de les següents condicions d'ús: La difusió d'aquesta tesi per mitjà del servei TDX (www.tesisenxarxa.net) ha estat autoritzada pels titulars dels drets de propietat intel·lectual únicament per a usos privats emmarcats en activitats d'investigació i docència. No s'autoritza la seva reproducció amb finalitats de lucre ni la seva difusió i posada a disposició des d'un lloc aliè al servei TDX. No s'autoritza la presentació del seu contingut en una finestra o marc aliè a TDX (framing). Aquesta reserva de drets afecta tant al resum de presentació de la tesi com als seus continguts. En la utilització o cita de parts de la tesi és obligat indicar el nom de la persona autora.

ADVERTENCIA. La consulta de esta tesis queda condicionada a la aceptación de las siguientes condiciones de uso: La difusión de esta tesis por medio del servicio TDR (www.tesisenred.net) ha sido autorizada por los titulares de los derechos de propiedad intelectual únicamente para usos privados enmarcados en actividades de investigación y docencia. No se autoriza su reproducción con finalidades de lucro ni su difusión y puesta a disposición desde un sitio ajeno al servicio TDR. No se autoriza la presentación de su contenido en una ventana o marco ajeno a TDR (framing). Esta reserva de derechos afecta tanto al resumen de presentación de la tesis como a sus contenidos. En la utilización o cita de partes de la tesis es obligado indicar el nombre de la persona autora.

WARNING. On having consulted this thesis you're accepting the following use conditions: Spreading this thesis by the TDX (www.tesisenxarxa.net) service has been authorized by the titular of the intellectual property rights only for private uses placed in investigation and teaching activities. Reproduction with lucrative aims is not authorized neither its spreading and availability from a site foreign to the TDX service. Introducing its content in a window or frame foreign to the TDX service is not authorized (framing). This rights affect to the presentation summary of the thesis as well as to its contents. In the using or citation of parts of the thesis it's obliged to indicate the name of the author

UNIVERSITAT POLITÈCNICA DE CATALUNYA
DEPARTAMENT DE FÍSICA APLICADA

MONTE CARLO SIMULATIONS
OF THE POPULATION OF
SINGLE AND BINARY WHITE DWARFS
IN OUR GALAXY

BY

MARIA JUDITH CAMACHO DÍAZ

A THESIS SUBMITTED FOR THE DEGREE OF DOCTOR OF
PHILOSOPHY

ADVISORS:

ENRIQUE GARCÍA-BERRO MONTILLA
SANTIAGO TORRES GIL

Castelldefels, Enero de 2014

I know that it will happen,
'cause I believe in the certainty of chance.

The Divine Comedy (1998)

Dedicated to my parents

*We have seen that computer programming is an art,
because it applies accumulated knowledge to the world,
because it requires skill and ingenuity, and especially
because it produces objects of beauty.*

Knuth (1974)

Acknowledgments

The research conducted in this dissertation is part of a team effort carried out by Enrique García-Berro, Santiago Torres, Alberto Rebassa-Mansergas, Matthias R. Schreiber, Boris T. Gänsicke, Monica Zorotovic, Ada Nebot, Leandro Althaus, Jordi Isern and myself. This thesis is a summary of my individual research while working within this team framework. In parts along this thesis I refer to work being done individually as “we” instead of “I” because without the dedication and contribution of the entire team the individual research presented would not have been possible.

First and foremost, I wish to express my sincere gratitude towards my advisors, Enrique García-Berro and Santiago Torres, for their prompt action in leading me to go full-steam ahead with my project and paddle my own canoe. I hope that the piece of work presented in this thesis made them be proud of me, not to mention the fact this brings justice to the trust they placed on me.

I would also like to acknowledge Toni Castillo and Jordi Lino, computer technicians of the BarcelonaTech (UPC), for their helpful advise in all kind of computer problems and, above all, for their patience with me.

Part of my research is fruit of an international collaboration, which for me has been an enriching experience. Because my project called for observational data, we contacted Matthias Schreiber who led an international project aimed at the detection of Galactic binary systems. Most of these observations were done at the European Southern Observatory, in Chile. This particular project is based on follow-up observations of the Sloan Digital Sky Survey (SDSS), which is one of the most challenging observational programs carried out so far.

Part of my work has been developed in Chile, during a week in 2010 and just over three months in 2011. I wish to acknowledge all the staff members of the Department of Physics and Astronomy at Valparaíso University. Thanks to them I quickly settled down and got into the swings of things. Special acknowledgments go

to the director of the department, Víctor Cardenas, and my guardian and leading investigator, Matthias Schreiber. Also, particular thanks to the following faculty: Moira Evans Treurnicht, Jura Borissova, Radostin Kurtev, Claus Tappert, Michel Curé, Nikolaus Vogt, and Osvaldo Herrera. On top of that, I would like to thank my research colleagues who bristled with confidence: Alberto Rebassa-Mansergas and Monica Zorotovic. By the same token, thanks are due to post-graduated students: Alexander Bonilla, Gisela Andrea Romero, James Clarke, Stuart Folkes, Stuart Sale Samer Kanaan and Luis Vega, and all their respective wives, husbands and fiancées, with whom I got a bang of them. I can say that I have been endowed with a worldwide network of friends. I cherish Professor Dr. Martin Gaskell who embodies the best moral values and is involved in volunteering poverty projects in Chile, he deserves my veneration and I wish to blow his own trumpet. I really remember our talks about science and religion which made spice things up.

I was tickled pink that Spanish Chilean community invited me to celebrate with them a happy occasion, the Day of Asturias. There I met Sigfrid Grimau, president of the Centre Català of Chile (<http://www.centrecatala.cl>), alongside other Chilean people of Catalan descents, with whom I had the dinner of my life.

I would like to thank to the Consul General of Chile in Barcelona for their rush processing service at my student visa, as well as answering back with a smile in all my inquires.

The thing is that setting foot in Chile marked a turning point in my life. Hardly had I arrived at Chile, it was stripped away any picture-postcard illusions that I expected from the most developed country of south America. Devoid of employment, youngsters succumb into misery. A growing unrest among students triggered in successive strikes to demand a free and public education. The thought that was sprung to my mind is that we European students gravitate in the abundance begot by the economic growth, comfortably cocooned ourselves. By rights children should be endowed with wall-to-wall health care and an education of quality. My mind boggles at the idea that such essentials are deprived indeed. I am glad to have joined to the cause and contribute my bit to spread awareness of ethical issues and what needs to be changed. This international collaboration has enriched my personal experience, enhancing both interpersonal and social skills, as well as it has nurtured knowledge-sharing and enhanced my critical thinking. I can really feel the buzz of having growth because all of this. I hope this telling experiences encourage more international scholarly collaborations. Not to mention the fact that this sparks debate over the standardization of the educational system derived of the global economic crisis that hits below the pale.

I appreciate the financial support from the Ministry of Education and Science of Spain (MEC), through the grants AYA05-08013-C03-01, AYA05-08013-C03-02, AYA08-04211-C02-01 and AYA08-1839/ESP, as well as the European Union FEDER funds, the Agency for Management of University and Research Grants (AGAUR), the ESF EUROGENESIS project, the Spanish Agency of International Cooperation

(AECI) grant A/023687/09, and the Fondecyt through the grant number 3110049. This financial support covered not only publishing expenses, but also partially travel and subsistence expenses to enable the exchange of researchers.

I also would like to thank to the anonymous journal referees that offered me some really interesting, insightful observations, as well as the members of my reading committee for supporting my thesis.

Finally, I am very grateful to have been blessed with a loving, supportive family. They always have encouraged me to do what float my boat, for them the sky is the limit to what I can do!

DREAMING

*I flew like a bird into the dark space,
gazing and gazing
a streak of Moon light.
There fluttering I could see some leaves,
it looked like drizzling.
I felt dazzled and stunned by the outstanding view.
A shoot of light led me back to my bed.*

Poem written by me for my English Poetry class in February, 2010.

Contents

Outline and research target	v
List of Figures	ix
List of Tables	xi
1 Introduction: the essentials of white dwarfs	1
1.1 A historical perspective	1
1.2 General properties of single white dwarfs	4
1.2.1 Spectroscopic classification	4
1.2.2 Distribution in effective temperatures	7
1.2.3 Metallicity content of white dwarfs	9
1.3 Mass distribution	10
1.4 The white dwarf luminosity function	11
1.4.1 Definition, estimators and completeness	11
1.4.2 The thick and the halo white dwarf luminosity functions . . .	13
1.5 White dwarfs as dark matter	14
1.6 White dwarfs in close binary systems	16
2 Building the sample	19
2.1 The Monte Carlo method	19
2.2 The population of gravitational microlenses	21
2.2.1 The halo model	21
2.2.2 Modeling the microlensing events towards the LMC	23
2.3 Monte Carlo simulations of the binary population	25
2.3.1 Inputs for the binary population	25
2.3.2 Treatment of the common envelope phase	27
2.3.3 Photometric magnitudes	29
3 The contribution of oxygen–neon white dwarfs	31
3.1 Introduction	31
3.2 Observational results	32

3.3	Results and discussion	32
3.3.1	The halo white dwarf luminosity function	32
3.3.2	Optical depth towards the LMC	34
3.3.3	The Hubble Deep Field South	39
3.3.4	The dark matter density	40
3.4	Conclusions	42
4	The contribution of red dwarfs and white dwarfs	43
4.1	Introduction	43
4.2	Expanding the model	44
4.3	Results and discussion	44
4.3.1	Optical depth towards the LMC	44
4.3.2	The microlensing event rate	51
4.3.3	The EROS experiment	53
4.3.4	The dark matter density	54
4.4	Conclusions	55
5	White dwarfs with hydrogen-deficient atmospheres	57
5.1	Introduction	57
5.2	Building the model	59
5.2.1	The fraction of DA and non-DA white dwarfs	60
5.2.2	The thick disk model	61
5.3	Results and discussion	62
5.3.1	The optical depth towards the LMC	62
5.3.2	The EROS experiment	66
5.3.3	The thick disk contribution	69
5.3.4	The event rate distribution	73
5.3.5	The joint contribution of the thick disk and halo populations	75
5.3.6	Halo dark matter	76
5.4	Conclusions	77
6	Monte Carlo simulations of the WD+MS population in the SDSS	79
6.1	Introduction	79
6.2	The simulated population of WD+MS PCEBs	81
6.2.1	Color cuts	81
6.2.2	Spectroscopic completeness	84
6.2.3	Intrinsic WD+MS binary bias	85
6.2.4	PCEB orbital period filter	86
6.3	Results	87
6.3.1	The observational sample	87
6.3.2	Overview of the simulations	87
6.3.3	Color-color space	88

6.3.4	The effects of biases and selection criteria	89
6.3.5	The role of the enhanced mass-loss parameter	91
6.3.6	The effects of the binding energy parameter	92
6.3.7	The fraction of PCEBs containing He white dwarfs	94
6.3.8	The period distribution	95
6.3.9	Period-mass distribution	99
6.4	Summary and conclusions	100
7	Conclusions	105
7.1	Gravitational microlensing and halo dark matter	105
7.1.1	The contribution of oxygen-neon white dwarfs	105
7.1.2	The contribution of halo red dwarfs	106
7.1.3	The contribution of hydrogen-deficient white dwarfs	107
7.1.4	Summary	108
7.2	White dwarf-main sequence binaries in the SDSS-DR7	108
A	Schmidt's estimator	111
	Bibliography	113

Outline and research target

Due to the fact that white dwarfs are the final stage of the evolution of the vast majority of stars, they carry important information about the chemical evolution of our Galaxy, its star formation rate, and its structure and dynamics. This thesis pays attention to two related but distinct astrophysical problems involving white dwarfs.

The first of these problems concerns the nature of the microlensing events towards the Large Magellanic Cloud (LMC), which still remains a mystery. The main observational groups, MACHO and EROS, are in dispute each other, yet agreement has now been accomplished in some of the most important points. For instance, no microlensing candidates were found by the MACHO team or the EROS group, with event durations between a few hours and 20 days. This implies that the Galactic halo can contain no more than a 10% of dark objects in the mass range $10^{-7} < M/M_{\odot} < 10^{-3}$. This rules out planets and brown dwarfs as the major contributors to the mass budget of the dark halo. Moreover, the MACHO collaboration detected ~ 15 microlensing events during their 5.7 yr analysis of 11.9 million stars in the LMC (Alcock et al., 2000). In their works, they derived an optical depth towards the LMC of $\tau = 1.2^{+0.4}_{-0.3} \times 10^{-7}$ or, equivalently, a halo fraction $0.08 < f < 0.50$, at the 95% confidence level, with a MACHO mass in the range $0.15 \leq M/M_{\odot} \leq 0.50$, depending on the halo model. On the other hand, the non-detections reported by the EROS collaboration provided an upper limit. The EROS team presented an analysis of a sub-sample of bright stars belonging to the LMC (Tisserand et al., 2007), to minimize source confusion and blending effects. Their findings imply that the optical depth towards the LMC was $\tau < 0.36 \times 10^{-7}$ at the 95% confidence level, corresponding to a fraction of the halo mass of less than 7%. This result was 4 times smaller than that obtained by the MACHO team. These findings stimulated the discussion about the location and nature of the lenses. In particular, LMC models were used to ascertain if possible asymmetries in the space distribution of the microlensed stars could be related to Galactic halo objects or LMC ones. In fact, different studies indicate that a sizeable fraction of the microlensed events are due to LMC self-lensing (Sahu, 1994; Gyuk, Dalal & Griest, 2000; Calchi Novati, de Luca, Jetzer & Scarpetta, 2006). Moreover, a full variety of possible explanations were proposed to reproduce the microlensing events: tidal debris or a dwarf galaxy toward the LMC (Zhao, 1998), a Galactic-extended shroud population of

white dwarfs (Gates & Gyuk 2001), blending effects (Belokurov et al., 2003, 2004), spatially-varying mass-functions (Kerins & Evans, 1998; Rahvar, 2005), and other explanations (Holopainen et al., 2006). However, all of these proposals were received with some criticism because none of them fully explains the observed microlensing results.

Other observational pieces of evidence were added to help resolve the present puzzle, such as the search for very faint objects in the Hubble Deep Field or the search for the microlensing events towards the Galactic bulge or towards very crowded fields such as M31. In particular, the Hubble Deep Field provided an opportunity to test the contribution of white dwarfs to the Galactic dark matter content. Ibata et al. (1999) and Kilic et al. (2005) claimed the detection of some white dwarf candidates among several faint blue objects. These objects exhibit significant proper motion and are, accordingly, assumed to belong to the thick disk or the halo populations. Another controversial issue which deserves attention is whether the lenses belong to the halo or to an extended thick disk population (Reid et al., 2001; Torres et al., 2002). After all, and as pointed out by Gyuk & Gates (1999), the thick disk population presents a reasonable alternative to a halo population of lenses. Several observational (Oppenheimer et al., 2001; Kilic et al., 2006; Harris et al., 2006; Vidrih et al., 2007) works have addressed this question, and a definitive answer still requires more theoretical and observational efforts.

The second of the problems we address in this work is an open problem as well. Close compact binaries are at the heart of several interesting phenomena in our Galaxy and in other galaxies. In particular, cataclysmic variables, low mass X-ray binaries or double degenerate white dwarf binaries — just to mention the most important and well-studied ones — are systems that not only deserve attention by themselves, but also because their statistical distributions are crucial to understand the underlying physics of the evolution during a common envelope episode. Actually, the vast majority of close compact binaries are formed through at least one common envelope episode. This phase occurs when the more massive star in a binary system fills its Roche lobe during its evolution, and can happen either when the primary is on the first giant branch or when it climbs the asymptotic giant branch. Depending on the orbital parameters of the binary system, the mass transfer episode can be unstable, the envelope of the giant star engulfs the secondary, and a common envelope forms. Once the common envelope is formed around both the core of the primary (the future compact star) and the secondary stars, drag forces transfer orbital energy and angular momentum from the orbit to the envelope, leading to a dramatic decrease of the orbital separation, and to ejection of the common envelope. For a suitable range of orbital parameters, the outcome of this sequence of events is a post-common envelope binary (PCEB), formed by a white dwarf (the degenerate core of the primary) and a main-sequence companion, with an orbital separation much smaller than that of the original binary system.

Even though the basic concepts of the evolution during a common envelope phase

are rather simple, the details are still far from being well understood. This is so because several complex physical processes play an important role in the evolution during the common envelope phase. For instance, the spiral-in of the core of the primary and of the secondary, and the ejection of the envelope are not only a consequence of the evolution of the core and remaining layers of the donor star in response to rapid mass loss, but also tidal forces and viscous dissipation in the common envelope play key roles. Moreover, these physical processes occur on very different timescales and on a wide range of physical scales — see Taam & Ricker (2010) for a recent review. Consequently, a self-consistent modeling of the common envelope phase requires detailed hydrodynamical models which are not available at the present time, although recent progresses are encouraging — see Ricker & Taam (2012) and references therein. Hence, the common envelope evolution has been traditionally described using parametrized models.

To shed light on these problems, we will use an existing Monte Carlo simulator thoroughly described in Torres Gil (2002). This Monte Carlo simulator has been already used to obtain insight in our understanding of the population of single white dwarfs of the Galactic disk (García-Berro et al., 1999; Torres et al., 2001), as well as on that of the halo population (Torres et al., 1998, 2002; García-Berro et al., 2004). We will expand this simulator integrating the most up-to-date white dwarf cooling models as well as a detailed modeling of our Galaxy and the LMC and SMC in order to mimic both the MACHO and EROS experiments. However, it is important to mention that not only white dwarfs are candidates to be stellar lenses but also are red dwarfs, given that these objects have masses in the range of the lens mass detected by the MACHOs survey. Because of this we will include the red dwarf population and perform a joint analysis of the contributions of both populations to the dark matter content of our Galaxy. Moreover, we will study the contribution of the sub-population of white dwarfs with hydrogen-deficient atmospheres. White dwarfs with hydrogen-deficient atmospheres cool down faster than their counterparts with hydrogen-rich atmospheres and, consequently, it is expected that these white dwarfs will increment the contribution to the total number of microlenses. This calculation has not been done up to now and represents a new step in our understanding of the microlensing experiments.

On the other hand, we will build a Monte Carlo simulator of the binary population of the Galactic disk. In particular, our Monte Carlo code has been expanded to deal with those systems composed by a white dwarf and a main sequence star which have evolved through a common envelope phase. In order to carry on the modeling of this scenario a detailed implementation of several different physical processes is needed. Among these physical inputs we mention a full description of the mass transfer episode, a complete treatment of the Roche lobe overflow episode, gravitational tiding and orbital evolution of the binary system. Moreover, in our treatment we will carefully include all the different selection criteria and observational biases. This will allow us to make a meaningful comparison with the available observational data,

allowing us to examine the role played by the binding energy parameter and by the common envelope efficiency parameter, as well as the role played by the distribution of secondary masses of the binary system.

This thesis is organized as follows. In the first chapter we present a general overview of the main properties of white dwarfs. The second chapter is devoted to explain our Monte Carlo simulator. In particular, in this chapter, the basic ingredients employed to build the samples of both the single and binary populations of white dwarfs are described at length. For the sake of completeness a description of the gravitational microlensing experiments is also included in this chapter. In chapters 3, 4 and 5, we present the results concerning the gravitational microlensing experiments. In particular, in chapter 3 we expand a previous analysis of the population of carbon-oxygen white dwarfs and we incorporate the halo population of white dwarfs with oxygen-neon cores. In chapter 4 we study the role of the halo population of red dwarfs. Specifically, we analyze the contribution of these stars to the microlensing event rates. It is worth mentioning here that the joint modeling of the red dwarf and the white dwarf populations is a novel approach, which implies a more robust analysis of the contribution of these populations to the dark matter content of our Galaxy. Finally, in chapter 5 we study the contribution to the halo dark matter content of the white dwarf population with hydrogen-deficient atmospheres. In this chapter we take into account not only the halo population, but we also incorporate a detailed description of the thick disk population. In chapter 6 we present our results of a study of post-common envelope binaries formed by a white dwarf and a main sequence star. Our simulated samples are then compared with the observational data obtained from the SDSS-DR7 survey, and a comprehensive statistical analysis is presented. Thus, a full treatment of all the observational selection criteria and their possible biases is implemented. As it will be seen later, this analysis will allow us to obtain very valuable information regarding the common envelope phase and will allow to constrain the values of the different parameters involved in the theoretical models. Finally, in chapter 7 we summarize our main results and we draw our conclusions.

List of Figures

3.1	Luminosity function of halo white dwarfs for a standard initial mass function (left panel) and a biased initial mass function (right panel). The observational luminosity function of halo white dwarfs is represented using a dotted line (Torres et al., 1998) and solid triangles, while the theoretical luminosity function is shown using a solid line and squares. See text for details.	33
3.2	Microlensing optical depth towards the LMC as a function of the limiting magnitude. Open and solid symbols represent the population of white dwarfs without and with the contribution of the ONe white dwarfs, respectively. The solid symbols have been shifted for the sake of clarity.	34
3.3	Fraction of microlenses due to ONe white dwarfs with respect to the whole population of white dwarfs for the standard initial mass function — squares — and for the log-normal initial mass function of Adams & Laughlin (1996) — triangles.	37
3.4	Color-magnitude diagram for the white dwarf distribution (ONe white dwarfs are circled) for the HDF-S of two typical simulations. The dashed line represents the HDF-S observational limit. Also represented is the average expected location within 1σ error of a typical ONe white dwarf. See text for details.	40
4.1	Microlensing optical depth towards the LMC as a function of the limiting magnitude. Solid and open squares represent the CO and ONe white dwarf populations, respectively. Red dwarfs are represented using open triangles, while the entire population is shown using open circles.	45
4.2	Contribution to the optical depth as a function of the lens mass. . .	49
4.3	Fraction of microlenses with respect to the entire population. . . .	50

4.4	Differential event rate normalized to unit area as a function of the Einstein crossing-time for the populations under study and different magnitude cuts (solid lines). The observational event distribution from Alcock et al. (2000) is represented as a dotted line in each panel.	52
4.5	Halo dark matter fraction as a function of the mass lens. We plot using a solid line the 95% confidence-level curve for the MACHO experiment and the 95% confidence-level upper-limit for the EROS experiment.	55
5.1	Color-magnitude diagram of a typical $0.6 M_{\odot}$ white dwarf. The solid line corresponds to a cooling sequence of a hydrogen-rich (DA) white dwarf (Salaris et al., 2000), while the dashed line corresponds to a helium-rich (non-DA) white dwarf (Benvenuto & Althaus, 1997). The dots correspond to cooling ages of 6, 8, 10, 12 and 14 Gyr.	58
5.2	Microlensing optical depth towards the LMC as a function of the limiting magnitude. Solid and open squares represent the DA and non-DA white dwarf populations, respectively. Red dwarfs are represented by open triangles, while the entire population is shown by open circles.	63
5.3	Proper motion as a function of the V magnitude for the halo white dwarf population. The EROS selection zone is shown as a bold solid line.	68
5.4	Microlensing optical depth towards the LMC as a function of the limiting magnitude for the thick disk population. Solid and open squares represent the DA and non-DA white dwarf populations, respectively. Red dwarfs are represented by open triangles, while the entire population is shown by open circles.	71
5.5	Normalized distributions of the microlensing event rate as a function of the event duration for the different population under study (solid lines) and also for the observed microlensing events of the MACHO experiment (dashed lines). All the distributions have been computed for a magnitude cut of 22.5^{mag}	74
6.1	Position of Legacy (black) and SEGUE (red) SDSS DR7 WD+MS binaries in Galactic and equatorial coordinates. Taken from Rebassa-Mansergas et al. (2012).	82
6.2	Detection probability of a PCEB as a function of the orbital period.	86

6.3	Color-color diagram of the synthetic WD+MS PCEBs obtained using our Monte Carlo simulator when our reference model ($\alpha_{\text{CE}} = 1.0$, $\lambda = 0.5$, and $n(q) = 1$) is employed. Systems containing He white dwarfs are represented using black dots, while light blue dots correspond to systems with carbon-oxygen or oxygen-neon white dwarfs. The observed WD+MS PCEB systems are displayed using red dots. The color selection criteria are shown using red lines (Sect. 6.2.1).	88
6.4	Color-magnitude diagram of the synthetic WD+MS PCEBs obtained using our Monte Carlo simulator (light blue and black dots) compared with the observational systems (red symbols) after applying the different filters explained in the text to our reference model. Colors are the same as in Fig. 6.3.	90
6.5	From top to bottom: binding energy parameter, primary ZAMS mass, white dwarf mass and orbital period as a function of the Roche-lobe radius. The case B, case C and TPAGB case common envelope episodes are represented using green, blue and red dots, respectively. We show the results for a model in which $\alpha_{\text{CE}} = 0.3$, $n(q) = 1$ and without fraction of the internal energy contributing to expel the envelope ($\alpha_{\text{int}} = 0.0$).	93
6.6	Same as Fig. 6.5, but for a model in which $\alpha_{\text{int}} = 0.2$, being the rest of the parameters the same.	94
6.7	Period histograms (normalized to unit area) of the distribution of present-day WD+MS PCEBs for our four best models (black line) compared with the observational distribution (dotted line, gray histogram).	96
6.8	Period-mass density distribution of present-day WDMS systems for our best model with $n(q) = 1$ and no internal energy parameter compared with the observational distribution (magenta squares).	101
6.9	Period-mass density distribution of present-day WDMS systems for our best model with $n(q) \propto q$ and non-zero internal energy parameter compared with the observational distribution (magenta squares).	102

List of Tables

1.1	Symbol nomenclature for the white dwarf atmospheric content and spectral characteristics.	5
3.1	Summary of the results obtained for the simulation of microlenses towards the LMC for the MACHO model for an age of the halo of 14 Gyr, different model IMFs, and several magnitude cuts.	35
3.2	Average values for the ONe white dwarf population.	36
3.3	Summary of the results obtained for the simulation of microlenses towards the LMC for the EROS model for an age of the halo of 14 Gyr, different model IMFs, and several magnitude cuts.	38
3.4	Density of baryonic matter (M_{\odot}/pc^3) in the Galactic halo within 300 pc from the Sun in the form gas returned to the interstellar medium (ISM) and in the form of white dwarfs (WD).	41
4.1	Summary of the results obtained for whole population simulation of microlenses towards the LMC for an age of the halo of 14 Gyr, different model initial mass functions, and several magnitude cuts.	46
4.2	Summary of the results obtained for the population of red dwarf microlenses towards the LMC for an age of the halo of 14 Gyr, different model initial mass functions, and several magnitude cuts.	47
4.3	Compatibility, as obtained using the Z^2 statistical test, of the observed MACHO distribution and the different Monte Carlo simulated populations.	53
4.4	Summary of the results obtained for the simulation of microlenses towards the LMC for the EROS experiment for an age of the halo of 14 Gyr, different model initial mass functions, and several magnitude cuts.	54
5.1	Percentages of non-DA white dwarfs and its corresponding cooling tracks for the different simulated models.	60
5.2	Summary of the global properties of the canonical thick disk and metal-weak thick disk models.	61

5.3	Summary of the results obtained for the entire population of microlenses towards the LMC for several magnitude cuts when the results of the MACHO collaboration are simulated. An age of the halo of 14 Gyr has been adopted.	65
5.4	Summary of the results obtained for the entire population of microlenses towards the LMC for the EROS experiment, using models A, B and C and adopting an age of the halo of 14 Gyr and several magnitude cuts.	67
5.5	Summary of the results obtained for the thick disk population of microlenses towards the LMC for the MACHO experiment with a thick disk age of 12 Gyr and several magnitude cuts.	70
5.6	Same as table 3 for the EROS experiment.	72
5.7	Z^2 compatibility test between the Einstein crossing times obtained by the MACHO team and the simulated thick disk and halo populations for different magnitude cuts.	75
5.8	Summary of the results obtained for the thick disk and halo populations of microlenses towards the LMC for the MACHO experiment. .	76
6.1	Total number and percentage of simulated WD+MS binary systems obtained after applying the successive selection criteria.	83
6.2	Enhanced mass-loss parameter and white dwarf percentages.	92
6.3	Percentage of systems with He white dwarfs and Kolmogorov-Smirnov test of the period distribution for six representative models with $\lambda = 0.5$	95
6.4	Percentage of systems with He white dwarfs and Kolmogorov-Smirnov test of the period distribution for our models with $\alpha_{\text{CE}} \leq 0.3$ and λ properly computed for each system, where different fractions of internal energy are taken into account.	98
6.5	Statistics for the best models.	100

Chapter 1

Introduction: the essentials of white dwarfs

1.1 A historical perspective

One of the most spectacular events in nature, planetary nebulae, precedes the birth of a white dwarf. Planetary nebulae are caused by the stripped outer layers of giant stars that form a shell of gas that radiates due to the absorption of the ultraviolet radiation coming from the exposed central star. These cores collapse under the force of gravity and, if the temperature is not enough to ignite new nuclear reactions, a degenerate core is formed. The stellar remnant of this giant stars, composed mostly of electron-degenerate matter, becomes a white dwarf.

The first planetary nebula catalogued was in 1764 by Messier (Kwok, 2000), it followed William Herschel together with his sister Caroline listing many others (Herschel, 1786). And yet, the first discovery of a white dwarf is claim to take place in the year 1783 by William Herschel, who discovered 40 Eridani B, a white dwarf embedded in a triple system (40 Eridani) with two main-sequence stars. The second white-dwarf discovery was Sirius B, belonging to the binary system Sirius. In the year 1844, the astronomer Friedrich Bessel appealed by its bizarre proper motion, it dawned on him the idea that Sirius may be overshadowing an easily darker companion (Bessel, 1844). By that time, the optician Alvin Clark set up a cutting-edge refracting telescope factory producing the largest lenses at that moment. In 1862, while Alvin Clark was testing a telescope built for the University of Mississippi, pointed to Sirius and unmasked it as a binary-star system, as suggested by Bessel. It is worth mentioning that the so-called Clark refractors were prolific in the field of proper motions, discovering many other white dwarfs in multiple systems, as well as in planetary studies.

However, not until the early twentieth century that white dwarfs were well understood. Owing to the development of quantum mechanics, white dwarfs became

the target to test and validate new theories. As mentioned above, white dwarfs are made of degenerate matter — every electron energy level below the Fermi level is occupied. This prevents them from collapsing, and therefore not only is this an evidence but also a demonstration of the Pauli Exclusion Principle for electrons. Soon thereafter, the condition of relativistic degenerate matter came out and whereby lead to the discovery that white dwarfs have other interesting properties, such as an inverse dependence of radius on mass $R \sim M^{-1/3}$ and an upper mass limit $\sim 1.4 M_{\odot}$ — for a non-rotating white dwarf — known as the Chandrasekhar mass limit (Chandrasekhar, 1931, 1933).

The first accurate white dwarf cooling model was computed by Mestel (1952). In this model a white dwarf consists basically of an isothermal electron-degenerate core. This core provides most of the mass, and is made of the ions resulting from the previous nuclear history of the progenitor star. This core is surrounded by a non-degenerate thin envelope ($\lesssim 0.01\%$ of the mass) composed mainly of hydrogen and/or helium. Within this approximation the evolution of a white dwarf can be fairly well described as a gravothermal process of cooling. In typical white dwarfs neither thermonuclear reactions nor the release of gravitational energy play significant roles. Thus, the lingering residual heat of its ion core causes white dwarfs to shine and cool down slowly by a flux controlled by the radiative opacity of the envelope. As a first approximation, Mestel’s model is good enough to describe white dwarfs with luminosities over $L \sim 10^{-3} L_{\odot}$.

The decade of the sixties of the twentieth century brought about a breakthrough in the cooling theory of white dwarfs. It was realized that the material of which white dwarfs are made should undergo a phase transition, and therefore crystallizes. This, in fact, is another example of how quantum mechanics play a key role in the evolution of these stars. Crystallization occurs when white dwarfs reach low effective temperatures (Kirzhnits, 1958; Abrikosov, 1960; Salpeter, 1961; van Horn, 1968). Nowadays, up-to-date white dwarf cooling models incorporate a wide range of physical effects such as gravitational contraction, thermal energy as well as residual nuclear burning, energy losses due to neutrinos, Debye cooling, electron heat capacity, electron conduction, electron-electron scattering, and radiative diffusion among others. Consequently, the cooling of white dwarfs is today relatively well understood and represents a solid and robust age benchmark in astrophysics.

As a consequence of all this, white dwarf cooling ages have been extensively used as age indicators of several stellar populations, namely they have been widely used as cosmochronometers. Not only that, the white dwarf luminosity function provides us with an invaluable wealth of information about the solar neighborhood. Hence, a wide range of Galactic parameters can be obtained from a its detailed study. Among the most important ones we mention the age of the Galaxy (Winget et al. 1987; García-Berro et al. 1988; Hernanz et al. 1994; Richer et al. 2000) and the stellar formation rate (Noh & Scalo 1990; Díaz-Pinto et al. 1994; Isern et al. 1995; Isern et al. 2001). Additionally, the luminosity function of white dwarfs

provides an independent test of the theory of dense plasmas (Segretain et al. 1994; Isern et al. 1997). Finally, the white dwarf luminosity function directly measures the current death rate of low- and intermediate-mass stars in the local disk. In addition, experiments based on gravitational microlensing have suggested that the halo of our Galaxy could be populated of cold, old white dwarfs. Hence, these stars could significantly contribute to the baryonic dark matter of our Galaxy (Adams & Laughlin, 1996; Chabrier et al., 1996; Graff et al., 1998), one of the key issues in modern cosmology.

Moreover, due to the fact that the physical processes that affect the structure of white dwarfs as well as their evolution are fairly well identified and understood, white dwarfs are an excellent complementary laboratory to corroborate alternative physical theories and testing new physics. For example, white dwarfs provide an independent way of testing the possibility of a hypothetical varying gravitational constant (Garcia-Berro et al., 1995). Besides, white dwarfs have been also used to test the existence of weakly interacting particles (Isern et al., 2010). Another interesting point refers to pulsating white dwarfs that jointly with asteroseismological models allow us to probe the structure and composition of the core of these objects (Metcalf, 2005). Finally, white dwarfs in stellar clusters are a benchmark for calibrating, testing and probing the theory of stellar evolution, as well as the evolution of our own Galaxy (Hufnagel, 1995; Kalirai, 2006; Liebert et al., 2005). By observing white dwarfs in star clusters we spectroscopically determine their masses and temperatures that alongside with white dwarf cooling models give us a precise estimate of their cooling ages.

Moreover, the advent of large automated surveys — like the Sloan Digital Sky Survey (York et al. 2000; Stoughton et al. 2002; Abazajian et al. 2003, 2004; Eisenstein et al. 2006), the Two Micron All Sky Survey (Skrutskie et al. 1997; Cutri et al. 2003), the SuperCosmos Sky Survey (Hambly et al. 2001a,b; Hambly, Irwin & MacGillivray 2001c), the 2dF QSO Redshift Survey (Vennes et al. 2002), the SPY project (Pauli et al. 2003), and others — has dramatically increased the number of known white dwarfs. Future astrometric space missions — of which Gaia (Perryman et al. 2001) is the leading example — will undoubtedly increase even more the size of the white dwarf population with accurately determined parameters (Torres et al. 2005), thus allowing for reliable determinations of the white dwarf luminosity function of our Galaxy, and many other interesting studies. Additionally, many planned terrestrial and space-borne observatories will eventually study challenging astrophysical phenomena involving white dwarfs, of which binary white dwarfs are a flagship issue. So far, the Sloan Digital Sky Survey (SDSS) has furnished the largest catalog of both single and binary white dwarfs, Chandra and XMM-Newton have extensively studied X-ray binaries, LIGO and LISA are currently trying to detect the gravitational waves radiated by compact sources, the High-Energy Transient Explorer and the Swift Space Telescope aim to study gamma-ray burst progenitors, while the Spitzer mission has searched for planets orbiting low-mass white dwarfs

(Kilic et al., 2010). Even more, Kepler has revealed the existence of low-mass white dwarfs with A-type stars, sdBs, and regular carbon-oxygen white dwarf companions and it may discover planets orbiting white dwarfs, as well as white dwarfs orbiting main-sequence stars through transits of asteroids or combining these measurements with gravitational lensing (Di Stefano et al., 2010; Di Stefano, 2011). Likewise, Eddington aims to study the variability of accreting white dwarfs (de Martino & Silvotti, 2004) and Gaia (Perryman et al., 1997; Figueras et al., 1999) will catalog more than one billion stars with excellent astrometric, photometric and spectroscopic accuracies. The scientific output of all these missions will undoubtedly have a large impact in our understanding of the theory of cooling white dwarfs.

1.2 General properties of single white dwarfs

1.2.1 Spectroscopic classification

It is a well known fact that the fundamental properties and features of stars — such as the effective temperatures, gravities and chemical compositions of their stellar surfaces, and the bolometric luminosity, rotation velocity, radial velocities and binary orbital motions — can be obtained using spectral measurements of their brightness at different frequencies. Usually, these are collected using charge-coupled devices (CCD) that go hand-in-hand with imaging spectrography, allowing time-resolved spectroscopy and spectrophotometry. On the other hand, in most cases this must be combined with theoretical models to derive useful information.

The white dwarf effective temperature and the surface gravity may be determined by fitting their synthetic spectra, generated by means of model atmosphere codes, to their observed Balmer lines (H_α), which lay in the visible band. However, hydrogen spectral features are most easily detected in the ultraviolet, where the Lyman lines appear, or in the infrared, where the Paschen series happen. Moreover, to obtain a detailed analysis is essential to analyze spectral features of all existing chemical elements. To sum up, a good fitting model has to match the spectral features in the visible, ultraviolet, far and extreme ultraviolet, the infrared and X-ray bands (Kahn et al., 1984; Kowalski & Saumon, 2006; Kowalski et al., 2007). There are two ways to model white dwarf spectra. The first, easiest and straightforward approach considers local thermodynamic equilibrium (LTE). This approach is valid for moderately cool stars, whereas for hot and very hot stars ($T_{\text{eff}} \gtrsim 20\,000\text{ K}$) this approach is no longer valid, and non-LTE modeling is required. The degree of sophistication in the modeling of white dwarf spectra can be very large, as in some particular cases, to successfully match the simulated spectrum to the observed one one has to incorporate stratified models, levitation, diffusion, or the so-called metal-line blanketing. All these physical effects alter the profiles of the Balmer lines — see, for example, Althaus et al. (2009), and Rauch et al. (2010).

The actual white dwarf spectral classification was introduced by Sion et al. (1983).

Type	Atmospheric content and spectral characteristics
H-rich	
DA	H present
DAO	H present, HeII weak
H-deficient	
DO	HeII strong, HeI and/or H present
DB	HeI
DBA	HeI strong, H weak
DQ	Carbon
DZ	Metals
DC	Featureless continuum — no lines deeper than 5 % — (it is required photometric analysis)
Additional	
P	Magnetic with polarization
H	Magnetic, no polarization detectable
E	Emission lines
d	Debris disk
V	Variable star
PEC	Peculiar or unclassifiable spectra

Table 1.1: Symbol nomenclature for the white dwarf atmospheric content and spectral characteristics.

The symbol nomenclature starts by the uppercase letter D, which comes from degenerate star, followed by an assortment of successive letters that denote the main atmospheric composition and weaker or secondary spectral features. In Table 1.1 the primary symbols are listed along with some secondary and additional features. As an example, a DB white dwarf showing traces of hydrogen would be classified as DBA, whereas a white dwarf of the DB type with traces of carbon would be classified as DBQ, and if it has calcium lines or any other metal would be classified as DBZ. Any spectrum depicting emission lines should be represented by the letter E, and so forth.

White dwarfs are often classified in two classes, attending to their atmospheric composition: hydrogen-rich (H-rich) and hydrogen-deficient (H-deficient) white dwarfs. White dwarfs with H-rich atmospheres represent $\sim 85\%$ of the total population (Eisenstein et al., 2006a) and have been traditionally classified as members of the DA class. On the other hand, H-deficient white dwarfs account for the remaining 15%, and are usually known non-DAs. The class of non-DA white dwarfs is practically made of white dwarfs with He-rich atmospheres, and the vast majority of them have pure helium atmospheres (thus belonging to the DB spectral type). There is only a handful of the coolest white dwarfs which have atmospheric heavier

elements. These findings have been recently corroborated by the study of Myszka et al. (2012) who have presented the distribution of spectral types and space motions for 205 white dwarfs located within 25 pc. Specifically, these authors find that 120 stars are non magnetic white dwarfs belonging to the DA spectral class, with effective temperatures $4600 \text{ K} \lesssim T_{\text{eff}} \lesssim 25\,000 \text{ K}$, whereas the rest of the white dwarfs in the sample belong to the non-DA spectral classes (DB, DBQZ, DC, DQ, DZ, DQZ, DZA), or are H-rich white dwarfs with traces of metals (DAZ), or are white dwarfs with magnetic features. Magnetic white dwarfs account for 8% of the sample. In summary, according to this work there are 2.4 times more white dwarfs of the DA type than of the non-DA one, and the same factor is found when comparing the magnetic group of DA white dwarfs with that of non-DAs.

The composition of the envelope of white dwarfs gives us information about the late stages of the evolution of the progenitor star before becoming a white dwarf, and in this way we might also guess its evolutionary channel. The spectra of white dwarfs also yields information about the ionization degree of the interstellar medium — see Redfield & Linsky (2008) and references therein — as well as information about the circumstellar material around the white dwarf, whose spectral features are superimposed to the spectrum of the star. This circumstellar material is attributed to mass loss through winds or to the presence of a companion, or to the remains of the planetary nebula phase, or to dust or debris disks. However, a proper modeling of the chemical evolution of the envelopes of white dwarfs is a hard task as residual nuclear reactions and a competition between several processes like gravity, radiative levitation, diffusion and several other are responsible for the chemical profiles of white dwarf envelopes. Moreover, the chemical profiles of white dwarfs evolve with time, which means that the composition of the surface also changes with time (Fontaine et al., 1987; Bergeron et al., 1995; Koester & Wilken, 2006; Bergeron et al., 2011).

Besides DA and DB white dwarfs — the most common ones — there are two more types of white dwarfs that are quite frequently found, namely DOs and hot DQs. We describe them separately. DO white dwarfs (Hügelmeier et al., 2006) are thought to be either the descendants of PG 1159 stars or mergers products. If they result from the evolution of PG 1159 stars the progenitors may have lost most of its hydrogen in a late helium flash at the end of the thermally pulsing phase at the Asymptotic Giant Branch (AGB). It is thought that an atmospheric model with stratified He/H abundances (Koester, 1989) may lead to traces of residual hydrogen to float or emerge to the photosphere. This would occur for temperatures $T_{\text{eff}} \lesssim 45\,000 \text{ K}$ leading to the formation of a thin layer of hydrogen on the top of the helium layer which, in turn, would convert DO white dwarfs into DA white dwarfs. This evolutionary scenario would explain the so-called DO/DB gap. The spectral evolution continues until helium can be dredge up again at $T_{\text{eff}} \lesssim 30\,000 \text{ K}$, turning successively the DA white dwarf into a DBA one, and then into a white dwarf of the DB type. Fontaine, Wesemael, Vennes & Pelletier (1987) explained the conversion of DA white dwarfs into DBs by convective dilution of the hydrogen layer into the underlying helium

layer. At $T_{\text{eff}} \lesssim 14\,000\text{ K}$ carbon may be dredge up to convert DB white dwarfs into a newborn DQ star (Pelletier et al., 1986; Dufour et al., 2007, 2008). The peculiar hot–DQ spectral type might have followed a different evolutionary path. The chemical composition of the envelope of the paradigmatic star of this class, H1504+65, could be explained by convective mixing and dilution of the He layer of DO stars (Dufour et al., 2008; Althaus et al., 2009). These carbon-dominated atmospheres have been the subject of asteroseismological studies (Fontaine et al., 2008), which confirm this origin. Two other peculiar white dwarfs with large photospheric oxygen abundances were reported by Gänsicke et al. (2010) and they are believed to be white dwarfs with bare oxygen–neon cores. According to the authors these white dwarfs might have come from star progenitors with masses between $\sim 8 M_{\odot}$ and $11 M_{\odot}$, that avoided core collapse.

Nevertheless, there are some other points that deserve further attention. The first one concerns whenever proper motions are not measurable, which usually happens for distant stars. When this occurs there are several types of stars that display similar spectra and colors. This happens, for instance, with the spectra of subdwarfs (sdB and sdO stars) which can be confused with hot DA white dwarfs, or to K and M dwarfs, for which their spectra resemble that of the coolest white dwarfs. This poses a limitation to large surveys, as white dwarfs in these surveys cannot be discerned from A, F and K main-sequence stars at $T_{\text{eff}} \lesssim 8000\text{ K}$ because of overlapping in colors (Kleinman et al., 2004; Harris et al., 2006; Tremblay et al., 2011). Secondly, there is a lack of robustness on the atmospheric cooling models at temperatures $T_{\text{eff}} \lesssim 12\,000\text{ K}$, which leads to somewhat large errors in the determination of the spectroscopic mass of the white dwarf. This, in turn, poses a serious limitation to the determination of the correct atmospheric abundances.

1.2.2 Distribution in effective temperatures

White dwarfs are observed in a wide range of effective temperatures, from $\sim 200\,000\text{ K}$ to $\sim 4000\text{ K}$. It is important to realize that many factors — such as the degree of ionization or the presence of traces of minor chemical elements — may modify the effective temperature of a given white dwarf. The degree of ionization of elements increases with the temperature. Consequently, spectral types do not exactly correspond to temperature ranges, but there is overwhelming evidence that the fraction of H-rich versus H-deficient changes with the temperature. For instance, Kleinman et al. (2004) studied the spectral distribution as a function of the temperature for the sample of white dwarfs of the SDSS and found a peak of DA white dwarfs at $\sim 10\,000\text{ K}$ and for the DBs at $\sim 16\,000\text{ K}$, both with a tail to higher temperatures. In general, H-rich white dwarfs are more numerous in the region $T_{\text{eff}} \gtrsim 12\,000\text{ K}$, whereas H-deficient ones are more frequent in the coolest region, $T_{\text{eff}} \lesssim 12\,000\text{ K}$. A general description of the properties of white dwarfs as a function of the effective temperature is presented as follows:

- (i) The highest temperature range, $T_{\text{eff}} \sim 200\,000\text{ K} - 45\,000\text{ K}$, corresponds to the hottest white dwarfs, and therefore the youngest ones. These white dwarfs contain H-dominated atmospheres or singly ionized helium HeII (DO), in a factor 7 : 1 (Fleming et al., 1986). On average, white dwarfs with helium-rich atmospheres are hotter than those with H-rich ones.
- (ii) In the range of $T_{\text{eff}} \sim 45\,000\text{ K} - 30\,000\text{ K}$ there are basically DA white dwarfs, and hardly a few H-deficient white dwarfs (Eisenstein et al., 2006b; Dreizler & Werner, 1996) are found. For this reason in the literature this range of effective temperatures is known as the DB/DO gap.
- (iii) In the range $T_{\text{eff}} \sim 30\,000\text{ K} - 11\,000\text{ K}$ white dwarfs with atmospheres rich in neutral helium (of the spectral type DB) are abundant, whereas peculiar carbon-dominated atmospheres, known as “hot DQ” white dwarfs, are also found (Liebert et al., 2003; Dufour et al., 2008).
- (iv) In the coolest range of effective temperatures, $T_{\text{eff}} \lesssim 11\,000\text{ K}$, where the process of crystallization takes place, white dwarfs with pure hydrogen atmospheres are numerous, although white with carbon-dominated atmospheres or white dwarfs with metal atmospheres are also found, as well as hybrid configurations, and white dwarfs with featureless spectra, with neither emission nor absorption lines. In these cases photometry is required to discern the spectral type because hydrogen becomes spectroscopically undetectable in the visible at $T_{\text{eff}} \lesssim 5000\text{ K}$, and helium at $T_{\text{eff}} \lesssim 10\,000\text{ K}$. The region with $T_{\text{eff}} \sim 6000\text{ K} - 5000\text{ K}$ is rather intriguing due to the fact that no single white dwarf with a pure helium atmosphere has been found (Bergeron et al., 2001) so far — this would be a second mysterious DB gap.

It is worth stressing that the range of effective temperatures $\sim 6\,000\text{ K} - 4\,000\text{ K}$ comprises the majority of halo white dwarfs. The most recent study of this range of effective temperatures has been done by Kilic et al. (2009), who have presented the largest near-infrared spectroscopic survey of white dwarfs in the above mentioned range of temperatures. Due to the small sample size (40 stars) the results are controversial. Specifically, by fitting atmospheric models to the SDSS photometry and the IRTF synthetic photometry these authors found evidence that the stars reported as belonging to the DC spectral type were indeed of the DA and DB ones. Secondly, they did not find any white dwarf of the DB spectral type with temperature below $5\,000\text{ K}$. Thus, they suggested that the mysterious second DB gap could be an artifact of the cooling models rather than being originated by a physical process inside the star.

1.2.3 Metallicity content of white dwarfs

The presence of atmospheric elements heavier than hydrogen or helium has been suggested to be driven by contamination due to accretion events such as mass loss from a binary companion, tidally disrupted asteroids, rocky planets and comets, or accretion of some circumstellar material, or dust or gas from the interstellar medium. For instance, Dufour et al. (2010) suggested that white dwarfs with He-rich atmospheres with metal lines (DBQ, DBZ) are the result of DB white dwarfs accreting matter from a disk. In general, for white dwarfs cooler than $T_{\text{eff}} \lesssim 25\,000\text{ K}$ many authors (Zuckerman et al., 2003; Chayer & Dupuis, 2010; Dupuis et al., 2010a,b) advocate accretion as a key factor to explain the abundance of metals in the atmosphere. In fact, the photosphere would be devoided of heavier elements for these range of temperatures due to gravitational settling, which is more efficient than radiative levitation (Koester & Wilken, 2006). Additionally, there are a few cases for which a binary origin might be elucidated.

However, intricate spectroscopic analysis have unexpectedly unraveled the presence of traces of metal elements in hot pure-hydrogen white dwarfs (Koester, 1989; Sion et al., 1992; Barstow et al., 1993; Holberg et al., 1998; Barstow et al., 2001, 2003). The theoretical explanation for this is that DA white dwarfs with the highest effective temperatures ($T_{\text{eff}} \gtrsim 50\,000\text{ K}$) may show metals in the photosphere due to radiative levitation, that would operate owing to the large upward radiation pressure. In these cases radiative levitation exceeds gravitational settling (Chayer et al., 1994, 1995a,b). However, it is well possible that the presence of atmospheric metals would have an origin not only on the progenitor stars but also could be due to binarity. Nonetheless, despite the fact that the theory of radiative levitation might well predict and justify to some extent the metal features observed in most of the hot DA white dwarfs, it fails dealing with all the individual abundances (Chayer et al., 1995a).

To be sure that the metal content of the star comes from an outer source, an analysis of the spectra combined with a study of its photometry must be performed. Better results are obtained if these analysis are applied to white dwarfs belonging to the same population, in order to rule out the contribution of the interstellar medium. For example, accreting material from a binary companion should be evident in the spectrum of a source with radial velocity variations. Studies of this kind have been performed by Farihi et al. (2010), who studied the SDSS sample of white dwarfs with metal features in their spectra. It was found that within the 146 DZ stars there was no evidence allowing to connect the calcium abundances to interstellar clouds. In the region of temperatures $T_{\text{eff}} \lesssim 12\,000\text{ K}$, it was concluded that the DBZ and DC stars were part of the same population. Bearing in mind that the matter accreted from the interstellar medium would be present in every spectrum of the stars of the population, and as DC stars show featureless spectra, the metallic content of the DBZ white dwarfs has then been suggested to come from tidally disrupted rocky

planets.

To sum up, the most common types of white dwarfs have atmospheres with either pure hydrogen (DA) or helium (DB). The DA spectral type appears in all range of effective temperatures, whereas the DB stars appear below 30 000 K. The fraction of stars belonging to the DA spectral class versus those belonging to the non-DA class varies as a function of the effective temperature, and is interpreted as a sign of the chemical evolution of white dwarf atmospheres. The surface composition changes due to some processes that allow mixing and diffusion of chemical elements between the deepest layers of the atmosphere and the very outer layers. As a consequence of these processes chemical elements of the underlying layers may be dredged-up to the surface. This may happen to the hottest H-rich atmospheres, which may allow to turn them in stars of the DAZ type. Also, stars with He-rich atmospheres may be turned into white dwarfs with H-rich atmospheres, and vice versa. On the other hand, the metal content of the atmospheres of the coolest white dwarfs (those with $T_{\text{eff}} \lesssim 20\,000\text{ K}$) has been attributed to contamination by accretion events.

1.3 Mass distribution

The internal composition of a white dwarf depends on its mass. White dwarfs with low masses, $M_{\text{WD}} \lesssim 0.5 M_{\odot}$, have cores made of helium and have a binary origin. White dwarfs with somewhat larger masses have progenitors which burned helium in previous evolutionary stages, and therefore have cores made of carbon and oxygen. This is true for white dwarfs with masses up to $M_{\text{WD}} \sim 1.0 M_{\odot}$. White dwarfs with masses even larger have cores made of oxygen and neon. This is the case of white dwarfs with masses larger than $\sim 1.0 M_{\odot}$, and up to the Chandrasekhar mass limit. In general, it can be said that those disk white dwarfs with longer cooling ages come from massive progenitors because they have shorter main-sequence lifetimes. Additionally, they are expected to produce white dwarfs with high mass cores. Consequently, it should be expected that massive white dwarfs should have both small radii and luminosities, and therefore they would be more difficult to detect. As far as low-mass white dwarfs are concerned, it is important to realize that up to now every single white dwarf with $M_{\text{WD}} < 0.5 M_{\odot}$ found so far has a H-rich atmosphere (Bergeron et al., 2011). This supports the idea that their progenitors were truncated their evolution before the helium flash at the red giant phase took place.

One of the most recent studies of the white dwarf mass distribution has been performed by Kepler et al. (2007) using data from the SDSS. The mean mass for the DA white dwarf stars brighter than 19^{mag} in the g-band and effective surface temperatures hotter than 12 000 K is $\langle M_{\text{DA}} \rangle = 0.593 \pm 0.016 M_{\odot}$, whereas for DB white dwarfs that fulfill $g \leq 19^{\text{mag}}$ and $T_{\text{eff}} \geq 16\,000\text{ K}$, the mean mass is $\langle M_{\text{DB}} \rangle = 0.711 \pm 0.009 M_{\odot}$. Other surveys have obtained similar white dwarf average masses.

This is the case of the study of Limoges & Bergeron (2010), who have presented a spectroscopic analysis of white dwarfs found in the Kiso survey. For a sample of 136 DA white dwarfs they find a mean value $\langle M_{\text{DA}} \rangle = 0.606 \pm 0.135 M_{\odot}$, and for a sample of 23 DB types a mean of $\langle M_{\text{DB}} \rangle = 0.758 \pm 0.192 M_{\odot}$. However, their DB mass distribution appears to be quite flat because of the rather small number of DB stars found. Nevertheless, the reader should keep in mind that the precision of the determinations of the masses of the observed white dwarf population is a topic of intense debate. For instance, Bergeron et al. (2007) discuss the actual methods such as spectroscopic, trigonometric parallax, and gravitational redshift measurements, paying attention to the regime $T_{\text{eff}} < 12\,000\text{ K}$, where energy transport by convection is concomitant.

A related issue consists in connecting the white dwarf mass with that of its main sequence progenitor, that is establishing an initial–final mass relationship. Catalán et al. (2008b,a) have derived a reliable initial–final mass relationship of white dwarfs belonging to common proper motion pairs — binaries with long periods which are believed not to have interacted. These systems allow to obtain valuable information about the evolutionary paths leading to the formation of white dwarfs. Moreover, they also allow to derive constraints on ages, distances and reddening, as well as to directly measure the amount of mass ejected to the interstellar medium through all the stellar evolutionary phases prior to the formation of the white dwarf.

To sum up, the white dwarf mass distribution of DA white dwarfs (the most abundant spectral class) has a narrow peak around $\sim 0.6 M_{\odot}$. When it comes to the DB white dwarf mass distribution, it is found that it is shifted to slightly higher masses. Additionally, a lower peak reveals the existence of a population of low-mass white dwarfs, which very likely have been produced in close binary systems where the evolution of the progenitor star was truncated and did not reach the phase of core helium burning. There is also a secondary peak around $\sim 1.1 M_{\odot}$ with a tail extending to longer masses which corresponds to progenitors that ignited carbon in the core of the progenitor star and were able to produce an oxygen–neon degenerate cores or to mergers of two lighter white dwarfs.

1.4 The white dwarf luminosity function

1.4.1 Definition, estimators and completeness

The white dwarf luminosity function is defined as the number of white dwarfs per unit volume and luminosity interval (or bolometric magnitude). From a theoretical point of view, the white dwarf luminosity function can be computed as:

$$N(L) = \int_{M_{\text{low}}}^{M_{\text{up}}} \Psi(t) \phi(M) \frac{dt_{\text{cool}}}{d \log(L/L_{\odot})} dM \quad (1.1)$$

where $\Psi(t)$ is the star formation rate, $\phi(M)$ is the initial mass function, L and t_{cool}

are the luminosity of the white dwarf and its cooling time, respectively. The interval of integration M_{low} and M_{up} corresponds to the minimum and maximum mass of the progenitor star able to produce a white dwarf at a fixed luminosity L .

The shape of the observational white dwarf luminosity function of the Galactic disk has been found to be monotonically increasing with decreasing luminosity up to bolometric magnitudes of $M_{\text{bol}} \approx 15.5$ — which corresponds to an absolute visual magnitude $M_V \approx 16$, or equivalently to a luminosity $\log(L/L_\odot) \sim 4.5$. At this magnitude the white dwarf luminosity functions shows a well defined and sharp downturn. This drop-off of the luminosity function is a clear indicator of the finite age of the Galaxy. The existence of this cut-off was first proposed by Schmidt (1959), and it allowed to compute the age of the Galactic disk (Winget et al., 1987; Garcia-Berro et al., 1988a,b; Liebert et al., 1988). Besides the age of the galactic disk the white dwarf luminosity function carries extensive information about the stellar formation history, and about the structure and chemical evolution of the Galaxy.

In large surveys white dwarfs are generally found because of their relatively high proper motions. Additionally certain color cuts to discard artifacts are also applied to the resulting sample. Generally speaking, this procedure produces a biased sample, and hence the selection criteria are of critical importance to obtain a reliable luminosity function. Traditionally, to obtain accurate luminosity functions most studies have adopted the $1/V_{\text{max}}$ method, also known as Schmidt’s estimator. This method was originally introduced by Schmidt (1968), and has been progressively updated in a series of successive works (Schmidt, 1975; Felten, 1976). The $1/V_{\text{max}}$ estimator has been shown to produce accurate an white dwarf luminosity function of the disk of our Galaxy using kinematically selected samples (Wood & Oswalt, 1998; García-Berro et al., 1999). In particular, this last study analyzed the effects of the observational selection criteria and the biases introduced by these criteria. These authors found that the observational errors in the tail of the white dwarf luminosity function were mostly due to uncertainties in the bolometric corrections and in the trigonometric parallaxes. Both uncertainties result in small-scale statistical uncertainties and fluctuations in the derived luminosity function. They also reported a disk age around 10 Gyr, which agrees with several other determinations obtained using very different methods. Subsequently Geijo et al. (2006) performed a study of the statistical reliability of the disk white dwarf luminosity function using several different estimators, including the $1/V_{\text{max}}$ method. In a second study (Torres et al., 2008) they also took into account the error in the determination of the parallax (the so-called Lutz–Kelker bias) and the contamination by misclassified halo white dwarfs. They deemed that the best two estimators were the Choloniewski method (Choloniewski, 1986) and the $1/V_{\text{max}}$ method. However, the Choloniewski method was found to be more suitable to derive the disk luminosity function since the position of the cut-off is not affected by the above-mentioned measurements errors.

The incompleteness of the observational sample is an important issue, which should be taken into account carefully. However, it should be pointed out that even

having a small number of stars but using a complete volume-limited sample one may have good completeness, and therefore to be statistically significant. This happens to the local sample of white dwarfs within 20 pc of the Sun, which according to Holberg et al. (2008) is claimed to be nearly complete (80%) although it just contains a small number of white dwarfs, 122. The completeness of one of the largest and well-known surveys, the SDSS spectroscopic survey, has been reported to be 15–50 %, although the sample of white dwarfs with $T_{\text{eff}} \gtrsim 8000$ K is quite complete (Eisenstein et al., 2006b; De Gennaro et al., 2008; Tremblay et al., 2011). Studies of completeness dependence on magnitude and proper motions of the SDSS survey have been carried out by Harris et al. (2006). The shape of the luminosity function is obtained with excellent accuracy for the hottest white dwarfs, but its completeness severely decreases near the downturn. Another study of the local sample of white dwarfs worth mentioning is that of the Palomar Green Survey (Green et al., 1986). Bergeron et al. (2011) and Gianninas et al. (2011) have devoted a large amount of work to analyze this sample. Yet there are many other studies, among which we mention those dedicated to analyze Limoges & Bergeron (2010) the Kiso survey (Noguchi et al., 1980; Kondo, 1984). Recently, Giammichele et al. (2012) have studied the completeness within of the local sample of white dwarfs considering the uncertainties in distances of the sample of Holberg et al. (2008) and improved atmospheric models. From a small local sample, containing less than 200 white dwarfs lying within 20 pc, they obtained a volume-limited sample with a completeness slightly higher than 90%, and from it they derived a reliable luminosity function.

1.4.2 The thick and the halo white dwarf luminosity functions

Finding a luminosity function for the thick disk is a difficult task given the overlap in velocities between the white dwarf populations of the thin and thick disk. Even so, Rowell & Hambly (2011) using the SuperCOSMOS Sky Survey have recently been able to distinguish among these Galactic populations. Their results indicate that the contribution of the thin disk to the local white dwarf density is 79%, whereas the contribution of the thick disk is 16% and the halo contribution is a modest 5%. Actually, the number of identified halo white dwarfs is extremely small. This is so because most halo white dwarfs are thought to have very faint absolute visual magnitudes $M_V > 17$, and consequently very low effective temperature $T_{\text{eff}} < 4000$ K. Accordingly, this prevents deriving a reliable observational white dwarf luminosity function for the halo population. Nevertheless, using data of only 6 halo white dwarfs identified using their kinematics, Liebert et al. (1989) derived a preliminary halo white dwarf luminosity function. Later on, Flynn et al. (1996) identified 5 more halo white dwarf candidates in the Hubble Deep Field. Also, Torres et al. (1998) employed an artificial neural network algorithm to optimize the recognition of halo white dwarfs from the existing catalogs. This turned out to be a successful technique and the number of identified halo white dwarfs improved substantially, yet still the

sample remained severely incomplete.

Generally speaking, halo white dwarfs have higher tangential velocities and larger proper motions, μ , than their disk counterparts. Thus, to identify halo white dwarfs it is customary to use the so-called reduced proper motion, H , which for a particular magnitude band is given by

$$H = m + 5 \log \mu + 5 = M + 5 \log(V_{\text{tan}}/4.74) \quad (1.2)$$

where μ is the proper motion given in units of $''/\text{yr}$, m and M are the apparent and the absolute magnitude respectively, and V_{tan} is the tangential velocity in units of km/s. It turns out that the reduced proper motion of a star is a good indicator of its halo membership. This is so because the reduced proper motion diagrams distinguish stellar populations of similar kinematics but different absolute magnitude calibrations, as well as populations of similar absolute magnitude distributions but different kinematics. In this sense, optical and infrared reduced proper motions diagrams have shown to be fairly successful to find new cool white dwarfs and to segregate the thin, the thick disk and the halo populations.

1.5 White dwarfs as dark matter

Since the first years of the twentieth century, studies based on the dynamical density of matter and the rotation curve of our Galaxy revealed a kind of non-luminous matter, the so-called dark matter. These studies were carried out by Öpik (1915), Kapteyn (1922), Jeans (1922) and Oort (1932) and gave as a result an intense debate among astronomers. Jan Oort's examined Doppler shifts in the spectra of stars of our Galaxy and his findings were hailed as the first measurement of dark matter. The second dark matter evidence is attributed to Zwicky (1933, 1937), who measured redshifts in the spectra of the galaxies of the Coma cluster. During the seventies and the eighties, several studies extended the observational basis of dark matter by measuring the rotation curve of other spiral galaxies — see, for example, Rubin & Ford (1970); Rubin et al. (1977, 1979, 1985). These studies concluded that most of the matter in the Universe was indeed dark. To date much empirical evidence of a dark-dominated Universe has been tracked down in motions of galaxies in clusters, flat rotation curves of spiral galaxies, motions of stars in elliptical galaxies, relative velocities in binary galaxies pairs, gravitational lensing, hot gas in galaxy clusters and many other. A summary of projects which have given evidence for a dark matter dominated Universe is:

- (i) Type Ia supernovae surveys such as the High-z Supernova Search (Riess et al., 1998), and the Supernova Cosmology Project (Perlmutter et al., 1999).
- (ii) Cosmic Microwave Background (CMB) radiation discovery and measured by the COBE and WMAP missions.

- (iii) Large-scale structure surveys, such as the SDSS and the 2dF Galaxy Redshift Survey.
- (iv) Cluster surveys (lensing and high-redshift cluster in optical surveys), such as the RCS and RCS2.
- (v) Gravitational lensing experiments such as the MACHO, EROS, and OGLE projects.
- (vi) The Dark Energy Survey (DES), currently working on Type Ia Supernovae, Baryon Acoustic Oscillations, Galaxy Cluster distribution and Gravitational Lensing.

The above mentioned cosmological observations show compelling evidence that ordinary matter, also known as baryonic matter, represents only a small fraction of the total matter in our Universe and that non-baryonic dark matter dominates over baryons. This non-baryonic dark matter is characterized by its weakly interaction with ordinary matter. Additionally, all matter is embedded in a dark-dominated energy. To characterize dark matter and dark energy it is usually employed the so-called cosmological constant, which is defined as the fraction of the effective mass of the universe attributed to dark energy, which is the predominant component, $\Omega_\Lambda \simeq 0.73$. The mass density includes the ordinary mass plus dark matter components, $\Omega_M \simeq 0.27$. The ordinary or baryonic component is just $\Omega_B \simeq 0.044$ (Bennett et al., 2003; Larson et al., 2011; Komatsu et al., 2011). This is the same to say that $\simeq 73\%$ of the Universe is composed by dark energy, which produces an accelerated expansion, whereas the remainder $\simeq 22\%$ is attributed to dark matter, and just only $\simeq 4.4\%$ to baryons. Moreover, the cosmic mean baryon fraction (Ω_B/Ω_M) represents 17% of the total matter of the Universe. Besides, most of the baryons are non-luminous, since $\Omega_\star \simeq 0.005$. For the case of our own Galaxy, the virial mass out to 100 kpc is $M \approx 10^{12} M_\odot$, whereas the baryonic mass in the form of stars is $M_\star \approx 7 \times 10^{10} M_\odot$. In other words, for the Milky Way the baryon fraction is at most 8% (Klypin et al., 2002). This problem is known as the missing baryon problem — see the excellent review of Silk (2007) for a complete, interesting and recent discussion of this issue — and it is critical in our understanding of how the Galaxy (and by extension other galaxies) were formed and will ultimately evolve.

Baryonic dark matter, despite being inconspicuous, is the only kind of matter directly accessible to observational detection. In this sense, numerous experimental searches have been pursued the detection of baryonic dark matter by means of its gravitational lensing inferences. Since the pioneering observational detection of the first Galactic gravitational microlensing events by the MACHO team (Alcock et al., 1995, 1997, 2000), that suggest that the halo dark matter of our Galaxy may contain a significant population of ultra-cool white dwarfs, many efforts have been devoted to this issue. In fact, after these preliminary discoveries, several other teams pursued

similar studies to either confirm or discard their results. Among these observational studies there are those performed by the EROS (Lasserre et al., 2000; Goldman et al., 2002; Tisserand et al., 2007), OGLE (Udalski et al., 1994), MOA (Muraki et al., 1999) and SuperMACHO teams (Becker et al., 2005). All of them have monitored millions of stars during several years in both the Large Magellanic Cloud (LMC) and the Small Magellanic Cloud (SMC) to search for microlensing events. Despite the increasing number of surveys that are searching for white dwarfs, the contribution of this population and their respective sub-populations to the dark matter content of our Galaxy still remains to be elucidated.

1.6 White dwarfs in close binary systems

According to theoretical models, white dwarfs with masses $\lesssim 0.5 M_{\odot}$ are expected to have helium cores (Althaus et al., 2001), since they come from progenitors that did not go through the core helium burning phase before their envelope was ejected. Since the evolutionary timescales of single progenitor stars able to produce this type of white dwarfs are very long (Laughlin et al., 1997), the only possible way to form these white dwarfs is, thus, in a binary system, as the envelope of the progenitor star has to be removed by the interaction with a companion, most likely through a common envelope evolutionary phase.

The explanation of interacting evolution with another star is also observationally well supported. Evidence of common envelopes has been collected since the pioneering work of Kuiper (1941), who analyzed both photometric and spectroscopic measurements of the binary system β Lyrae and concluded that it should have a common envelope. Deutsch (1956) made mass-loss rate measurements of the binary system α Herculis and made a prediction of its outcome: “... such star may then shed most of its mass, so that the remnant could come to equilibrium as a white dwarf”. It is also worth mentioning that Kitamura (1959) and Lucy (1973), as well as Paczynski (1976), studied the binary system W Ursae Majoris. The main conclusion of all these works was that common envelope evolution provides a formation channel for cataclysmic variables. Nowadays, there are a large number of these low-mass white dwarfs which are found in close binary systems — see, for instance, Marsh et al. (1995); Liebert et al. (2005); van Kerkwijk et al. (2005); Rebassa-Mansergas et al. (2011), and references therein. We note, moreover, that there is growing evidence that some of the reported single low-mass white dwarfs might be in fact unresolved binary degenerate systems (Giammichele et al., 2012). Additionally, it is alleged that short-period compact-binary systems are outcomes of a mass-transfer process of their progenitors that ends up in common-envelope evolution.

In a common envelope episode both energy and angular momentum are transferred between the orbit and the material flowing out — the common envelope — until the entire envelope is removed, and the orbit is circularized and synchronized.

An in-depth review of close-binary formation and common-envelope evolution can be found in Iben & Livio (1993); Webbink (2008); Ivanova (2011) and Passy et al. (2012). Nevertheless, this process is still poorly understood, and the theoretical models rely on simple parametrizations. This drawback of the theory is an important issue, as there are several other fascinating astronomical phenomena in which a binary system composed by a white dwarf formed during the common envelope phase and another star are involved. For instance, it is thought that high-field magnetic white dwarfs and R Corona Borealis form as a consequence of the merger of double low-mass white dwarfs. In this case both stars of the binary system were formed very likely through a common envelope phase. Other outstanding systems in which a common envelope phase is involved are those systems in which a white dwarf accretes material from a main-sequence or a giant star (Munari & Renzini, 1992). These systems comprise the groups of cataclysmic variables systems and symbiotic stars, which are possible progenitors of Type Ia supernovae. Additionally, white dwarfs with either a neutron star or a black hole companion are thought to be possible precursors of gamma-ray bursts (Belczynski et al., 2002). Finally, several possible sources of gravitational wave radiation are binary systems in which one of the components is a white dwarf. These comprise binary white dwarfs, which would ultimately merge, and interacting white dwarfs in dense stellar systems, like globular cluster.

Chapter 2

Building the sample

This chapter is devoted to explain the methodology and the physical and astronomical inputs used in our simulations. In the first section, we introduce the basic elements of a Monte Carlo simulator, and we review the statistical tools associated with it. In the second part of this chapter, we comprehensively describe our Monte Carlo simulator and the main ingredients used to build our synthetic populations of white dwarfs aimed at ascertaining if the microlensing experiments can be explained by a population of dim white dwarfs. Finally, in the third section of this chapter we focus on the methods employed to perform Monte Carlo simulations of the Galactic population of binary systems formed by a white dwarf and a main sequence star.

2.1 The Monte Carlo method

The Monte Carlo simulation method is a thriving computer-intensive statistical tool used to model a wide range of physical systems. In order that the simulation may well represent a model of reality, inputs are assigned as experimental or semi-experimental law distributions and integrated employing a pseudo-random number generator algorithm. Not only are models constructed and validated through the Monte Carlo method, but also we can better understand a complex system behavior besides predicting its future or what-if analysis by varying the input parameters. On top of that, it might provide numerical solutions where there have not been found analytic solutions.

The Monte Carlo procedure is based on generating a large number of independent random simulated samples, with the goal of bringing out the probability of occurrence of the outcome values, referred as the sampling distribution, also called probability distribution or frequency distribution. The more iterations, the smoother will be the output probability distribution. Randomness is the cornerstone of any Monte Carlo simulator. We provide it by means of the random number generator algorithm of James (1990), which offers excellent statistical properties as well as a

very large repetition cycle $\gtrsim 10^{18}$, which is virtually infinite for the purposes of our studies. On the other hand, a statistical test is considered reliable if it is reproducible, that is if the same result is obtained repeatedly. It follows that in Monte Carlo simulations an optimal number of simulations should be performed so that their sum converges to a limiting stable distribution (Uchaikin & Zolotarev, 1999). If this occurs the resulting sampling distribution is a good likelihood estimator of true sampling distribution for the observed population, which is the same to say that we obtained an unbiased estimator for the unknown true distribution. Hence, its derived values are an unbiased good approximation of the true parameter values. The standard error of the mean, that is the standard deviation of the mean of the sample distribution, tells us about the variability of the sample, and therefore provides a measure of the accuracy of the resulting estimates.

Due to the fact that the phenomena we simulating are rare, to reach reliability in our calculations we ran a very large number of Monte Carlo simulations, approximately $\sim 10^4$. From each simulation we computed the mean values of the most relevant observational quantities of our interest. Then, we drew the sampling distributions from the data collection and extracted the average values and their corresponding statistical errors. Moreover, in addition to the observational selection criteria, we eliminated low probability outcomes with large impact in the results, leading to heavy-tail distributions, which usually are very few simulations that provide exaggerated and unrealistic results. The averages of the quantities of interest are accompanied by their respective standard deviations, which represent how much they vary among the set of different simulations. In particular, for the case in which the number of microlensing events towards the LMC is considered, the mean value estimates of interest for a typical lens are its mass, proper motion, distance, tangential velocity, crossing time \hat{t}_E , and the contribution to the microlensing optical depth. These are drawn from distributions of sample means from the set of simulations reporting microlensing events. For a large number of realizations a Gaussian distribution of the values is reached. Consequently, Monte Carlo standard errors are associated to sample mean distributions. However, the reader should take into account that for a given set of assumptions to be a valid representation of the observed population (choosing among various inputs models), a goodness-of-fit test must be performed to compare the output simulated data with the observed population. In the case that the observed sample would not fit to any known distribution, then a non-parametric goodness-of-fit should be performed. In our simulations we used the χ^2 test, Student's t -test, the Z -test and the Kolmogorov-Smirnov test — see NIST/SEMATECH, e-Handbook of Statistical Methods¹.

Finally, in all our calculations we expand the number of different Monte Carlo realizations by means of a resampling method (Chernick, 2007). Specifically, we take advantage of the bootstrapping technique. Due to the fact that resampling can

¹<http://www.itl.nist.gov/div898/handbook/>

be done without taking into account any assumption about the probability distribution of the population, non-parametric bootstrapping can be used not only for deriving the sampling distribution-free values of interest but also for assessing the precision and variability of sample statistics. It consists in generating resamples in an equal probability from one original sample, which is named resampling with replacement. Each resample, also called “bootstrap sample” or “replication”, must be of the same size (number of elements) as the original sample. Ultimately, we used the bootstrapping method as a tool so as to streamline the Monte Carlo computations, which results in large savings of computer time. The bootstrapping technique was specially useful for our simulations of the Galactic population of binaries. In this case we computed the evolution of around ~ 10 millions of zero-age binary systems on each Monte Carlo simulation, and we performed ~ 20 independent realizations per each one of the ~ 50 models. Due to the fact that the selection criteria of the survey dramatically reduce the number of synthetic stars, we have employed a bootstrap method which allowed us to obtain a total of $\sim 6 \times 10^3$ resamples per model. Averages of the observational quantities of interest are taken from an ensemble of means alongside their corresponding standard errors as standard deviations of their bootstrap distributions.

2.2 The population of gravitational microlenses

2.2.1 The halo model

We have adopted a spherically symmetric halo. The density profile of this model is the isothermal sphere of radius 5 kpc, also called the “S-model”, which has been extensively used by the MACHO collaboration (Alcock et al., 2000; Griest, 1991). Despite the existence of other density profiles, such as the exponential power-law model, the Navarro, Frenk & White (1997) density profile and others, in a previous study (García-Berro et al., 2004) it was shown that the differences between them are not significant for the case under study and, consequently, we adopt the most simple description. The position of each synthetic single star is randomly chosen according to this density profile. We proceed generating homogeneously and uniformly zero-age main sequence stars in an sphere centered at the Sun, with a radius of approximately 200 pc. Likewise, we generated zero-age main-sequence stars following the above mentioned density profile in cones centered at the Sun, pointing to the Large Magellanic Cloud and covering distances until the outer limit of the halo. The adopted aperture angle of each cone is identical to the observational window of the respective experiment.

Given the age of the halo, the time at which each main-sequence progenitor was born and the main-sequence lifetime as a function of the mass in the main sequence (Iben & Laughlin, 1989) we know which stars have had enough time to become white dwarfs. Consequently, using a set of theoretical cooling sequences and the initial to

final mass relationship (Iben & Laughlin, 1989), we get their luminosities, effective temperatures, colors and the rest of relevant properties. The cooling sequences adopted here depend on the mass and are described below. Furthermore, we assume that the halo was formed 14 Gyr ago in an intense burst of star formation of duration ~ 1 Gyr. Besides, we have considered as our reference model the standard stellar initial mass function of Scalo (1998), which follows a power law given by:

$$m\phi(m) \propto \begin{cases} m^{-0.2}, & 0.1 < m \leq 1, \\ m^{-1.7}, & 1 < m \leq 10, \\ m^{-1.3}, & 10 < m \end{cases}$$

We used an upper mass limit of $30 M_{\odot}$ and lower mass of $0.1 M_{\odot}$. In addition, we have also considered the biased log-normal initial mass function proposed by (Adams & Laughlin, 1996). Other biased initial mass functions — such as those proposed by Chabrier et al. (1996) — have been discarded in most of our simulations, since their results are only marginally compatible with the observational results (García-Berro et al., 2004).

For the kinematical properties of the halo white dwarf population, we used the Box-Muller algorithm of Press et al. (1986) to model the heliocentric spherical velocities according to a Gaussian law (Binney & Tremaine, 1987):

$$f(v_r, v_t) = \frac{1}{(2\pi)^{3/2}} \frac{1}{\sigma_r \sigma_t^2} \exp \left[-\frac{1}{2} \left(\frac{v_r^2}{\sigma_r^2} + \frac{v_t^2}{\sigma_t^2} \right) \right] \quad (2.1)$$

where σ_r and σ_t — the radial and the tangential velocity dispersion, respectively — are related by the following expression:

$$\sigma_t^2 = \frac{V_c^2}{2} + \left[1 - \frac{r^2}{a^2 + r^2} \right] \sigma_r^2 + \frac{r}{2} \frac{d(\sigma_r^2)}{dr} \quad (2.2)$$

which reproduces the flat rotation curve of our Galaxy at large distances. We have adopted a circular velocity $V_c = 220$ km/s. Finally, and in order to obtain the heliocentric velocities we took into account the peculiar velocity of the Sun $(U_{\odot}, V_{\odot}, W_{\odot}) = (10.0, 15.0, 8.0)$ km/s (Dehnen & Binney, 1998). Since white dwarfs usually do not have determinations of the radial component of the velocity, the radial velocity is eliminated when a comparison with the observational data is needed. Moreover, we only consider stars with velocities larger than 250 km/s because white dwarfs with velocities smaller than this would not be considered as halo members. Additionally, we also discard stars with velocities larger than 750 km/s, because they would have velocities exceeding 1.5 times the escape velocity of the Galaxy.

In order to compare the simulated results with the observational ones, a normalization criterion should be used. We have normalized our simulations to the local density of halo white dwarfs obtained from the halo white dwarf luminosity function of Torres et al. (1998), but taken into account the new halo white dwarf candidates

found in the SDSS Stripe 82 (Vidrih et al., 2007). Nevertheless, we emphasize that when normalizing to the local density of halo white dwarfs obtained using the white dwarf luminosity function we only consider those stars with velocities higher than 250 km/s, given that only those stars would be genuinely considered as halo members and would be used to build the observational halo luminosity function (Liebert et al., 1989; Torres et al., 1998). This is totally equivalent to the adopted cut in reduced proper motion employed by Flynn et al. (2001). Additionally, only the number density of DA white dwarfs was considered to normalize the simulations, since all but one of the white dwarfs used to obtain the luminosity function of Torres et al. (1998) were of the DA spectral type. Obviously, by imposing this normalization we implicitly assume that the MACHO results and the direct surveys are complementary and seem to be probing the same populations, whatever the nature of those populations be (Hansen & Liebert, 2003).

2.2.2 Modeling the microlensing events towards the LMC

In order to mimic the microlensing experiments towards the Large Magellanic Cloud (LMC), we have closely followed the detailed LMC descriptions of Gyuk et al. (2000) and Kallivayalil et al. (2006). Our model takes into account among other parameters the scale length and scale height of LMC, its inclination and its kinematical properties. This model provides us with a synthetic population of stars representative of the monitored point sources. Afterwards we assess which stars of the Galactic halo could be responsible of a microlensing event. Here it is understood by lens or microlens any stellar object that produces a microlensing event. With that in mind, we have only considered star lenses fulfilling a series of conditions. First of all the candidate lensing stars should be fainter than a certain magnitude limit. In a second step we have checked if the lens is inside the Einstein tube of the monitored star. That is, we checked if the angular distance between the lens and the monitored star source is smaller than the Einstein radius. We recall that a microlensing event blends the light coming from a bright background star source that forms a ring around the lens. The observer sees this phenomenon like a magnification of the area image of the source brightness, which peaks at the perfect alignment observer–lens–source. The Einstein microlensing tube is the three-dimensional structure of the ring projection on the sky. This results in a tube, centered along the direction of perfect alignment, so that any object passing through it will produce a microlensing event as long as the magnification of the background star source brightness is above a certain minimum given by the experimental setup. In our case we have reproduced the MACHO and EROS experiments, which both have this threshold set to 1.34. The Einstein radius is therefore the radius of the microlensing tube and is given by the expression:

$$R_E = 2\sqrt{\frac{GM D_{OS}}{c^2} x(1-x)} \quad (2.3)$$

where D_{OS} is the observer–source distance, $x \equiv D_{\text{OL}}/D_{\text{OS}}$ and D_{OL} is the observer–lens distance. After that, we have determined the duration of the event, named the Einstein diameter crossing time, $\hat{t}_{\text{E}} = 2 \times R_{\text{E}}/V_{\text{tan}}$, where V_{tan} is the transverse velocity of the lens through the microlensing tube (the velocity component perpendicular to the line of sight). Finally, we filtered those stars which are candidates to produce a microlensing event with the detection efficiency function, $\varepsilon(\hat{t}_i)$, where \hat{t}_i is the Einstein ring diameter crossing time of the i -th microlensing event. The detection efficiency depends on the particular characteristics of the experiment. Specifically for the MACHO collaboration we have taken 1.1×10^7 stars during 5.7 yr and over 13.4 deg^2 , whereas the detection efficiency has been modeled according to:

$$\varepsilon(\hat{t}) = \begin{cases} 0.43 e^{-(\ln(\hat{t}/T_{\text{m}}))^{3.58}/0.87}, & \hat{t} > T_{\text{m}} \\ 43 e^{-|\ln(\hat{t}/T_{\text{m}})|^{2.34}/11.16}, & \hat{t} < T_{\text{m}}, \end{cases} \quad (2.4)$$

where $T_{\text{m}} = 250$ days. This expression provides a good fit to the results of Alcock et al. (2000). For the EROS experiment we have used 0.7×10^7 stars over a wider field of 84 deg^2 and over a period of 6.7 yr. Regarding the detection efficiency we have adopted a numerical fit to the results of Tisserand et al. (2007).

For all the simulations presented here, we extracted the parameters relevant to characterize the microlensing experiments. A complete description of the various parameters which are of importance in discussing gravitational microlensing can be found in Mollerach & Roulet (2002) and Kochanek et al. (2004). Among these parameters, perhaps the most important one for our purposes is the optical depth, τ , which measures the probability of a star to be magnified by a lens at a given time by more than the above mentioned factor 1.34. From an observational point of view an estimate of this parameter can be obtained using the expression (Alcock et al., 2000):

$$\tau = \frac{1}{E} \frac{\pi}{4} \sum_i \frac{\hat{t}_i}{\varepsilon(\hat{t}_i)}, \quad (2.5)$$

where E is the total exposure in star–years. The optical depth is independent of the lens motion and mass distribution. However, since the experiments measure the number of events and their durations, additional information can be obtained using the microlensing rate Γ and its distribution as a function of the event durations. This parameter represents nothing else but the flux of lenses inside the microlensing tube. Finally, an estimate of the expected number of events can be derived using the expression

$$N_{\text{exp}} = E \int_0^\infty \frac{d\Gamma}{d\hat{t}} \varepsilon(\hat{t}_i) d\hat{t}_i. \quad (2.6)$$

2.3 Monte Carlo simulations of the binary population

2.3.1 Inputs for the binary population

To start with, the initial primary mass M_1 is obtained using a simplified version of the initial mass function of Kroupa et al. (1993) — see also Kroupa (2001), Reid et al. (2002), and Weidner & Kroupa (2006):

$$\phi(m) \propto \begin{cases} 0, & m \leq 0.1, \\ m^{-1.0}, & 0.1 < m \leq 0.75, \\ m^{-2.7}, & 0.75 < m \leq 30 \end{cases}$$

To compute the mass of the secondary we used different prescriptions for the distribution of initial mass ratios, $q = M_2/M_1$, since the distribution of the secondary masses is still a controversial issue. We took a flat distribution, $n(q) = 1$, as our fiducial model. This prescription implies that the masses of the two components of the binary system are independently drawn from the same initial mass function. We also studied the influence of the distribution of secondary masses using a distribution that depends inversely on the mass ratio, $n(q) \propto q^{-1}$. Finally we studied the case of a lineal dependence of the secondary mass on the primary mass, that is, $n(q) \propto q$. In all the cases we only considered secondary stars with masses $0.06 M_\odot \leq M \leq 30 M_\odot$.

We assigned to each binary system an age of birth, according to constant and exponential star formation rates. The adopted age of the Galactic disk is 10 Gyr. The exponential star formation rate is calibrated so that the present day surface star density matches that of the Galactic stellar disk — $43 M_\odot/\text{pc}^2$ (Flynn et al., 2006). The adopted density distribution follows an exponential law with radial scale length 3.5 kpc. The z coordinate is randomly chosen following an exponential law with scale height $H = 250$ pc. We assumed a fraction of binaries of 50% and we normalized to the local disk density (Holmberg & Flynn, 2000). We randomly choose two numbers for the galactocentric polar coordinates (r, θ) of each star in the sample within approximately 3 kpc from the Sun, following the SDSS DR7 spectroscopic plate directions (Abazajian et al., 2009). In addition, orbital separations were randomly drawn according to a logarithmic probability distribution (Nelemans et al., 2001), $f(a) \propto \ln a$ for $3 \leq a/R_\odot \leq 10^6$. Finally, the eccentricities were also randomly drawn according to a thermal distribution (Heggie, 1975), $g(e) = 2e$ for $0.0 \leq e \leq 0.9$.

Once the mass of the primary star is known, and the properties of the binary system are assigned according to the previously explained procedures, each of the components can be evolved through the main sequence up to their respective giant evolutionary phase. We do that using analytical fits to detailed stellar evolutionary tracks of Hurley et al. (2002), which provide full coverage of the entire range of masses of interest from the zero-age main sequence until advanced stages of evolution. These evolutionary fits provide all the relevant information — such as radii, masses, luminosities, evolutionary timescales, distances... but the photometric prop-

erties, which are calculated independently (see Sect. 2.3.3 below). As far as wind mass losses are concerned, the evolution during the main sequence phase is generally accepted to be conservative, whereas stars are seriously affected by mass losses when hydrogen starts burning in a shell. Accordingly, we adopted for the shell hydrogen burning phase the mass-loss rate of Reimers & Kudritzki (1978), and we assumed an efficiency $\eta = 0.5$. On the other hand, on the asymptotic giant branch the prescription of Vassiliadis & Wood (1993) was used. In the case of moderately close binary systems we also considered a tidally enhanced mass-loss rate (Tout & Eggleton, 1988):

$$\dot{M} = \dot{M}_R \left[1 + B_W \max \left(\frac{1}{2}, \frac{R}{R_L} \right)^6 \right] \quad (2.7)$$

where M and R are the mass and star radius, R_L is the Roche lobe radius, \dot{M}_R is the standard Reimers' mass-loss rate, and B_W is the enhanced mass-loss parameter. We analyzed several models in which B_W varies from 0 to 10^4 . The Roche lobe radius was modeled according to the prescription of Eggleton (1983) and during the overflow episodes both rejuvenation and ageing were taken into account. Also, tidal evolution, circularization and synchronization were considered. Regarding this point we took advantage of the binary evolution algorithm BSE² (Hurley et al., 2002). We took into account angular momentum losses due to magnetic braking and gravitational radiation according to Schreiber & Gänsicke (2003) and Zorotovic et al. (2010) — note that we do not take into consideration magnetic braking and gravitation radiation supplied by the BSE code. From the resulting simulated sample of white dwarf plus main sequence binaries we eliminated those synthetic binary systems which produce cataclysmic variables (Schreiber & Gänsicke, 2003), as well as those binary systems for which the likely outcome is a merger.

For those binary systems in which the primary component had time enough to evolve to the white dwarf stage three situations can be found. For detached systems in which no mass transfer episodes occur whatsoever we adopted the initial-to-final mass relationship of Catalán et al. (2008a) to obtain the mass of the white dwarf. In those cases in which the mass transfer was stable we employed the procedure detailed in Hurley et al. (2002), while if the mass transfer was unstable, i.e. if the system underwent a CE phase, we followed the procedure detailed in the next section. In all the three cases previously described the corresponding evolutionary properties of the resulting white dwarf must be interpolated in the appropriate cooling tracks. For low-mass helium-core white dwarfs (He white dwarfs, $M_{WD} \lesssim 0.5 M_\odot$) we adopted the evolutionary tracks of Serenelli et al. (2001). For intermediate-mass carbon-oxygen core white dwarfs (CO white dwarfs, $0.5 \lesssim M_{WD}/M_\odot \lesssim 1.1$) we used the very recent cooling tracks of Renedo et al. (2010), which include the most up-to-date

²<http://astronomy.swin.edu.au/~jhurley/>

physical inputs. Finally, for the high-mass end ($M_{\text{WD}} \gtrsim 1.1 M_{\odot}$) of the white dwarf mass distribution, composed by white dwarfs with oxygen-neon cores, we adopted the cooling sequences of Althaus et al. (2007). All these cooling tracks correspond to white dwarfs with pure hydrogen atmospheres.

2.3.2 Treatment of the common envelope phase

It is well known that all close compact binaries are formed through at least one common envelope stage. The basic idea of common envelope evolution is straightforward. Once the more massive star in a main sequence binary evolves into the giant or asymptotic giant branch, it overfills its Roche lobe and unstable mass transfer to the less massive companion begins. The companion cannot assimilate the accreted material from the outer layers of the giant, and a common envelope forms around the two stars. Friction within the envelope leads to a dramatic decrease of the orbital separation, and the orbital energy released due to the shrinkage of the orbit may help to expel the envelope. The outcome of common envelope evolution is a post-common-envelope binary (PCEB) at a much closer orbital separation than the one the main sequence binary had initially.

Even though the basic concepts of the evolution during a common envelope phase are rather simple, the details are still far from being well understood. This is so because several complex physical processes play an important role in the evolution during this phase. For instance, the spiral-in of the core of the primary and of the secondary, and the ejection of the envelope are not only a consequence of the evolution of the core and remaining layers of the donor star in response to rapid mass loss, but also tidal forces and viscous dissipation in the common envelope play key roles. Moreover, these physical processes occur on very different timescales and on a wide range of physical scales — see Taam & Ricker (2010) for a recent review. Consequently, a self-consistent modeling of the common envelope phase requires detailed hydrodynamical models which are not available at the present time, although recent progresses are encouraging — see Ricker & Taam (2012) and references therein. Hence, the common envelope phase has been traditionally described using parametrized models.

There are two canonical formalisms to treat the evolution during a common envelope episode. The most commonly used one, known as the α formalism, assumes energy conservation (Webbink, 1984; de Kool, 1990; Dewi & Tauris, 2000). Within the α formalism, the energy transferred to the envelope is parametrized using an efficiency parameter, α_{CE} . Furthermore, the binding energy of the envelope is also modeled with another free parameter, λ , which mainly depends on the mass of the donor and on its evolutionary stage. The most recent formulations also include a third parameter, α_{int} , which is used to measure the fraction of the internal energy contributing to the ejection of the envelope. We describe them in detail in forthcoming paragraphs. The second formalism relies on angular momentum conservation,

and it is known as the γ formalism (Nelemans & Tout, 2005; Nelemans et al., 2000). Here we have not considered the γ formalism since it may explain any kind of configuration, and consequently results in a limited forecast ability (Zorotovic et al., 2010; Webbink, 2007).

Within the α formalism, the envelope is assumed to be isotropic, and brought into corotation with the orbit. In our calculations the evolution during the common envelope phase was computed following the treatment of Hurley et al. (2002). In particular, the Roche-lobe radius is calculated according to the prescription of Eggleton (1983) and during the overflow episodes both rejuvenation and ageing were taken into account. The final separation of a given pair after the common envelope phase was obtained using the usual prescription:

$$\frac{a_f}{a_i} = \left(\frac{m_{\text{WD}}}{M_1} \right) \left[1 + \left(\frac{2}{\lambda \alpha_{\text{CE}} r_{\text{L1}}} \right) \left(\frac{M_{\text{env}}}{M_2} \right) \right]^{-1} \quad (2.8)$$

where a_i and a_f are the initial and final orbital separations, M_{env} is the mass of the envelope of the primary star at the beginning of the CE phase and $r_{\text{L1}} = R_{\text{L1}}/a_i$, where R_{L1} is the radius of the primary at the onset of mass transfer, α_{CE} is the common envelope efficiency and λ is the binding energy parameter. These two parameters are described in detail below.

The common envelope efficiency parameter, α_{CE} , describes the efficiency of ejecting the envelope, namely, of converting orbital energy into kinetic energy to eject the envelope. We then have:

$$E_{\text{bind}} = \alpha_{\text{CE}} \Delta E_{\text{orb}} \quad (2.9)$$

where E_{bind} is the binding energy of the envelope of the primary, usually approximated by the gravitational energy, i.e.:

$$E_{\text{bind}} = - \int_{M_{\text{core}}}^{M_{\text{donor}}} \frac{GM(r)}{r} dm, \quad (2.10)$$

generally rewritten in a more compact and suitable way as:

$$E_{\text{bind}} = - \frac{GM_{\text{donor}} M_{\text{env}}}{\lambda R_1} \quad (2.11)$$

where λ is the binding energy parameter, which represents the ratio between the approximate and the exact expression of the binding energy. In passing, we note that this approximation is equivalent to assume that the resulting white dwarf is a point mass and that the envelope is a shell of homogeneous density located at distance λR_1 from the core of the primary.

We recall here that Han et al. (1995) introduced a parameter α_{th} to characterize the fraction of the thermal energy that is used to expel the common envelope. As in Zorotovic et al. (2010), we will use here the notation α_{int} for this parameter to

emphasize that it includes not only the thermal energy but also the radiation and recombination energy. According to this, Eq. (2.10) becomes:

$$E_{\text{bind}} = \int_{M_{\text{core}}}^{M_{\text{donor}}} \left(-\frac{GM(r)}{r} + \alpha_{\text{int}} U_{\text{int}} \right) dm \quad (2.12)$$

One can include the effects of the internal energy in the binding energy parameter λ by equating Eqs. (2.11) and (2.12). Thus, λ clearly depends on the mass of the donor, its evolutive stage and the fraction of the internal energy, α_{int} , available for ejecting the envelope. Except for models in which a fixed value of λ was assumed, the values of λ were computed using a subroutine from the binary-star evolution (BSE) code from Hurley et al. (2002).

Finally, we note that the final mass of the white dwarf in the post-common envelope binary is determined taking into account the growth of the mass of the core until the binding energy of the envelope becomes positive, at which time we consider that the envelope is ejected instantaneously. Furthermore, we take into account an stellar convective-core overshoot according to Pols et al. (1998).

2.3.3 Photometric magnitudes

The Monte Carlo simulator described so far does not provide photometric magnitudes for the simulated WD+MS PCEBs. In this section we explain how we obtain *ugriz* SDSS magnitudes for the two binary components in an independent manner, that are then combined to obtain the magnitudes of the simulated sample of WD+MS PCEBs.

White dwarf Johnson-Cousins *UBVRI* magnitudes were obtained from the evolutionary tracks detailed in the previous section (Serenelli et al., 2001; Renedo et al., 2010; Althaus et al., 2007). To transform to the SDSS *ugriz* system we simply followed the procedure detailed in Jordi et al. (2006). The photometry of the companion stars was obtained as follows. We first used the empirical spectral type-mass relation of Rebassa-Mansergas et al. (2007) and obtained the spectral type of the secondary stars (note that the secondary star mass is known from the Monte Carlo simulator). This relation is only defined for M-dwarfs ($M \lesssim 0.45 M_{\odot}$), however, as it will be shown later (in Sect. 6.2.3), WD+MS pairs containing earlier type secondary stars are excluded from the simulated sample as a consequence of selection effects affecting the observed population of PCEBs. For each spectral type we then obtained average $u - g$, $g - r$, $r - i$ and $i - z$ colors. These were obtained fitting a large sample of SDSS M-dwarfs (West et al., 2008) to the M-dwarf templates of Rebassa-Mansergas et al. (2007). Once $\sim 25 - 30$ stars were fitted for each spectral type, we then calculated the above mentioned colors using the available SDSS unreddened magnitudes of the considered M-dwarfs and averaged them. Our average colors are in very good agreement with those of West (2011) for $g - r$, $r - i$ and

$i - z$. For $u - g$ this exercise works relatively well for spectral types M0–5, however it becomes rather uncertain for later spectral types. To avoid this we searched for nearby late-type M-dwarfs ($>M5$) in the sample of Bochanski et al. (2011) with available un-reddened magnitudes in SDSS and averaged their $u - g$ colors. This dramatically reduced the uncertainties. Once the average colors were obtained we used the empirical $M_r - (r - i)$ and $M_r - (i - z)$ relations of Bochanski (2008) to obtain M_r . This, together with the known distance from the Monte Carlo simulator, gives r . The remaining $ugiz$ magnitudes were easily calculated from the average colors.

Once the SDSS $ugriz$ magnitudes of the two binary components were obtained, we added the corresponding fluxes to obtain the magnitudes of the simulated WD+MS PCEBs. Finally, in order to provide reliable magnitudes and colors (see Sect. 6.2.1) Galactic extinction was incorporated using the model of Hakkila et al. (1997), while the employed color correction was that of Schlegel et al. (1998).

Chapter 3

The contribution of oxygen–neon white dwarfs to the MACHO content of the Galactic Halo

3.1 Introduction

The interpretation of the microlensing results towards the Large Magellanic Cloud (LMC) still remains controversial. While white dwarfs have been proposed to explain these results and, hence, to contribute significantly to the mass budget of our Galaxy, there are also several constraints on the role played by white dwarfs. Massive white dwarfs are thought to be made of a mixture of oxygen and neon. Correspondingly, their cooling rate is larger than those of typical carbon–oxygen white dwarfs and they fade to invisibility in short timescales. Consequently, they constitute a good candidate for explaining the microlensing results. Here we examine in detail this hypothesis by using the most recent and up-to-date cooling tracks for massive white dwarfs and a Monte Carlo simulator which takes into account the most relevant Galactic inputs.

In our study we consider white dwarfs made of carbon and oxygen (CO white dwarfs) and made of oxygen and neon (ONe white dwarfs). We assume that both types of white dwarfs have hydrogen-rich atmospheres and, thus, are of the DA type. White dwarfs with masses smaller than $M_{\text{WD}} = 1.1 M_{\odot}$ are expected to have a CO core, and for them we adopt the cooling tracks of Salaris et al. (2000). White dwarfs with masses larger than $M_{\text{WD}} = 1.1 M_{\odot}$ most probably have ONe cores and for these white dwarfs we adopt the most recent cooling sequences of Althaus et al. (2007). Both sets of cooling sequences incorporate the most accurate physical inputs for the stellar interior (including neutrinos, crystallization and phase separation)

and reproduce the blue turn at low luminosities (Hansen, 1998). Also, the ensemble of cooling sequences used here encompass the full range of interest of white dwarf masses, so a complete coverage of the effects of the mass spectrum of the white dwarf population was taken into account.

In this chapter we analyze if ONe white dwarfs could be responsible of a sizeable fraction of the reported microlensing events towards the LMC. We also check if ONe white dwarfs could be detected in the Hubble Deep Field South and we discuss the contribution of ONe white dwarfs to the baryonic content of the Galaxy.

3.2 Observational results

Despite the increasing number of surveys searching for white dwarfs — like the Sloan Digital Sky Survey (Eisenstein et al., 2008), the 2 Micron All Sky Survey (Cutri et al., 2003), the SuperCosmos Sky Survey (Hambly, Irwin & MacGillivray, 2001), the 2dF QSO Redshift Survey (Vennes et al., 2002), and others — their success in finding halo white dwarfs has been limited. Thus, the observational determination of the halo white dwarf luminosity is still today rather uncertain. In fact, the two attempts to build such a luminosity function (Liebert et al., 1989; Torres et al., 1998) have provided us only with the bright branch of the halo white dwarf luminosity function. Nevertheless, for our purposes this is enough, since we only need a normalization criterion and, hence, only an upper limit to the local density of moderately bright dwarfs is needed. Consequently, we have used the luminosity function of Torres et al. (1998) and we have normalized the local density of white dwarfs obtained from our Monte Carlo simulations to its observed value, $n \sim 9.0 \times 10^{-6} \text{ pc}^{-3}$ for $\log(L/L_{\odot}) \geq -3.5$ — see Fig. 3 of Torres et al. (1998).

On the other hand, Kilic et al. (2005) have recently re-observed the Hubble Deep field south (HDF-S), and have found three white dwarf candidates among several faint blue objects which exhibit significant proper motion and, thus, are assumed to belong to the thick-disk or the halo populations. If in the end these white dwarfs are spectroscopically confirmed it would imply that white dwarfs can account for about $\leq 10\%$ of the Galactic dark matter, which would be consistent with the results of the EROS team, and with previous estimates (Chabrier, 2004).

3.3 Results and discussion

3.3.1 The halo white dwarf luminosity function

From the distribution of white dwarfs obtained using our Monte Carlo simulator we compute the white dwarf luminosity function using the $1/V_{\text{max}}$ method (Schmidt, 1968). It is important to mention at this point that when deriving a luminosity function using the $1/V_{\text{max}}$ method a proper motion cut and a limiting magnitude

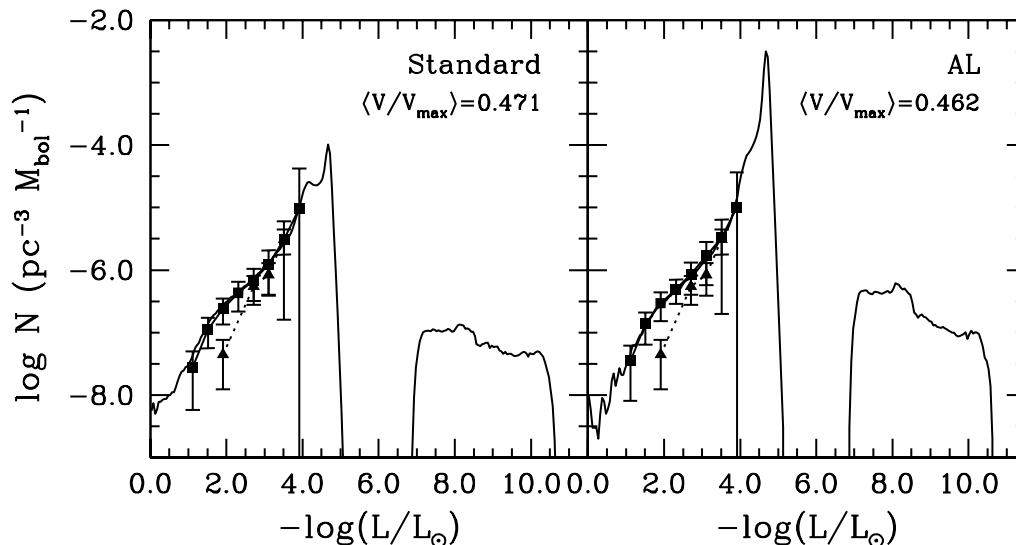


Figure 3.1: Luminosity function of halo white dwarfs for a standard initial mass function (left panel) and a biased initial mass function (right panel). The observational luminosity function of halo white dwarfs is represented using a dotted line (Torres et al., 1998) and solid triangles, while the theoretical luminosity function is shown using a solid line and squares. See text for details.

are required. The set of selection criteria adopted here for computing the halo white dwarf luminosity function is the same used in García-Berro et al. (2004). Namely, we have chosen a limiting magnitude $m_V^{\text{lim}} = 17.5^{\text{mag}}$ and a proper motion cut $\mu \geq 0.16'' \text{ yr}^{-1}$. With all these inputs the luminosity functions of Fig. 3.1 are obtained. The left panel shows the halo white dwarf luminosity function obtained using a standard initial mass function, whereas the right panel shows the luminosity function when the biased initial mass function of Adams & Laughlin (1996) is adopted. The simulated luminosity functions are represented as squares connected by solid lines, whereas the observational luminosity function is represented as triangles connected by dashed lines.

We also recall that, by construction, our samples are complete, although we only select about 10 white dwarfs using the selection criteria discussed before. However, our simulations do provide the whole population of white dwarfs, which is much larger. Hence, we can obtain the *real* luminosity function by simply counting white dwarfs in the computational volume. This is done for all realizations and then we obtain the average. The result is depicted as a solid line in Fig. 3.1. The true luminosity function steadily increases for luminosities larger than $\log(L/L_{\odot}) \simeq -5.0$ and then sharply drops. This drop-off is given by the paucity of CO white dwarfs

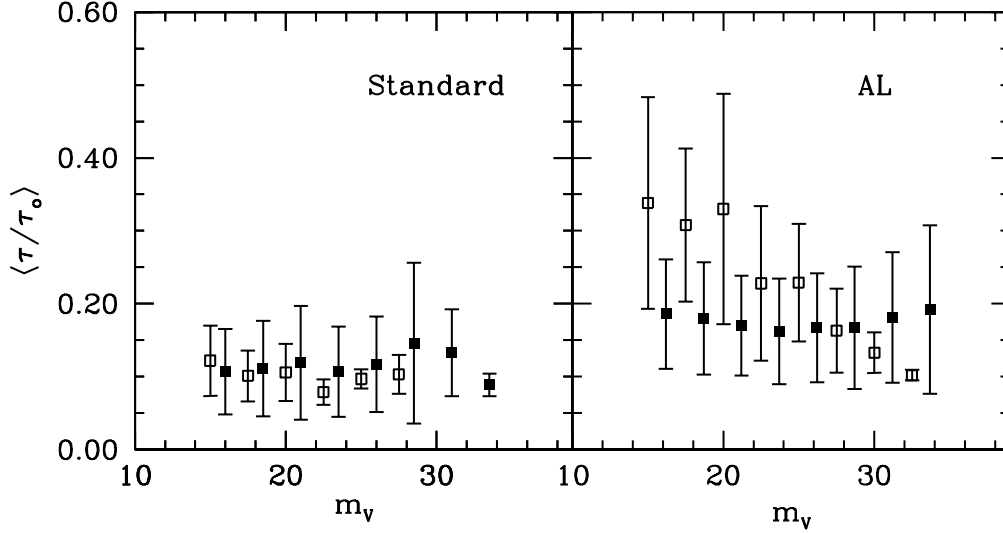


Figure 3.2: Microlensing optical depth towards the LMC as a function of the limiting magnitude. Open and solid symbols represent the population of white dwarfs without and with the contribution of the ONe white dwarfs, respectively. The solid symbols have been shifted for the sake of clarity.

with appropriate ages (14 Gyr). Note however that the bulk of the population of ONe white dwarfs is located at much smaller luminosities, a consequence of the much shorter cooling timescales of these white dwarfs. In fact, for a typical halo age of 14 Gyr, the bulk of the ONe white dwarf population has already entered in the fast Debye cooling phase and, consequently, would not be detectable with the current observational facilities.

In the next section we explore if these white dwarfs contribute significantly to the microlensing optical depth. It is also important to note that with the adopted limiting magnitude and proper motion cut we obtain simulated white dwarf luminosity functions which are totally compatible with the observational one. Hence, the inclusion of massive ONe white dwarfs does not appreciably change the resulting white dwarf luminosity function, which is very similar to that obtained by García-Berro et al. (2004).

3.3.2 Optical depth towards the LMC

First of all, we analyze the result obtained by the MACHO collaboration. In Fig. 3.2 we show the contribution to the optical depth towards the LMC due to the white dwarf population as a function of the adopted limiting magnitude. The results have

	Standard				AL			
Magnitude	17.5	22.5	27.5	32.5	17.5	22.5	27.5	32.5
$\langle N_{\text{WD}} \rangle$	0 ± 1	0 ± 1	0 ± 1	0 ± 1	3 ± 3	2 ± 2	1 ± 1	0 ± 2
$\langle m \rangle (M/M_{\odot})$	0.593	0.599	0.619	0.888	0.636	0.638	0.651	0.684
$\langle \mu \rangle ('' \text{ yr}^{-1})$	0.018	0.015	0.009	0.004	0.038	0.025	0.010	0.003
$\langle d \rangle (\text{kpc})$	2.85	3.52	6.27	14.65	1.31	2.22	5.45	18.73
$\langle V_{\text{tan}} \rangle (\text{km s}^{-1})$	238	243	262	268	240	260	257	279
$\langle \hat{t}_{\text{E}} \rangle (\text{d})$	56.6	59.8	82.4	121.2	34.9	48.0	76.6	129.7
$\langle \tau/\tau_0 \rangle$	0.139	0.134	0.187	0.131	0.180	0.162	0.167	0.192

Table 3.1: Summary of the results obtained for the simulation of microlenses towards the LMC for the MACHO model for an age of the halo of 14 Gyr, different model IMFs, and several magnitude cuts.

been normalized to the value derived by Alcock et al. (2000), $\tau_0 = 1.2 \times 10^{-7}$. The open symbols represent the contribution if only CO white dwarfs are taken into account, while the solid symbols show the contribution to the microlensing optical depth when both CO and ONe white dwarfs are correctly included in the model white dwarf population. As can be seen, for none of the adopted initial mass functions the inclusion of the ONe white dwarf population significantly increases the contribution of white dwarfs to the microlensing optical depth towards the LMC, despite the fact that ONe white dwarfs are much fainter than regular CO white dwarfs (see also Fig. 3.1). Specifically, the contribution of the white dwarf population is, respectively, of the order of 10% for the case of the standard initial mass function and somewhat larger ($\sim 15\%$) for the log-normal initial mass function of Adams & Laughlin (1996). These figures are comparable to those already found in García-Berro et al. (2004). The only differences are that in the case of the standard mass function the contribution of ONe white dwarfs to the microlensing optical depth is clearly dominant only when the adopted limiting magnitude is of the order of 30, which is a totally unrealistic value. For the case of the log-normal initial mass function the results presented here show that the contribution is nearly constant, independently of the adopted limiting magnitude, whereas when only the contribution of CO white dwarfs was considered the contribution to the optical depth of the halo white dwarf population was clearly decreasing for increasing magnitude cuts.

A summary of the results obtained with our Monte Carlo simulator can be found in Table 3.1, where we show for four selected magnitude cuts the number of microlensing events, the average mass of the microlenses, their average proper motion, distance and tangential velocity, the corresponding Einstein crossing times and, finally, the contribution to the microlensing optical depth. It is important to discuss some of the numerical values in Table 3.1. For instance, it is clear that the larger the magnitude cut is, the more massive is the average mass of the lenses, as it should be

	Standard				AL			
Magnitude	17.5	22.5	27.5	32.5	17.5	22.5	27.5	32.5
$\langle m \rangle$ (M/M_\odot)	1.118	1.106	1.244	1.130	1.092	1.082	1.083	1.101
$\langle d \rangle$ (kpc)	4.95	3.98	2.83	3.80	2.31	2.02	2.84	5.75
$\langle V_{\text{tan}} \rangle$ (km s^{-1})	253	257	250	250	266	255	250	269
$\langle t_E \rangle$ (d)	107.9	91.6	77.7	104.1	56.8	61.6	75.0	99.0

Table 3.2: Average values for the ONe white dwarf population.

expected from Fig. 3.2. In particular, for the case in which a standard initial mass function is used we obtain that for the largest limiting magnitude the average mass is $\sim 0.9 M_\odot$, indicating that in a sizeable fraction of the Monte Carlo realizations the lens is an ONe white dwarf. Also, the log–normal initial mass function produces more microlensing events, as one should expect, given that this biased initial mass function was tailored to produce more microlensing events. In fact for this initial mass function a maximum number of 6 microlensing events should be expected, while for the standard initial mass function we should expect 1 microlensing event, at most. However, the contribution to the microlensing optical depth is only slightly larger for the initial mass function of Adams & Laughlin (1996). The reason for this that the microlensing events for this distribution have shorter Einstein crossing times, as can be seen in Table 3.1.

The results obtained so far are not evident at first glance, since one may expect that ONe white dwarfs should be good microlensing candidates. As previously mentioned, ONe white dwarfs have a faster cooling rate than that of CO white dwarfs and, consequently, they reach much fainter magnitudes. Hence, one should naively expect that the probability that a ONe white dwarf could produce a microlensing event would be larger than that of a CO white dwarf, given that practically all ONe white dwarfs have magnitudes larger than the magnitude cuts adopted here. However, even if this is indeed the case, we have shown that the total contribution of ONe white dwarfs is almost negligible. To clarify this result we have analyzed the fraction of microlenses due to ONe white dwarfs with respect to that of the total population. In Fig. 3.3 we show this fraction as a function of the limiting magnitude for the two initial mass functions under study. As can be seen, the contribution of ONe white dwarfs is small for limiting magnitudes below 25^{mag} . Specifically, for the case of the standard initial mass function they only contribute a modest 2%, whereas for the log–normal initial mass function the contribution is halved. This situation only reverses when magnitude cuts larger than $\sim 27^{\text{mag}}$ are adopted. This result by itself is not explanatory of why the contribution of ONe white dwarfs is not significant. We recall here that the contribution of an object to the total optical depth is given by Eq. (2.4), which depends on the Einstein crossing time which, in turn, depends on the Einstein radius and on the transverse velocity of the lens, $t_E = r_E/v_{\text{tan}}$. The

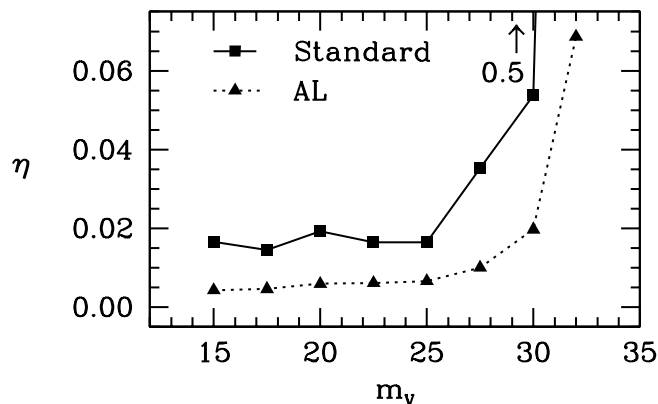


Figure 3.3: Fraction of microlenses due to ONe white dwarfs with respect to the whole population of white dwarfs for the standard initial mass function — squares — and for the log-normal initial mass function of Adams & Laughlin (1996) — triangles.

Einstein radius scales as the root of the mass of the object and it also depends on the lens-object distance — see Eq. (2.3). We note that average mass of an ONe white dwarf is larger than that of a CO white dwarf. Also, given the intrinsic faintness of ONe white dwarfs, their spatial distribution in the computational volume is different because we are selecting microlensing candidates with magnitudes fainter than a given limiting magnitude. Thus, it can be expected that the contribution to the optical depth of an representative object of the these two populations should be different as well.

In Table 3.2 we show the average parameters of the ONe white dwarf population susceptible to produce a microlensing event. The average mass of an ONe white dwarf is $\simeq 1.1 M_{\odot}$, while for a CO white dwarf it is $\simeq 0.6 M_{\odot}$. On the other hand, the average distance of ONe white dwarfs is in the range between ≈ 2 and 4 kpc, independently of the limiting magnitude, while for the CO white dwarf population the average distance increases for increasing magnitude cuts. Finally, the average tangential velocities are very similar for all the magnitude cuts, given that the selection criteria are independent of the kinematics properties of the sample. With these data and using Eq. (2.3) and Eq. (2.4) the ratio of the contribution to the optical depth of a typical ONe white dwarf with respect to the contribution of a typical CO white dwarf is

$$\frac{\tau_{\text{ONe}}}{\tau_{\text{CO}}} = \frac{\hat{t}_{\text{ONe}}}{\hat{t}_{\text{CO}}} \frac{\varepsilon(\hat{t}_{\text{CO}})}{\varepsilon(\hat{t}_{\text{ONe}})} \approx \sqrt{\frac{M_{\text{ONe}} D_{\text{OL}}^{\text{ONe}}}{M_{\text{CO}} D_{\text{OL}}^{\text{CO}}}} \frac{\varepsilon(\hat{t}_{\text{CO}})}{\varepsilon(\hat{t}_{\text{ONe}})} \quad (3.1)$$

This ratio turns out to be $\tau_{\text{ONe}}/\tau_{\text{CO}} \approx 1.5$. Recalling that the fraction η of ONe white dwarfs for limiting magnitudes fainter than 25^{mag} is typically 0.02 for the standard initial mass function and 0.01 for the biased initial mass function, the

	Standard			AL		
Magnitude	17.5	22.5	27.5	17.5	22.5	27.5
$\langle N_{\text{WD}} \rangle$	0 ± 1	0 ± 1	0 ± 1	1 ± 2	1 ± 2	0 ± 2
$\langle m \rangle (M/M_{\odot})$	0.607	0.595	0.622	0.631	0.634	0.642
$\langle \mu \rangle ('' \text{ yr}^{-1})$	0.013	0.011	0.008	0.034	0.025	0.010
$\langle d \rangle (\text{kpc})$	4.29	4.52	6.71	1.50	2.03	5.39
$\langle V_{\text{tan}} \rangle (\text{km s}^{-1})$	256	239	246	240	244	258
$\langle \hat{t}_{\text{E}} \rangle (\text{d})$	64.9	77.0	89.7	37.9	45.3	74.8
$\langle \tau/\tau_0 \rangle$	0.344	0.372	0.392	0.368	0.384	0.505

Table 3.3: Summary of the results obtained for the simulation of microlenses towards the LMC for the EROS model for an age of the halo of 14 Gyr, different model IMFs, and several magnitude cuts.

increment in the total optical depth due to ONe white dwarfs can be estimated to be

$$\frac{\Delta\tau}{\tau_0} \approx \eta \frac{\tau_{\text{ONe}}}{\tau_{\text{CO}}}, \quad (3.2)$$

which represents an increment of roughly 3% for the case in which a standard initial mass function is considered and a 2% increment for the case of the log–normal initial mass function. These results are in nice agreement with those previously presented in Fig. 3.1. On the other hand, when the magnitude cut is 30^{mag} the fraction of ONe microlenses η increases significantly and, thus, the fractional increase of the optical depth due to ONe white dwarfs consequently increases, reaching values as high as 100%. This fact is the responsible for different behaviour of the deepest magnitude bins of the left panel of Fig. 3.1, which show the situation for the standard initial mass function. The biased initial mass function suppresses the formation of moderately massive ONe white dwarfs, and this is the reason why these faintest luminosity bins are not as populated as the equivalent bins for the case in which a standard mass function is considered.

In a second set of Monte Carlo calculations we have simulated the observational data obtained by the EROS team. We recall here that the EROS collaboration have not found any microlensing event towards the LMC and one candidate event towards the SMC. Adopting a standard halo model and assuming $\tau_{\text{SMC}} = 1.4\tau_{\text{LMC}}$, the EROS results imply an optical depth $\tau_0 = 0.36 \times 10^{-7}$ (Tisserand et al., 2007), which is four times smaller than that obtained by the MACHO team. Although it is expected that the value of the optical depth obtained from our simulations should be only slightly different, it is as well true that this may be a test of the robustness of our numerical procedures. In particular, the detection efficiency of both experiments is very different. Additionally, the areas (and the number of objects) surveyed by

both teams are different. The results are summarized in Table 3.3. Our simulations show that the white dwarf population could account for a 35% of the optical depth found by the EROS team if a standard initial mass function is adopted, while for the non-standard initial mass function the contribution of the white dwarf population could be as large as 50%. On the other hand, the expected number of objects has an upper limit of 1 for the standard initial mass function and 2 for the log-normal initial mass function. Both results are in agreement with the results of the EROS experiment. Again, as it was the case for the simulation of the MACHO experiment, the contribution of ONe white dwarfs is small. All in all, it seems that the microlensing optical depth obtained by the MACHO collaboration is a clear overestimate.

3.3.3 The Hubble Deep Field South

We have performed a series of Monte Carlo simulations in the direction of the HDF-S ($l = 328.25^\circ$ $b = -49.21^\circ$) for a small window of 4.062 arcmin^2 . We have used the Johnson-Cousins *UBVRI* system instead of the WFPC2 photometry because the differences between both photometric systems is smaller than 0.02^{mag} for the range of colors under study (Holtzman et al., 1995). Also, no reddening was applied to the synthetic white dwarf stars. Contrary to what has been done until now the results presented in next section are the average of 10^3 different realizations. Each of these realizations has been normalized to the local density of halo white dwarfs as previously described in the preceding sections.

In Fig. 3.4 we represent two typical simulations for the halo white dwarf population in the direction of the HDF-S for the two initial mass functions under study. As can be seen, the number of white dwarfs susceptible to be detected in the HDF-S survey — that is, those with I magnitude smaller than 27^{mag} — is substantially larger for the log-normal initial mass function of Adams & Laughlin (1996) than for the standard initial mass function. Specifically, the average number of objects with $I < 27^{\text{mag}}$ turns out to be 6 ± 2 for the case in which a standard initial mass function is adopted, while for the log-normal initial mass function this number is 110 ± 8 . However, and in order to avoid confusion with blue extragalactic objects and main sequence stars, Kilic et al. (2005) restricted their search for white dwarfs candidates to colors in the range $V - I < 0.4$. Adding this new restriction we obtain that the expected number of white dwarfs should be 1 ± 1 for both initial mass functions. Although this result implies that both initial mass functions are compatible with the observations, the log-normal initial mass function produces a large number of white dwarfs with colors in the interval $0.6 < V - I < 1.4$, which has no observational counterpart.

Additionally, in Fig. 3.4 we also show the only one ONe white dwarf obtained for each one of these two typical simulations. In both cases its location is shown as an encircled dot in the color-magnitude diagram. It is worth mentioning that in

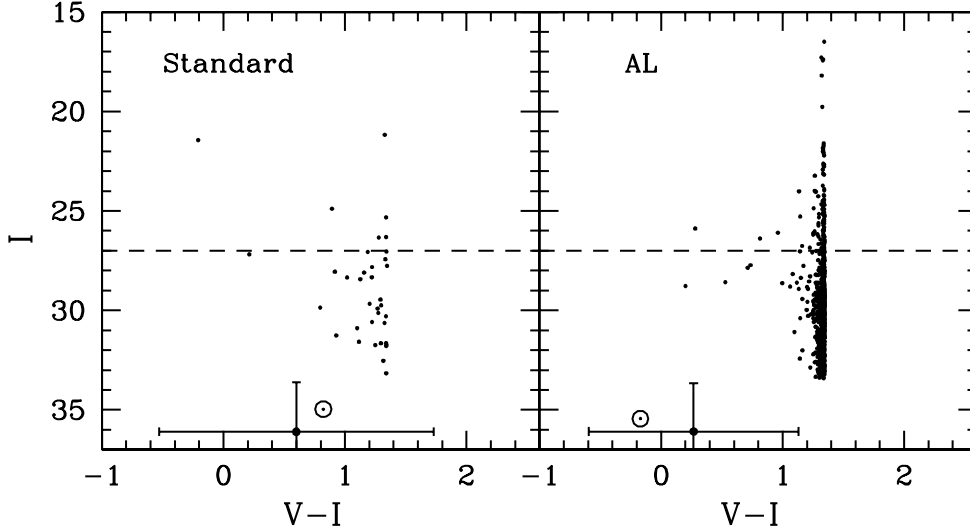


Figure 3.4: Color–magnitude diagram for the white dwarf distribution (ONe white dwarfs are circled) for the HDF–S of two typical simulations. The dashed line represents the HDF–S observational limit. Also represented is the average expected location within 1σ error of a typical ONe white dwarf. See text for details.

most of the 10^3 realizations an ONe white dwarf is found, and thus we also show the average location of ONe white dwarfs in the color–magnitude diagram, along with the corresponding 1σ error bars. Note that in any case ONe white dwarfs are much fainter and bluer than normal CO white dwarfs, as it should be expected given that for a typical age of the halo most ONe white dwarfs have already reached the blue hook in the color–magnitude diagram.

3.3.4 The dark matter density

The results discussed so far indicate that, even in the case in which the contribution of ONe white dwarfs is taken into account, only a small fraction of the microlensing optical depth towards the LMC can be attributed to white dwarfs. We recall that if we adopt the microlensing optical depth of the MACHO experiment this contribution is nearly a 20% for the biased initial mass function of Adams & Laughlin (1996) and $\sim 10\%$ for the standard initial mass function. Besides, for a spherical isothermal halo model the microlensing optical depth towards the LMC is given by the expression (Alcock et al., 2000; Griest, 1991):

$$\tau_{\text{LMC}} = 5.1 \times 10^{-7} f \quad (3.3)$$

	Standard		AL	
	CO	ONe	CO	ONe
ISM	1.1×10^{-4}	6.4×10^{-6}	2.8×10^{-3}	3.5×10^{-5}
WD	5.4×10^{-5}	9.5×10^{-7}	9.2×10^{-4}	5.3×10^{-6}

Table 3.4: Density of baryonic matter (M_{\odot}/pc^3) in the Galactic halo within 300 pc from the Sun in the form gas returned to the interstellar medium (ISM) and in the form of white dwarfs (WD).

where f is the fraction of the halo mass that is made of lensing objects. Thus, the white dwarf population would contribute $f \approx 0.05$ to the mass of the halo in the most optimistic case.

However, we can go one step beyond using the results of our Monte Carlo simulations. In particular, we can compute the baryonic dark matter density in the form of white dwarfs using the $1/V_{\text{max}}$ method. We proceed as follows. For each star of the sample we determine the maximum volume over which each star can contribute as a microlensing event using the expression

$$V_{\text{max}} = \frac{\Omega}{3}(r_{\text{max}}^3 - r_{\text{min}}^3) \quad (3.4)$$

where r_{max} is the radius of the volume in which we distribute the objects of our sample, which in our case is the radius of Galactic halo, and r_{min} is the minimum volume for which a white dwarf still belongs to the sample considering its apparent magnitude to be fainter than the adopted magnitude cut. Then, the number density of white dwarfs is

$$n = \sum_{i=1}^{N_{\text{obj}}} \frac{1}{V_{\text{max}_i}}. \quad (3.5)$$

Using this procedure we find that the contribution of white dwarfs to the baryonic dark matter would be roughly a 3% in the case in which a standard initial mass function is considered and nearly a 5% for the case in which the initial mass function of Adams & Laughlin (1996) is adopted.

Finally, from our Monte Carlo simulations we can also derive the *total* density of baryonic matter in the Galactic halo within 300 pc from the Sun in the form of main sequence stars, stellar remnants and in the corresponding ejected mass. We obtain $\rho_0 = 2.6 \times 10^{-4} M_{\odot} \text{ pc}^{-3}$ for the standard initial mass function and $3.8 \times 10^{-3} M_{\odot} \text{ pc}^{-3}$ for the log-normal initial mass function. The respective contributions of CO and ONe white dwarfs to the mass budget and of the mass returned to the interstellar medium are also shown in Table 3.4. Note that the total contribution of ONe white dwarfs is rather limited. The total density of baryonic matter obtained

from our Monte Carlo simulations can be compared as well with the local dynamical matter density:

$$\rho_{\text{DM}} = \frac{v_{\text{rot}}^2}{4\pi G R_{\odot}^2}, \quad (3.6)$$

where v_{rot} is the rotation velocity of the Galaxy and R_{\odot} is the Galactocentric distance. Thus, the fraction η of baryonic matter of the Galaxy resulting from the white dwarf population can be estimated. Our results indicate that η would be a modest 0.02 for the case in which a standard initial mass function is adopted, whereas a sizeable fraction of the baryonic matter, $\eta = 0.52$, can be accounted if the initial mass function of Adams & Laughlin (1996) is assumed.

3.4 Conclusions

We have analyzed the contribution of ONe white dwarfs to the MACHO content of the Galactic halo. We find that although ONe white dwarfs fade to invisibility very rapidly and, thus, they are good baryonic dark matter candidates, their contribution to the microlensing optical depth towards the LMC is rather limited. In particular, we have found that when the contribution of ONe white dwarfs is taken into account the microlensing optical depth does not increase significantly, independently of the adopted initial mass function. If the microlensing optical depth is adopted to be that of the MACHO experiment, $\tau_0 = 1.2 \times 10^{-7}$ (Alcock et al., 2000) — which probably is an overestimate — we find that the fraction of the microlensing optical depth due to the whole white dwarf population is at most $\sim 13\%$ in the case in which a standard initial mass function is adopted and $\sim 19\%$ if the log-normal initial mass function of Adams & Laughlin (1996) is considered. These values are roughly $\sim 3\%$ larger than those already found by García-Berro et al. (2004), who only considered the contribution of CO white dwarfs. We have also studied if some of the candidate white dwarfs of the Hubble Deep Field South could be ONe white dwarfs and we have found that most probably this is not the case. Finally, we have also discussed the contribution of the whole white dwarf population to the mass of the Galactic halo. We have found that this contribution is of the order of a modest 5% in the most optimistic case. All in all, we conclude that white dwarfs are not significant contributors to the mass of the Galactic halo.

Chapter 4

The contribution of red dwarfs and white dwarfs to the halo dark matter

4.1 Introduction

In the previous chapter, we scrutinized the role played by the population of oxygen–neon (ONe) white dwarfs in addition to that of (CO) carbon–oxygen white dwarfs as possible contributors to the halo dark matter. A wide range of Galactic inputs, including different initial mass functions and halo ages, and several density profiles corresponding to different halo models, were appraised. The calculations indicated that a sizeable fraction of the halo dark matter cannot be locked in the form of white dwarfs. We found that the contribution of white dwarfs is, in fact, approximately a modest 5% in the most optimistic case. This contribution is mainly due to old CO white dwarfs with hydrogen-rich atmospheres and the contribution of ONe white dwarfs with hydrogen atmospheres is minor, because although ONe white dwarfs can reach fainter magnitudes more rapidly than CO ones, their contribution is heavily suppressed by the initial mass function.

In this chapter we extend our Monte Carlo simulator and we add the red-dwarf population. We analyze, in a comprehensive way, a significant range of masses $0.08 < M/M_{\odot} < 10$ likely to produce microlensing events towards the LMC and, thus, to contribute to the halo dark matter. This mass range represents almost 90% of the stellar content, including the red-dwarf regime ($M > 0.075 M_{\odot}$), the CO white-dwarf population, and the population of massive ONe white dwarfs. Our goal is to evaluate the contribution of the population of red dwarfs to the microlensing optical depth towards the LMC, besides that of white dwarfs. The results will be compared to those of the MACHO and EROS teams. We will also estimate the probability that a microlensing event could be assigned to one or another of the populations under

study and we will discuss the contribution of red and white dwarfs to the baryonic content of the Galaxy.

4.2 Expanding the model

We have expanded of our Monte Carlo simulator, presented in previous chapters, by adding the population of red dwarfs. In order to do this, we proceed as follows. As soon as the mass of a synthetic star is chosen, its main-sequence lifetime is inferred and we are able to determine which stars evolved into white dwarfs and which ones remain on the main sequence as red dwarfs. We considered red dwarfs to have masses in the range $0.08 < M/M_{\odot} < 1$. For these stars, we adopted the evolutionary models of Baraffe et al. (1998). Stars with such small masses have large main-sequence lifetimes. Therefore, no post-main-sequence evolutionary tracks of these stars were required.

As we did in the previous chapter, the mass distribution of synthetic stars was computed using two different initial mass functions, the standard initial mass function of Scalo (1998) and the biased log-normal initial mass function proposed by Adams & Laughlin (1996). We note, however, that any kind of biased initial mass functions appear to be incompatible with the observed properties of the halo white-dwarf population Isern et al. (1998); García-Berro et al. (2004), with the contribution of thermonuclear supernovae to the metallicity of the Galactic halo Canal et al. (1997), and with the observations of galactic halos in deep galaxy surveys Charlot & Silk (1995). For the sake of completeness we prefer, however, to include a representative example of these biased mass functions to illustrate the role played by the red dwarf population when a biased initial mass function is adopted.

Finally, to compare the simulated results with the observational ones, a normalization criterion should be used. We have proceeded as in our previous chapter. That is, we have normalized our simulations to the local density of halo white dwarfs obtained from the halo white dwarf luminosity function of Torres et al. (1998) taking into account the new halo white dwarf candidates in the SDSS Stripe 82 (Vidrih et al., 2007).

4.3 Results and discussion

4.3.1 Optical depth towards the LMC

As previously mentioned, the optical depth provides the utmost, immediate and simplest information about the microlensing experiments. Even so, the optical depth plays a critical role in our analysis, since it provides a wealth of information about the Galactic halo and the presence of dark matter. We compare results obtained using our Monte Carlo simulator with those derived by the MACHO collaboration.

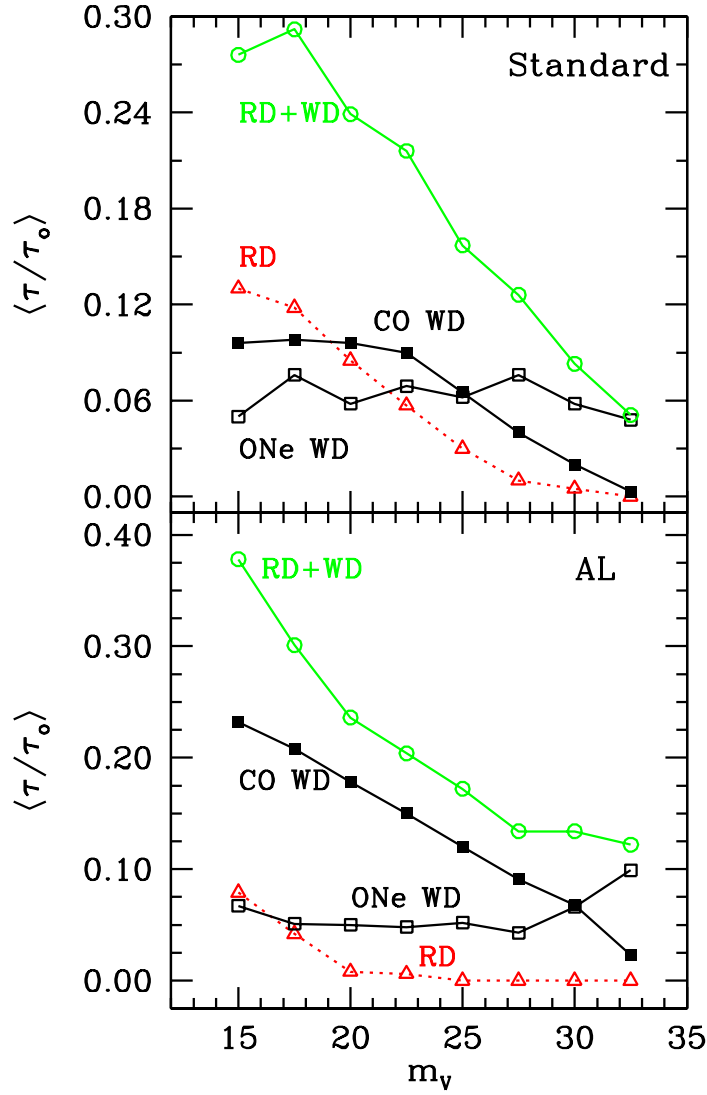


Figure 4.1: Microlensing optical depth towards the LMC as a function of the limiting magnitude. Solid and open squares represent the CO and ONe white dwarf populations, respectively. Red dwarfs are represented using open triangles, while the entire population is shown using open circles.

In Fig. 4.1 we present the contribution of the different simulated populations to the optical depth, for the two initial mass function studied, as a function of the adopted magnitude cut. Our simulations were normalized to the value of the optical depth derived by Alcock et al. (2000), $\tau_0 = 1.2 \times 10^{-7}$. The white-dwarf populations are

	Standard				AL			
Magnitude	17.5	22.5	27.5	32.5	17.5	22.5	27.5	32.5
$\langle N_{\text{WD}} \rangle$	0 ± 1	0 ± 1	0 ± 1	0 ± 1	3 ± 2	2 ± 1	1 ± 1	0 ± 1
$\langle m \rangle (M/M_{\odot})$	0.421	0.411	0.427	0.443	0.638	0.636	0.640	0.684
$\langle \mu \rangle ('' \text{ yr}^{-1})$	0.020	0.017	0.008	0.004	0.036	0.025	0.011	0.003
$\langle d \rangle (\text{kpc})$	2.48	3.79	6.62	13.08	1.39	2.15	5.13	19.6
$\langle V_{\text{tan}} \rangle (\text{km s}^{-1})$	240	247	262	241	240	252	263	261
$\langle \hat{t}_{\text{E}} \rangle (\text{d})$	41.2	49.3	63.3	82.8	34.7	46.6	76.4	126.8
$\langle \tau/\tau_0 \rangle$	0.283	0.214	0.139	0.055	0.302	0.204	0.140	0.129

Table 4.1: Summary of the results obtained for whole population simulation of microlenses towards the LMC for an age of the halo of 14 Gyr, different model initial mass functions, and several magnitude cuts.

represented by solid and open squares for the CO and ONe white dwarfs, respectively. Open triangles indicate the contribution of red dwarfs, while the contribution of the three populations is represented by open circles. The first remarkable result is that, for the standard initial mass function — top panel of Fig. 4.1) — the combined contribution of red dwarfs and white dwarfs is at most one third of the observed optical depth, when a totally unrealistic magnitude cut is adopted, $m_V \sim 15^{\text{mag}}$. Second, there is a clearly decreasing trend as the adopted magnitude cut is increased. This can be easily understood, since fewer objects contribute to the optical depth as the magnitude cut increases. Furthermore, the slope of the distributions is different for the three types of objects considered. For instance, the contribution of red dwarfs decreases faster than the contribution of CO white dwarfs as the magnitude cut increases, which, in turn, decreases faster than the contribution of ONe white dwarfs. This reflects the fact that, in general, red dwarfs are brighter than regular, CO white dwarfs. Finally, ONe white dwarfs cool rapidly (Althaus et al., 2007) and thus, for realistic halo ages, are faint objects. Consequently, their contribution remains almost constant. We note that the optical depth, measured for the entire population, almost doubles that obtained when the white-dwarf population alone is considered. The value measured remains, however, far below the observed value, which agrees with other studies. It is clear that the mass of a Galactic halo population cannot fully explain the results of the MACHO team. Even the alternative initial mass functions, of which that of (Adams & Laughlin, 1996) is a representative example, predict that $\langle \tau/\tau_0 \rangle$ in the best of the cases — see the bottom panel of Fig. 4.1.

The results obtained using the non-standard initial mass function deserve two additional comments. In particular, we note that the largest contribution to the optical depth measurement is made by the CO white-dwarf population and, secondly, that the contribution of red dwarfs is negligible for magnitude cuts larger than $\sim 23^{\text{mag}}$, which is a reasonable value for current surveys. Both facts are unsurprising

	Standard				AL			
Magnitude	17.5	22.5	27.5	32.5	17.5	22.5	27.5	32.5
$\langle N_{\text{WD}} \rangle$	0 ± 1	0 ± 1	0 ± 1	0 ± 1	0 ± 1	0 ± 1	0 ± 0	0 ± 0
$\langle m \rangle (M/M_{\odot})$	0.324	0.228	0.119	0.092	0.747	0.622	—	—
$\langle \mu \rangle ('' \text{ yr}^{-1})$	0.018	0.011	0.006	0.005	0.010	0.002	—	—
$\langle d \rangle (\text{kpc})$	2.89	4.88	8.27	10.20	5.15	17.59	—	—
$\langle V_{\text{tan}} \rangle (\text{km s}^{-1})$	242	244	254	235	246	180	—	—
$\langle \hat{t}_{\text{E}} \rangle (\text{d})$	41.2	48.5	41.3	43.3	98.2	158.0	—	—
$\langle \tau/\tau_0 \rangle$	0.130	0.118	0.096	0.070	0.091	0.125	—	—

Table 4.2: Summary of the results obtained for the population of red dwarf microlenses towards the LMC for an age of the halo of 14 Gyr, different model initial mass functions, and several magnitude cuts.

since this particular initial mass function was tailored to produce a large population of $0.5 M_{\odot}$ white dwarfs. In summary, we find that, for the mass range considered, a model stellar halo produces a microlensing optical-depth that is at most one third of that measured by the MACHO team, independently of the adopted initial mass function.

In Table 4.1 we summarize the average values of parameters of the entire population for the two initial mass functions and four magnitude cuts, that is, we present the number of microlensing events, the average mass of the microlenses, their average proper motion, distance and tangential velocity, the corresponding Einstein crossing times and, finally, the contribution to the microlensing optical depth. It is clear that some parameters are dependent of the magnitude cut. For instance, the average distance of the sample increases as the magnitude cut is larger. This is a natural consequence of selecting more distant objects which, in turn, implies longer Einstein crossing times. This behavior is independent of the assumed initial mass function. However, there are characteristics which do not change as the magnitude cut increases, for instance, the expected number of events or the average mass of the sample. In the case of a standard initial mass function, no more than one microlensing event should be expected at the 1σ confidence level, while for a log-normal mass function up to 5 events might be expected. In any case, the expected number of microlensing events is far from the 17 events claimed by the MACHO experiment.

As already mentioned, the average mass of the microlenses depends on the initial mass function. To investigate this further in Fig. 4.2, the contribution to the optical depth as a function of the mass of the lens object for both initial mass functions, is shown. The results obtained with our Monte Carlo simulator clearly show that for a standard initial mass function (shown in the top panel of Fig. 4.2) there are two peaks centered at masses $\sim 0.3 M_{\odot}$ and $\sim 0.6 M_{\odot}$, respectively. These masses correspond to the average masses of red dwarfs and CO white dwarfs, respectively.

We note that, in the case of a standard initial mass function, the contribution of ONe white dwarfs appears as an extended tail. This agrees with studies of the distribution of masses of the white dwarf population (Finley et al., 1997; Liebert et al., 2005). These studies indicate that a narrow, sharp peak exists close to $0.6 M_{\odot}$, with a tail extending towards larger masses, and that several white dwarfs with spectroscopically determined masses occupy the mass interval between 1.0 and $1.2 M_{\odot}$. The situation is different for the non-standard initial mass function, which is shown in the bottom panel of Fig. 4.2. The log-normal initial mass function considered here cannot produce red dwarfs with masses below $\sim 0.45 M_{\odot}$ and thus the peak at $0.3 M_{\odot}$ previously found is absent in this case.

A more detailed analysis of the role played by the red-dwarf population is possible. In Table 4.2, we summarize the average parameter values of the red-dwarf population for both initial mass functions. Similar sets of data for the white-dwarf population can be found in our previous studies (Camacho et al., 2007; García-Berro et al., 2004). As seen in Table 4.2, the red-dwarf population constitutes roughly 10% of the observed MACHO optical depth for a standard initial mass function. It is also important to discuss the other parameters shown in Table 4.2. For instance, the average mass clearly decreases when the magnitude cut increases, which is the opposite to what occurs for the white-dwarf population. We should expect to find less massive objects for larger magnitude cuts, because the more massive the red dwarf, the brighter it will be. This result is reinforced by the fact that the average distance increases for increasing magnitude cuts. Since the average tangential velocity remains constant, the combined effect of a mass that decreases on average and a distance that increases on average is that the Einstein crossing-time remains almost constant. The characteristics of the red-dwarf population differ significantly when the initial mass function of Adams & Laughlin (1996) is used, since in this case the production of low-mass red dwarfs is heavily suppressed. Accordingly, in our simulations we have not produced red dwarfs with masses smaller than $\sim 0.45 M_{\odot}$. Thus, since the masses on average are larger, we also find brighter stars. We therefore expect no contribution at all for magnitude cuts above 22.5^{mag} , while for brighter magnitude cuts the average mass expected is $\sim 0.7 M_{\odot}$, which is even larger than expected for CO white dwarfs.

For the standard initial mass function, a double-peaked profile is found, as already observed; but the peak amplitude, however, should be analyzed in more detail. The ratio of the contribution to the optical depth of a typical red dwarf with respect to the contribution of a typical CO white dwarf is

$$\frac{\tau_{\text{RD}}}{\tau_{\text{CO}}} = \frac{\hat{t}_{\text{RD}} \varepsilon(\hat{t}_{\text{CO}})}{\hat{t}_{\text{CO}} \varepsilon(\hat{t}_{\text{RD}})} \approx \sqrt{\frac{M_{\text{RD}} D_{\text{OL}}^{\text{RD}} \varepsilon(\hat{t}_{\text{CO}})}{M_{\text{CO}} D_{\text{OL}}^{\text{CO}} \varepsilon(\hat{t}_{\text{RD}})}} \quad (4.1)$$

This value depends on the adopted initial mass function and on the magnitude cut used. For the standard initial mass function and a magnitude cut of 22.5^{mag} the

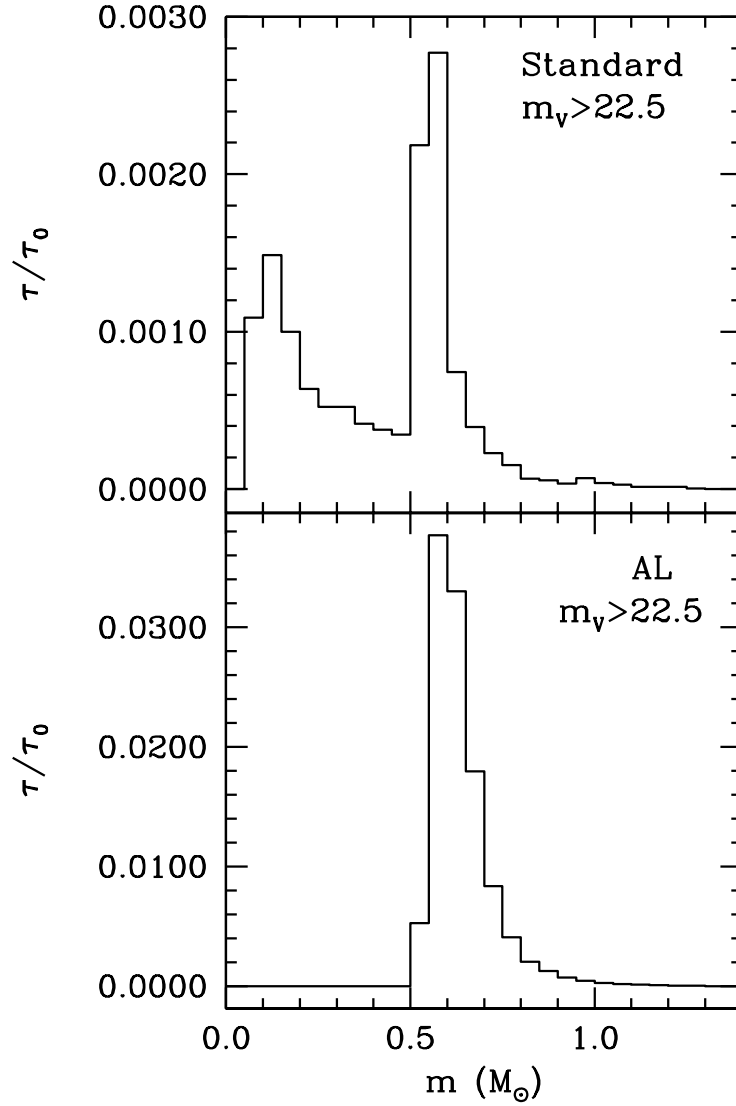


Figure 4.2: Contribution to the optical depth as a function of the lens mass.

average values of the mass and distance of a red dwarf are, respectively, $\sim 0.228 M_{\odot}$ and 4.88 kpc, while for a typical CO white dwarf the average mass is $\sim 0.568 M_{\odot}$ and the average distance is 3.14 kpc. For these values, the ratio of the optical depths is equal to $\tau_{\text{RD}}/\tau_{\text{CO}} \approx 0.9$. Thus, although the sample of red dwarfs and white dwarfs differ, their contribution to the optical depth, per object, remains the same. For instance, the red-dwarf population has a smaller average mass than that of white

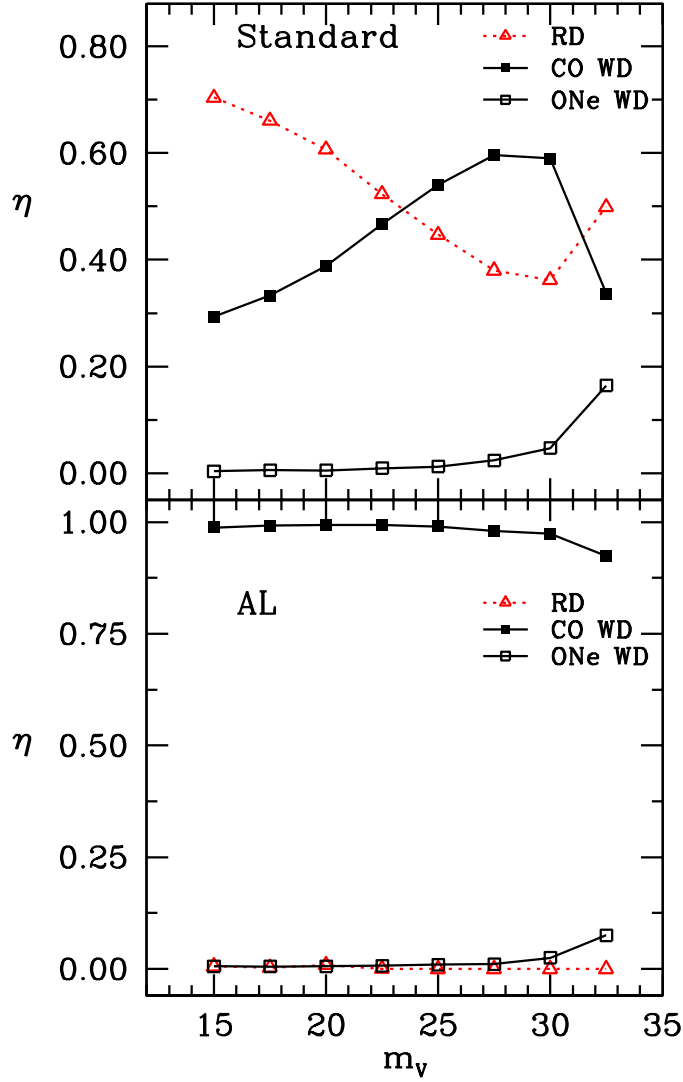


Figure 4.3: Fraction of microlenses with respect to the entire population.

dwarfs but, conversely, the average distance is larger. The total contribution of both populations is therefore the number of microlenses. To clarify this issue, we evaluated the fraction of microlenses, for the different populations, as a function of the adopted magnitude cut. The results are shown in Fig. 4.3 for both the standard initial mass function (top panel) and the log-normal initial mass function (bottom panel).

As can be seen in Fig. 4.3, for the standard initial mass function the relative

contribution of red dwarfs decreases with increasing value of magnitude cuts, while that of CO white dwarfs increases. Both contributions are equal for a magnitude cut of $\approx 24^{\text{mag}}$. Finally, the contribution of ONe white dwarfs remains roughly constant and only becomes significant for large magnitude cuts. These trends can be attributed to the fact that red dwarfs are more numerous at bright magnitudes than white dwarfs, for which typical luminosities are of the order of $\log(L/L_{\odot}) \simeq -3.5$. The situation is completely different when the log-normal initial mass function of Adams & Laughlin (1996) is used. As can be seen in the bottom panel of Fig. 4.3, the number of microlenses is practically dominated by the CO white-dwarf contribution, while the contribution of red dwarfs and ONe white dwarfs is negligible.

4.3.2 The microlensing event rate

As previously pointed out, the contribution to the optical depth for a standard initial mass function is doubled when the red dwarf population is considered. We have also shown that for a standard initial mass function the contributions of red dwarfs and CO white dwarfs are roughly the same. It is natural to ask whether there are differences that can help us to discern the contribution of one or another population, using the observational data of the MACHO experiment. To answer this question we analyzed the microlensing rate as a function of event duration. The results of our simulations, for a standard initial mass function, are shown in Fig. 4.4. Each of the panels is clearly labeled with the adopted magnitude cut and the population of microlenses. In the left panels of Fig. 4.4 we adopted a magnitude cut of 25^{mag} , whilst for the right panels a magnitude cut of 30^{mag} was adopted. In all cases, the simulated microlensing rate is shown using solid lines, while the observational data obtained by the MACHO team is shown using a dotted line. All distributions are normalized to unit area. The red-dwarf and the white-dwarf distributions present some differences. For a magnitude cut of 25^{mag} , the white-dwarf population presents a wider distribution, even though both the red-dwarf population and the white-dwarf populations show a peak located at nearly ~ 20 days. When a magnitude cut of 30^{mag} is adopted, the differences are more pronounced and it is clear that the distribution peak for the CO white-dwarf population moves to longer durations (~ 70 days); in contrast, the peak of the red-dwarf population does not move appreciably.

To be able to attain more quantitative estimates, we performed a Z^2 statistical test of the compatibility of the different populations with the observed data. The Z^2 statistical test (Lucy, 2000) represents an improvement to the standard χ^2 statistical test and was specially developed for small data sets. In Table 4.3, we show the Z^2 probability that the different simulated populations are compatible with the distribution of Einstein times, obtained by the MACHO experiment. It should be clarified that this probability represents an estimate of the degree to which the observed event-rate distribution can be derived from a single population of stars. As

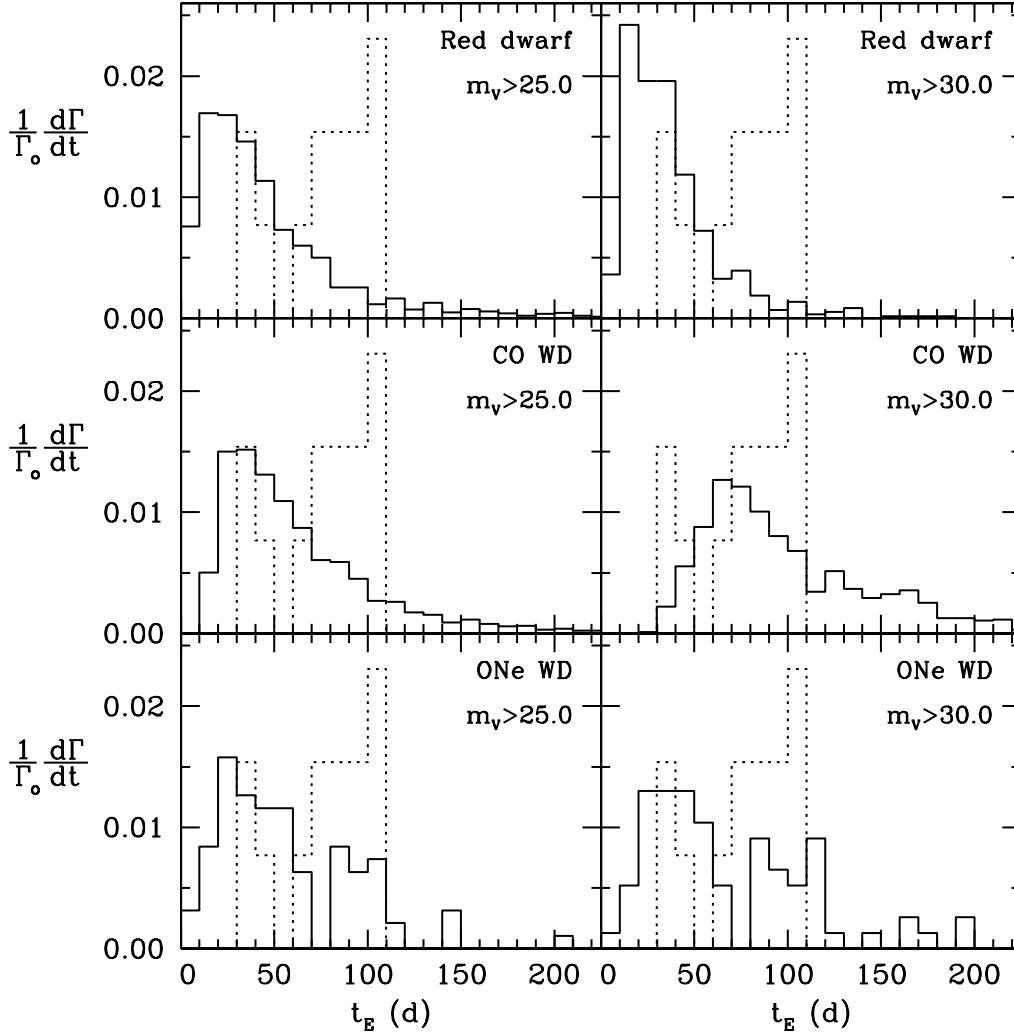


Figure 4.4: Differential event rate normalized to unit area as a function of the Einstein crossing-time for the populations under study and different magnitude cuts (solid lines). The observational event distribution from Alcock et al. (2000) is represented as a dotted line in each panel.

can be seen in Table 4.3, the CO white-dwarf population provides the most appropriate description of the observational data, given that its compatibility is as high as 0.90 for the faintest magnitude cut. Moreover, the compatibility of this population with the observational data increases at fainter magnitude bins. In sharp contrast, the population of red dwarfs presents a decreasing trend as the magnitude cut in-

Z^2 COMPATIBILITY TEST

Magnitude	17.5 ^{mag}	22.5 ^{mag}	25.0 ^{mag}	27.5 ^{mag}	30.0 ^{mag}
Red dwarfs	0.58	0.67	0.65	0.55	0.40
CO white dwarfs	0.61	0.70	0.80	0.87	0.90
ONe white dwarfs	0.76	0.55	0.68	0.68	0.72
Entire population	0.59	0.69	0.75	0.82	0.89

Table 4.3: Compatibility, as obtained using the Z^2 statistical test, of the observed MACHO distribution and the different Monte Carlo simulated populations.

creases and, additionally, the compatibility with the observational data is, at most, 0.70. With regard to the ONe white-dwarf population, the compatibility presents an almost constant value of around 0.70, independently of the magnitude cut. These results indicate that the CO white-dwarf population can reproduce the observed distribution of microlensing event-rates. Even more, they dominate the behavior of the entire population, as can be seen from the final row of Table 4.3, in which we analyze the compatibility of the entire population of simulated stars. Therefore, even if the expected number of microlensing events obtained in our simulations is considerable smaller than the ~ 15 events claimed by the MACHO team, the event rate distribution of the CO white-dwarf population is in fair agreement with the observed distribution. This result places doubt on how well the characteristics of the halo white-dwarf population are known and if there are other ways to produce a larger number of old white dwarfs in the stellar halo.

4.3.3 The EROS experiment

While the MACHO team claim the identification of up to 17 observed events, the EROS collaboration have not found any microlensing event towards the LMC and one candidate event towards the SMC. Adopting a standard halo model and assuming $\tau_{\text{SMC}} = 1.4\tau_{\text{LMC}}$, the EROS results imply an optical depth $\tau_0 = 0.36 \times 10^{-7}$ (Tisserand et al., 2007), which is four times smaller than that obtained by the MACHO team. We performed a set of simulations emulating the conditions of the EROS experiment with inputs similar to those described in the previous chapter. Although only minor differences should be expected in the analysis of the main results, it is clear as well that a joint study of both experiments, using a controlled set of prescriptions, represents a test of the robustness of our numerical procedure.

In Table 4.4, we summarized the results obtained in this second set of Monte Carlo simulations of microlenses towards the LMC, for the EROS experiment. Our simulations show that, for the standard initial mass function, the expected optical depth could be 70% of the value found by the EROS team. The value obtained, when only the white-dwarf population was considered, was previously found to be

	Standard			AL		
Magnitude	17.5	22.5	27.5	17.5	22.5	27.5
$\langle N_{\text{WD}} \rangle$	0 ± 1	0 ± 1	0 ± 1	1 ± 1	1 ± 1	1 ± 1
$\langle m \rangle (M/M_{\odot})$	0.385	0.384	0.427	0.633	0.637	0.637
$\langle \mu \rangle ('' \text{ yr}^{-1})$	0.020	0.013	0.009	0.028	0.022	0.011
$\langle d \rangle (\text{kpc})$	2.49	4.26	6.55	1.83	2.39	5.27
$\langle V_{\text{tan}} \rangle (\text{km s}^{-1})$	241	269	267	242	250	266
$\langle \hat{t}_{\text{E}} \rangle (\text{d})$	38.3	45.0	54.7	42.6	50.0	75.6
$\langle \tau/\tau_0 \rangle$	0.558	0.695	0.163	0.839	0.628	0.488

Table 4.4: Summary of the results obtained for the simulation of microlenses towards the LMC for the EROS experiment for an age of the halo of 14 Gyr, different model initial mass functions, and several magnitude cuts.

50% (Camacho et al., 2007). Our simulations reproduce the results of the EROS experiment more effectively. The red-dwarf population is obviously responsible for this increase. When a non-standard initial mass function is adopted, the results show, however, only marginal differences with respect to those obtained for a white-dwarf population, given that in this case the role of red dwarfs is limited. In summary, our results are in fair agreement with those obtained by the EROS experiment, and appear to indicate that the microlensing optical depth, obtained by the MACHO collaboration, is an overestimate.

4.3.4 The dark matter density

Using the information presented in this chapter, we are able to assess the contribution of stellar populations, for the mass range studied, to the mass of the baryonic dark-matter halo. Based on their ~ 15 microlensing events, the MACHO collaboration derived an estimate of the halo fraction of dark matter f , as well as the MACHO mass m , using maximum-likelihood techniques. A similar analysis was completed by the EROS team, but with the significant difference that, in that case, no event was reported for the LMC, which implies that only an upper limit to the halo mass fraction can be obtained.

To compare the results of the MACHO and EROS collaborations with our Monte Carlo simulations, we adopted, as our reference model, the isothermal sphere of core radius 5 kpc, with a value of $\rho_0 = 0.0079 M_{\odot} \text{ pc}^{-3}$ for the local dark-matter density and disregarding the contribution of the LMC halo. Using this model, we obtained that the optical depth towards the LMC is $\tau_{\text{LMC}} = 5.1 \times 10^{-7} f$. The different estimates of the halo mass fraction f , as a function of mass, are plotted in Fig. 4.5. As a solid line we show the curve of the MACHO 95% confidence-level, as taken from Alcock et al. (2000), and the EROS 95% confidence-level upper-limit, based on no observed events in the EROS-1 and EROS-2 data (Tisserand et al., 2007). We

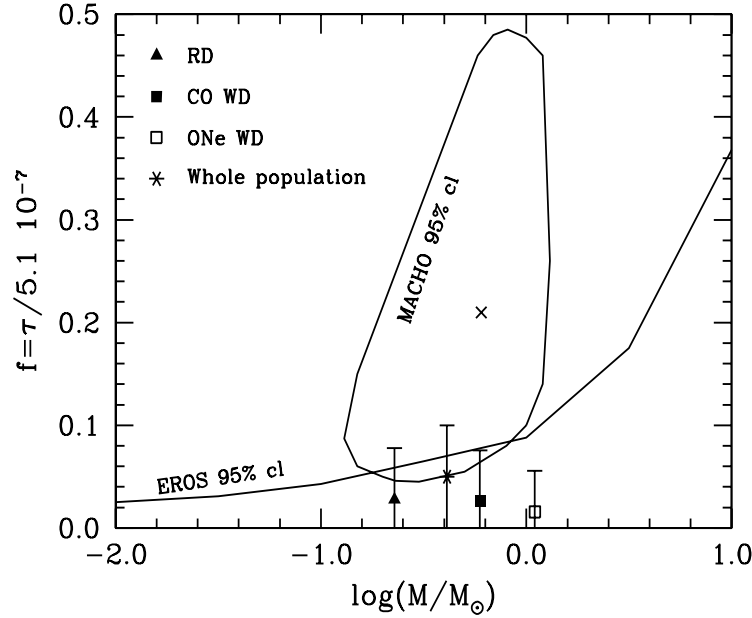


Figure 4.5: Halo dark matter fraction as a function of the mass lens. We plot using a solid line the 95% confidence-level curve for the MACHO experiment and the 95% confidence-level upper-limit for the EROS experiment.

also represent the individual contributions of each population studied and the entire population, in addition to the corresponding 95% confidence-level error bars. It is remarkable that the value obtained for the entire halo simulated-population agrees within the 95% confidence-level curves of both observational estimates.

Our results therefore predict that the range of stellar masses within 0.08 and $10 M_{\odot}$, provides $f = 0.05$ and an average mass of $0.411 M_{\odot}$ to the halo dark matter, in agreement with the observational data. This result corroborates our previous estimates of the limited contribution of both CO white dwarfs and ONe white dwarfs (García-Berro et al., 2004; Camacho et al., 2007).

4.4 Conclusions

We have extended previous studies of the contribution to the halo dark matter of the white-dwarf population and included the Galactic population of red dwarfs. We have estimated the contribution of these objects to the microlensing optical depth towards the LMC and compared our estimate with the measurements of the MACHO and EROS collaborations. Our estimate is based on a series of Monte Carlo simulations that incorporate the most up-to-date evolutionary tracks for red dwarfs, CO white

dwarfs, and ONe white dwarfs, and reliable models of our Galaxy and the LMC. In a first set of simulations, we have found that the contribution of the red-dwarf population practically doubles the contribution found so far for the white-dwarf population. Our results indicate that the entire population of these stars can account for at most ~ 0.3 of the optical depth found by the MACHO team. This value implies that the contribution of the full range of masses between 0.08 and $10 M_{\odot}$ represents 5% of the halo dark matter with an average mass of $0.4 M_{\odot}$. Although this result is in partial agreement with the 95% confidence level MACHO estimate for a standard isothermal sphere and no halo LMC contribution, the expected number of events obtained by our simulations (3 events at the 95% confidence level) is substantially below the 13 to 17 observed MACHO events. These arguments reinforce the idea, previously pointed out by other studies, that the optical depth found by the MACHO team should be an overestimate, probably due to contamination of self-lensing objects, variable stars and others. Moreover, we have assessed the compatibility between the observed event rate distribution and the ones obtained for the different populations under study. Our results show that the CO white-dwarf population can reproduce fairly well the observed event-rate distribution although, as mentioned earlier, the expected number of events is considerable smaller. On the other hand, the negative results obtained by the EROS team towards the LMC are in agreement with our standard halo simulation. Finally, and for the sake of completeness, we have studied the effects of a log-normal biased initial mass function. In this case, the contribution of the red-dwarf population is only marginal given that the production of low-mass stars is strongly inhibited. Accordingly, the total contribution to the microlensing optical depth is not different from that found in previous studies of the white-dwarf contribution.

Chapter 5

White dwarfs with hydrogen–deficient atmospheres and the dark matter content of the Galaxy

5.1 Introduction

In previous chapters we have exhaustively analyzed the contributions of the halo populations of carbon-oxygen (CO) and oxygen-neon (ONe) white dwarfs with pure hydrogen atmospheres. We have also extended our initial studies to include the population of halo red dwarfs. Thus, these studies covered so far the full range of initial masses able to produce microlensing events compatible with the required durations, and nearly 90% of the stellar content. The main conclusion of these studies is that the entire population of these stars can account at most for ~ 0.3 of the optical depth found by the MACHO team. This in turn implies that the contribution of the full range of masses between 0.08 and $10 M_{\odot}$ represents $\leq 5\%$ of the halo dark matter, with an average mass of $0.4 M_{\odot}$. Even though, we also found that the expected number of events obtained in our simulations (three events at the 95% confidence level) is substantially below the number of events detected by the MACHO team. Thus these results support the idea previously pointed out in several other studies, that the optical depth found by the MACHO team is probably an overestimate, possibly due to contamination of self-lensing objects, variable stars and others.

In all previous studies in which the contribution of white dwarfs to the dark matter content of the Galaxy was appraised, white-dwarf evolutionary sequences with pure hydrogen atmospheres (white dwarfs of the DA type) were employed, and the contribution of non-DA white dwarfs was disregarded. However, non-DA white

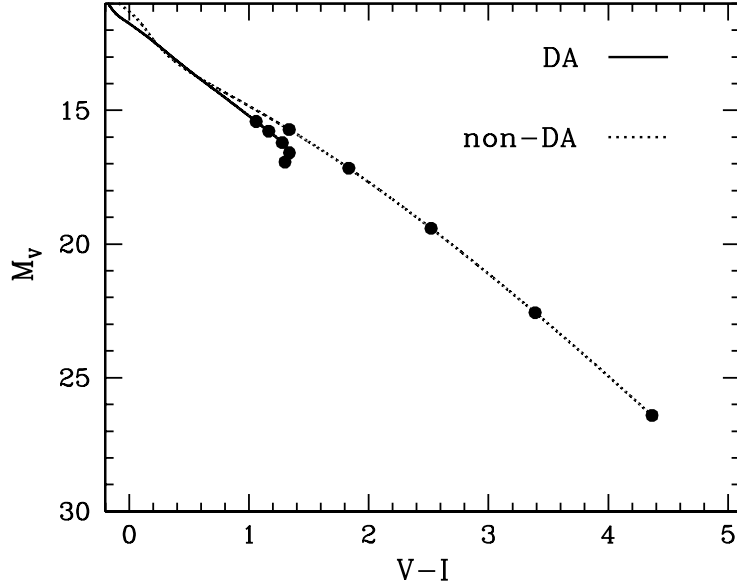


Figure 5.1: Color-magnitude diagram of a typical $0.6 M_{\odot}$ white dwarf. The solid line corresponds to a cooling sequence of a hydrogen-rich (DA) white dwarf (Salaris et al., 2000), while the dashed line corresponds to a helium-rich (non-DA) white dwarf (Benvenuto & Althaus, 1997). The dots correspond to cooling ages of 6, 8, 10, 12 and 14 Gyr.

dwarfs represent roughly 20% of the entire white dwarf population, and consequently their contribution cannot be considered negligible *a priori*. Moreover, there is strong observational evidence that non-DA white dwarfs represent an even more important fraction of the cool white dwarf population (Bergeron, Leggett & Ruiz, 2001), but the current simulations of the halo white dwarf population do not take this fact into account. Additionally, the colors and magnitudes of cool white dwarfs depend on their atmospheric composition — see Fig. 5.1. Indeed, it has been demonstrated (Hansen, 1998) that white dwarfs with hydrogen-rich atmospheres experience a blue turn at low luminosities, which is the result of extremely strong H_2 molecular absorption features in the infra-red. This blue hook prevents DA white dwarfs from reaching very faint magnitudes. On the contrary, white dwarfs of the non-DA types cool like black bodies and hence may easily reach the faintest magnitudes within the age of the Galaxy. Again, this important fact has been overlooked in the most up-to-date models of the population of halo white dwarfs. Finally, the rate of cooling is controlled by the thickness and composition of the atmospheric layers. It turns out that non-DA white dwarfs cool faster than their corresponding DA counterparts, another fact that has not been taken into account in previous simulations.

Another controversial issue which deserves attention is whether the lenses belong to the halo or to an extended thick disk population (Reid et al., 2001; Torres et al., 2002). After all, and as pointed out by Gyuk & Gates (1999), the thick disk population presents a reasonable alternative to a halo population of lenses. Several observational (Oppenheimer et al., 2001; Kilic et al., 2006; Harris et al., 2006; Vidrih et al., 2007) works have addressed this question, and a definitive answer still requires more theoretical and observational efforts.

In this chapter we extend our Monte Carlo simulator to include the contribution of non-DA halo white dwarfs to the microlensing event rate, and we study as well the role played by the thick-disk populations of these stars. Special emphasis has been put on the analysis of the simulated microlensing events as a function of the range of colors susceptible to be detected by the EROS and MACHOS surveys, as well as on comparing our results with such surveys. For this purpose not only do we incorporate up-to-date evolutionary sequences of hydrogen-deficient atmospheres, but also two distinct thick disk models.

The chapter is organized as follows. In Section 5.2 we summarize the main ingredients of our Monte Carlo code and other basic assumptions and procedures. Section 5.3 is devoted to the discussion of our main findings, such as the contribution of red dwarfs and DA and non-DA white dwarfs to the microlensing optical depth towards the LMC following both MACHOS and EROS experiment, the probability that a microlensing event may be assigned either to the thick disk or the halo, and the contribution of the entire population of red and white dwarfs of whatever type to the baryonic content of the Galaxy.

5.2 Building the model

We expanded our Monte Carlo simulator to include the population of non-DA white dwarfs. Specifically, for those stars which have had time enough to enter into the white dwarf cooling track and given a set of theoretical cooling sequences and the initial to final mass relationship (Iben & Laughlin, 1989) their luminosities, effective temperatures and colors were obtained. The cooling sequences adopted here depend on the mass of the white dwarf. White dwarfs with masses smaller than $M_{\text{WD}} = 1.1 M_{\odot}$ are expected to have CO cores and, consequently, we adopt for them the cooling tracks of Salaris et al. (2000) if they belong to the DA spectral class. If, on the contrary, the white dwarf has a hydrogen-deficient atmosphere we use the cooling sequences of Benvenuto & Althaus (1997) — corresponding to pure helium atmospheres — and the bolometric corrections of Bergeron et al. (1995). These are our fiducial cooling sequences. However, to study the effects of different cooling sequences for hydrogen-deficient white dwarfs (and, hence, different cooling speeds) which may affect our results we also use the cooling sequences of Bergeron et al. (1995) — see below. White dwarfs with masses larger than $M_{\text{WD}} = 1.1 M_{\odot}$ most

	Model A	Model B	Model C
below 4000 K	20%	100%	100%
4000 K — 5000 K	20%	64.5%	64.5%
5000 K — 6000 K	20%	0%	0%
> 6000 K	20%	16.5%	16.5%
Non-DA cooling tracks	Benvenuto et al. (1997)	Benvenuto et al. (1997)	Bergeron et al. (1995)

Table 5.1: Percentages of non-DA white dwarfs and its corresponding cooling tracks for the different simulated models.

probably have ONe cores, and for these white dwarfs we adopt the cooling sequences of Althaus et al. (2007). All these cooling sequences incorporate the most accurate physical inputs for the stellar interior (including neutrinos, crystallization, phase separation and Debye cooling) and, for the case of DA white dwarfs, reproduce the blue turn at low luminosities (Hansen, 1998).

5.2.1 The fraction of DA and non-DA white dwarfs

To assign a spectral type to each of the white dwarfs in the simulated sample we proceeded as follows. In a first set of simulations we adopted the canonical fraction of 80% of white dwarfs of the spectral type DA and 20% of the non-DA class, independently of the effective temperature of the white dwarf. We regard this as our fiducial model, and we refer to it as model A. However, several observations indicate that this ratio is a function of the effective temperature. For instance, the well-known DB-gap, where no white dwarfs of the DB spectral class can be found, occurs at effective temperatures between 45 000 K and 30 000 K. Additionally, Bergeron et al. (2001) found that most white dwarfs with effective temperatures ranging from 6 000 K to 5 000 K are DAs. Finally, Bergeron & Leggett (2002) argued that all white dwarfs cooler than 4 000 K have mixed H/He atmospheres.

Many of these early findings have been corroborated by the wealth of data obtained from recent large surveys, like the Sloan Digital Sky-Survey (Harris et al., 2006; Kilic et al., 2006). Accordingly, we have produced a second set of simulations, and we refer to them as model B, following these observational results. Basically, in model B we adopt the same fraction of DA white dwarfs (80%) for temperatures above 6 000 K. All white dwarfs in the range of effective temperatures between 6 000 K and 5 000 K were considered to be DA white dwarfs. Finally, for effective temperatures below this value we adopt a fraction of 50% (Bergeron & Leggett, 2002; Gates et al., 2004).

We would like to note that we model the transitions between the different spectral

	Canonical thick disk	Metal-weak thick disk
Initial mass function	Standard	Standard
Density profile	Double exponential	Double exponential
Scale height (kpc)	1.5	1.36
Scale length (kpc)	3	2
Star formation rate	Exponential decay	Exponential decay
Age (Gyr)	12	12
Peak (Gyr)	10	10
$(\sigma_U, \sigma_V, \sigma_W)$ (km s ⁻¹)	(60, 45, 35)	(59, 40, 44)
V_ϕ (km s ⁻¹)	-40	-40
$\Delta\langle V_\phi \rangle / \Delta z $ (km s ⁻¹ kpc ⁻¹)	0	-36
Normalization criteria	8.5% of the local thin disk density	8.5% of the local thin disk density

Table 5.2: Summary of the global properties of the canonical thick disk and metal-weak thick disk models.

classes in a purely heuristic way because currently there are no cooling sequences which correctly reproduce these transitions, as this is a long-standing problem, which is indicative of a failure of the theoretical cooling models. However, our model correctly reproduces the observations, and thus we consider it to be a fair approach. Finally, to check the sensitivity of our results to the adopted cooling tracks we have also computed a third set of simulations, based on model B, in which we use the cooling sequences of Bergeron et al. (1995). We refer to this model as model C. The principal characteristics of all these models are summarized in Table 5.1.

5.2.2 The thick disk model

The structure and kinematics of the Galactic disk remain a source of controversy and discussion. In particular the nature of the thick disk is an active field of research. Consequently we have used two distinct models in our simulations. The first of these is a canonical thick disk model, which we consider as a starting reference model. However, there are alternative thick disk models based on the kinematics of metal-poor stars of the Galaxy — see Chiba & Beers (2000) and references therein — that challenge the canonical model. Accordingly, we also consider the most recent thick disk model of Carollo et al. (2010), which is based on the SDSS Data Release 7. We describe them separately, while a summary of both the canonical thick disk model and the metal-weak thick disk is given in Table 5.2.

The kinematical properties of the canonical model are well represented by an ellipsoid with constant values of the velocity and dispersions and an asymmetrical

drift. Within this model the spatial distribution is generally assumed to follow exponential laws characterized by a scale height and a scale length with no vertical gradients. Thus we have chosen a double exponential law for the density profile of this model with a scale height of 1.5 kpc and a scale length of 3.0 kpc (Reid, 2005). The kinematical properties of the synthetic thick disk stars have been modeled according to an ellipsoid with the standard dispersion $(\sigma_U, \sigma_V, \sigma_W) = (60, 45, 35) \text{ km s}^{-1}$ and an asymmetric velocity drift $V_\phi = -40 \text{ km s}^{-1}$ (Reid, 2005).

In a recent study, Carollo et al. (2010) analyzed the structure and kinematical properties of the Milky Way based on the Sloan Digital Sky Survey Data Release 7 and showed evidence that a sizeable fraction of the thick disk is composed by metal-weak stars with independent kinematical properties. Following Carollo et al. (2010) we use an ellipsoid with standard dispersions $(\sigma_U, \sigma_V, \sigma_W) = (59, 40, 44) \text{ km s}^{-1}$, and a scale height and a scale length of 1.36 and 2.0 kpc, respectively. The most distinctive feature of the model of Carollo et al. (2010) is that the asymmetric drift varies as a function of height above the Galactic plane. Specifically, the gradient in the asymmetric drift is $\Delta\langle V_\phi \rangle / \Delta|z| = -36 \text{ km s}^{-1} \text{ kpc}^{-1}$, which agrees with the previous studies of Chiba & Beers (2000). We note that although the observations indicate that only a fraction of the thick disk could be explained by the metal-weak thick disk population, we have considered a full metal-weak thick disk to obtain an upper limit to the possible contribution of this population to the microlensing experiments.

Additionally, in both cases we took into account the peculiar velocity of the Sun $(U_\odot, V_\odot, W_\odot) = (10.0, 15.0, 8.0) \text{ km s}^{-1}$ (Dehnen & Binney, 1998) and discarded those stars that escape the potential of the Galaxy. We also assumed that the thick disk formation started 12 Gyr ago with a maximum star formation rate occurring 10 Gyr ago and exponentially decreased since, following the model of Gilmore, Wyse & Jones (1995). Finally our thick disk models have been normalized assuming that the thick disk density represents 8.5% of the thin disk density (Reid, 2005).

5.3 Results and discussion

5.3.1 The optical depth towards the LMC

In this section we examine carefully the contribution of halo non-DA white dwarfs to the optical depth, which provides the most immediate and simple information about the microlensing experiments. Thus we compare our simulations with the optical depth derived by the MACHO collaboration. In Fig. 5.2 we show the contribution to the optical depth of the different populations under study as a function of the adopted magnitude cut, in the same manner as it was done in García-Berro et al. (2004) and subsequent papers. Our simulations have been normalized to the value derived by Alcock et al. (2000), $\tau_0 = 1.2 \times 10^{-7}$. The contributions to the microlensing optical depth of the different populations are represented by solid and open squares for the

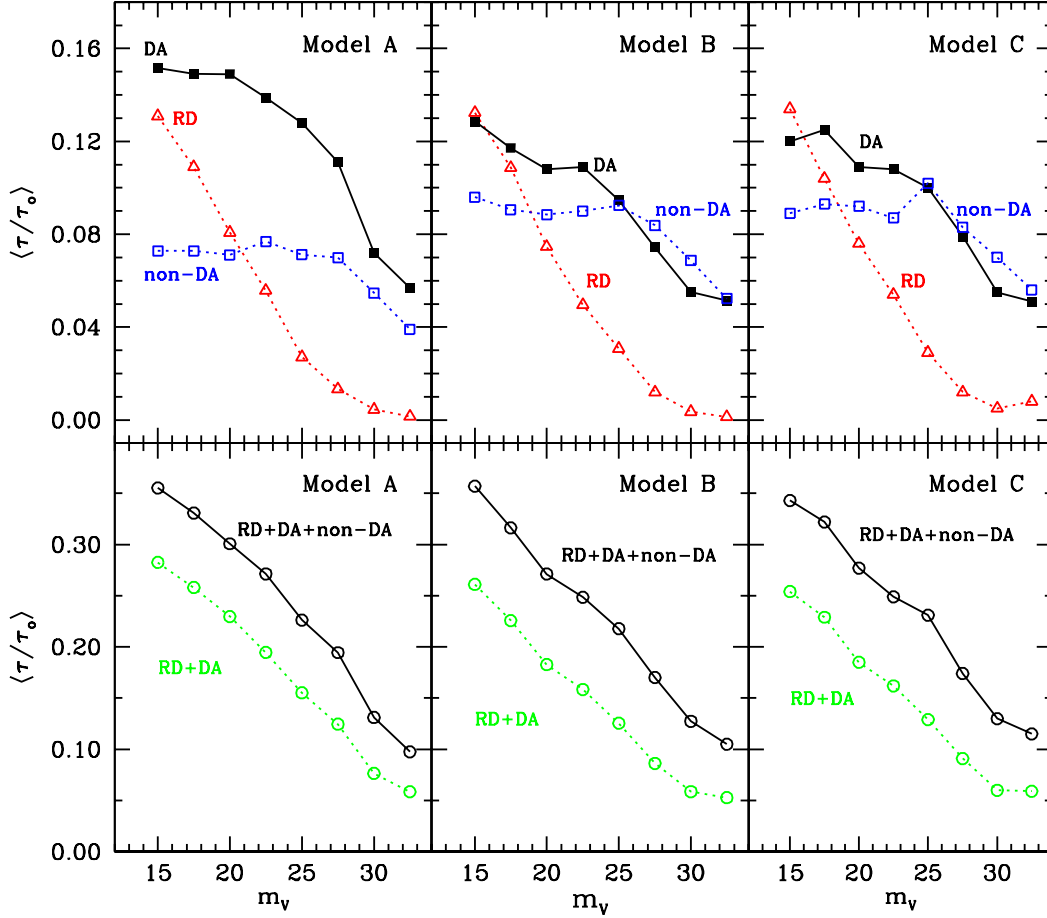


Figure 5.2: Microlensing optical depth towards the LMC as a function of the limiting magnitude. Solid and open squares represent the DA and non-DA white dwarf populations, respectively. Red dwarfs are represented by open triangles, while the entire population is shown by open circles.

populations of DA and non-DA white dwarfs respectively, while the contribution of the red dwarf population is displayed by open triangles. Finally, the contribution to the microlensing optical depth of the entire population is shown by open circles. For the sake of clarity, the contribution of the ONe white dwarf population is not shown in the top panels of Fig. 5.2, but it is taken into account when the total contribution (shown in the bottom panels of Fig. 5.2) is computed. As can be seen, for model A at bright magnitude cuts the contribution to the microlensing optical depth is roughly 7% for the population of non-DA white dwarfs and $\sim 15\%$ for the DA white dwarf population (see the top left panel of Fig. 5.2). However, it is remarkable that

as the magnitude cut increases, the contribution of non-DA white dwarfs remains almost constant, while the contribution of DA white dwarfs rapidly drops. This is a direct consequence of the faster cooling rate of non-DA white dwarfs and of the fact that non-DA white dwarfs do not experience the blue turn. The contribution of the red dwarf population is very similar to the one found in our previous studies, with a fairly constant decreasing slope as the magnitude cut increases. The decreasing contribution of red dwarfs to the microlensing optical depth for increasing magnitude cuts stems from the fact that in general red dwarfs are brighter than regular white dwarfs.

When model B is considered, the overall contribution of DA white dwarfs is smaller than the contribution of non-DA white dwarfs — see the top central panel of Fig. 5.2. Note that for model A the opposite occurs, that is, the contribution of DA white dwarfs is more sizeable than the one of non-DA white dwarfs. The reason for this is easy to understand. Since the luminosity function of halo white dwarfs of Torres et al. (1998) only provides the density of relatively bright DA white dwarfs ($\log(L/L_\odot) \geq -3.7$) and the fraction of low luminosity white dwarfs in model B is only 50% (in contrast with that of model A, for which a fraction of 80% was adopted independently of the effective temperature), the contribution of low luminosity white dwarfs to the optical depth decreases.

Finally, the top right panel of Fig. 5.2 shows the relative contributions to the microlensing optical depth when model C is considered. As can be seen, the results are virtually indistinguishable of those obtained for model B, as one should expect given that the cooling tracks of Bergeron et al. (1995) are very similar to those of Benvenuto & Althaus (1997). In all cases it is important to highlight that as far as the entire population is concerned, there is a noticeable increase in the contribution to the optical depth, which is exclusively due to the inclusion of non-DA white dwarfs in our calculations. Moreover, the global contribution of white dwarfs to the microlensing optical depth is very similar in both models — see the bottom panels of Fig. 5.2 — for magnitude cuts larger than $m_V \sim 23^{\text{mag}}$, which is a reasonable value for current surveys. This value, roughly 30% of the observed optical depth obtained by the MACHO team, represents a 50% increment with respect to the value found in our previous studies, see Torres et al. (2008).

A more precise information can be obtained from our simulations. A summary is presented in Table 5.3, where we show several interesting parameters for the three models under study as a function of the adopted magnitude cut. In particular we show in this table the expected number of white dwarf microlensing events, the number of microlensing events produced by red dwarfs, the average mass of the microlenses for both the microlensing events produced by white and red dwarfs, the fraction of the white dwarf microlensing events produced by white dwarfs of the non-DA spectral type (η) over the total white dwarf microlensing events, the average proper motion, distance and tangential velocity of the lenses, the corresponding Einstein crossing times of the microlenses and finally the relative contribution to

	Model A				Model B				Model C			
Magnitude	17.5	22.5	27.5	32.5	17.5	22.5	27.5	32.5	17.5	22.5	27.5	32.5
$\langle N_{\text{WD}} \rangle$	0 ± 1	0 ± 1	0 ± 1	0 ± 1	0 ± 1	0 ± 1	0 ± 1	0 ± 1	0 ± 1	0 ± 1	0 ± 1	0 ± 1
$\langle N_{\text{RD}} \rangle$	0 ± 1	0 ± 1	0 ± 1	0 ± 1	0 ± 1	0 ± 1	0 ± 1	0 ± 1	0 ± 1	0 ± 1	0 ± 1	0 ± 1
$\langle m_{\text{WD}} \rangle (M/M_{\odot})$	0.599	0.605	0.627	0.721	0.604	0.602	0.627	0.661	0.600	0.605	0.619	0.678
$\langle m_{\text{RD}} \rangle (M/M_{\odot})$	0.325	0.233	0.109	0.081	0.319	0.227	0.118	0.080	0.315	0.227	0.124	0.079
$\langle \eta \rangle$	0.204	0.227	0.323	0.837	0.810	0.834	0.927	0.993	0.780	0.828	0.913	0.987
$\langle \mu \rangle ('' \text{ yr}^{-1})$	0.020	0.014	0.010	0.009	0.021	0.016	0.015	0.014	0.021	0.014	0.012	0.016
$\langle d \rangle (\text{kpc})$	2.54	3.62	5.28	5.26	2.29	3.28	3.49	3.88	2.37	3.71	4.09	3.02
$\langle V_{\text{tan}} \rangle (\text{km s}^{-1})$	243	247	253	244	239	244	252	260	239	252	241	238
$\langle \hat{t}_{\text{E}} \rangle (\text{d})$	41.3	49.6	59.0	60.7	39.1	45.3	47.7	60.9	40.1	45.6	52.1	65.5
$\langle \tau / \tau_0 \rangle$	0.331	0.271	0.194	0.098	0.316	0.257	0.179	0.109	0.321	0.266	0.174	0.115

Table 5.3: Summary of the results obtained for the entire population of microlenses towards the LMC for several magnitude cuts when the results of the MACHO collaboration are simulated. An age of the halo of 14 Gyr has been adopted.

the microlensing optical depth. A close inspection of Table 5.3 reveals that all three models produce similar results except in one aspect, the fraction of microlensing events attributable to a non-DA white dwarf. As can be seen, the expected number of microlensing events is very small in all models, since in all cases no more than one microlensing event is expected to be found at the 1σ confidence level. Additionally, the average masses of the microlenses are around $0.6 M_{\odot}$ in the case of white dwarfs, while for red dwarfs it is $\sim 0.2 M_{\odot}$, the average distances to the microlenses are also very similar for both models, and there are no significant differences in the Einstein crossing times.

The only relevant difference between the simulations is the spectral type of the white dwarf responsible for the simulated microlensing events. Whereas for model A the DA type prevails in $\sim 73\%$ of the cases, for model B this fraction drops to $\sim 20\%$ of the cases, while for model C we obtain a very similar value, $\sim 21\%$. This can be understood by the same reasoning employed before. For models B and C, at low effective temperatures the fraction of hydrogen-rich white dwarfs is considerably smaller than for model A and, additionally, old DA white dwarfs are brighter than non-DAs. Thus for models B and C non-DA white dwarfs dominate at low luminosities and produce most of the microlensing events.

Additionally, from a detailed analysis of the data used to build Table 5.3, we have found that on average the microlenses produced by non-DA white dwarfs have slightly higher average masses ($\sim 0.61 M_{\odot}$ and $\sim 0.56 M_{\odot}$, respectively) and can be found at smaller distances (~ 1.7 kpc and ~ 2.9 kpc, respectively) than those produced by the population of DA white dwarfs. That is again a consequence of the different cooling rates and colors of non-DA white dwarfs. As previously mentioned, non-DA white dwarfs cool faster and moreover, as they cool, they become substantially dimmer than their corresponding DA counterparts. Hence, not only can the population of non-DA white dwarfs produce microlenses at significantly smaller distances, but these values do not depend significantly on the model adopted for the evolution of the atmospheric composition of white dwarfs. Since the distribution of velocities does not depend on the spectral type, the final result is that the Einstein crossing times are on average different for the microlensing events produced by non-DA and DA white dwarfs (~ 40 and ~ 57 days, respectively).

5.3.2 The EROS experiment

The EROS experiment has monitored a wider solid angle and less crowded fields in the LMC than the MACHO team. In addition, it has also monitored the SMC. For these reasons, self-lensing of the LMC should be less important in the EROS experiment than in the case of the MACHO collaboration. Consequently, a smaller value of the optical depth should be expected, and this is indeed the case. The EROS results, adopting a standard halo model and assuming $\tau_{\text{SMC}} = 1.4\tau_{\text{LMC}}$ indicate that the microlensing optical depth is $\tau_0 = 0.36 \times 10^{-7}$ (Tisserand et al., 2007), which is four

	Model A				Model B				Model C			
Magnitude	17.5	22.5	27.5	32.5	17.5	22.5	27.5	32.5	17.5	22.5	27.5	32.5
$\langle N_{\text{WD}} \rangle$	0 ± 1	0 ± 1	0 ± 1	0 ± 1	0 ± 1	0 ± 1	0 ± 1	0 ± 1	0 ± 1	0 ± 1	0 ± 1	0 ± 1
$\langle N_{\text{RD}} \rangle$	0 ± 1	0 ± 1	0 ± 1	0 ± 1	0 ± 1	0 ± 1	0 ± 1	0 ± 1	0 ± 1	0 ± 1	0 ± 1	0 ± 1
$\langle m_{\text{WD}} \rangle (M/M_{\odot})$	0.383	0.601	0.618	0.744	0.602	0.598	0.621	0.674	0.590	0.605	0.610	0.666
$\langle m_{\text{RD}} \rangle (M/M_{\odot})$	0.328	0.206	0.111	0.083	0.305	0.208	0.118	0.082	0.304	0.177	0.112	0.085
$\langle \eta \rangle$	0.186	0.246	0.373	0.671	0.774	0.800	0.919	0.965	0.711	0.882	0.957	0.976
$\langle \mu \rangle ('' \text{ yr}^{-1})$	0.021	0.017	0.009	0.006	0.022	0.016	0.016	0.015	0.021	0.017	0.011	0.016
$\langle d \rangle (\text{kpc})$	2.51	3.16	5.52	9.04	2.46	3.35	3.58	3.80	2.56	3.23	4.83	3.21
$\langle V_{\text{tan}} \rangle (\text{km s}^{-1})$	250	258	244	245	254	259	272	275	261	257	259	245
$\langle \hat{t}_{\text{E}} \rangle (\text{d})$	41.9	44.1	60.7	88.8	35.9	40.9	43.5	53.2	38.1	39.6	49.4	63.9
$\langle \tau / \tau_0 \rangle$	0.977	0.810	0.659	0.384	0.794	0.678	0.400	0.214	0.775	0.618	0.352	0.259

Table 5.4: Summary of the results obtained for the entire population of microlenses towards the LMC for the EROS experiment, using models A, B and C and adopting an age of the halo of 14 Gyr and several magnitude cuts.

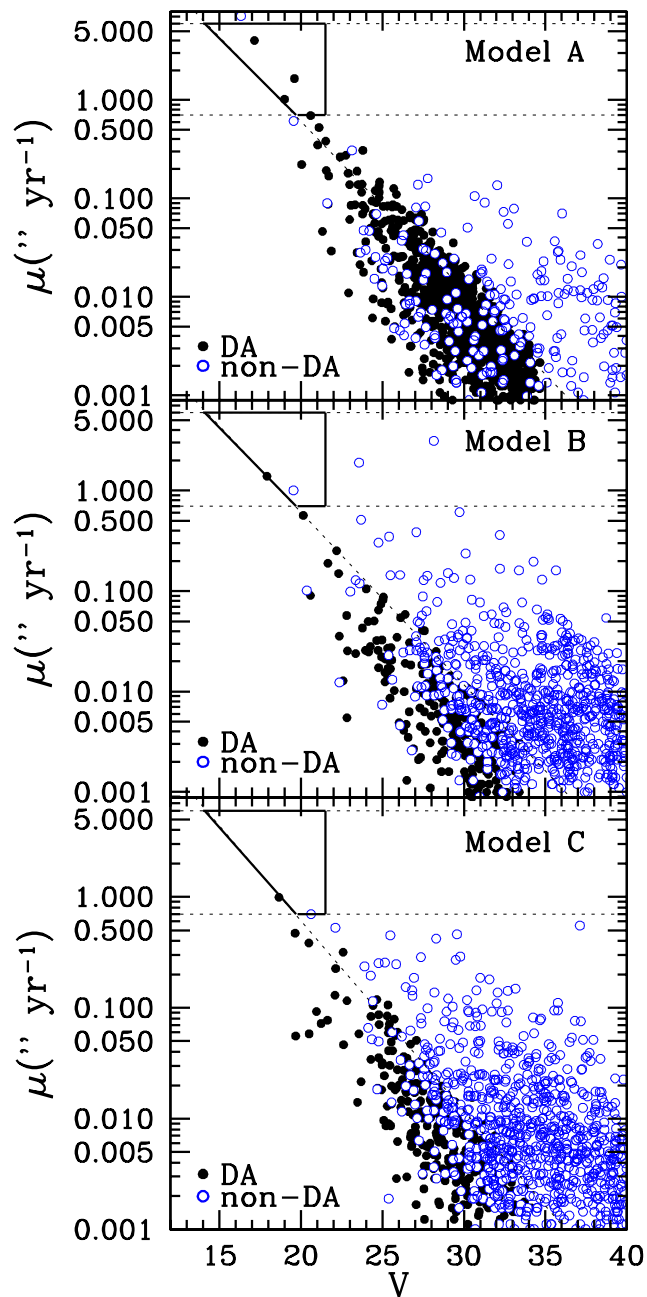


Figure 5.3: Proper motion as a function of the V magnitude for the halo white dwarf population. The EROS selection zone is shown as a bold solid line.

times smaller than that obtained by the MACHO team.

We have performed a set of simulations emulating the conditions of the EROS

experiment using the same populations described previously. Although only small differences should be expected, this new series of simulations represents a test of the robustness of our numerical procedures. In Table 5.4 we summarize the results obtained for this set of simulations. Our simulations show that independently of the adopted model for the spectral type of white dwarfs, the joint population of red dwarfs and white dwarfs of the galactic halo provides at most $\sim 90\%$ of the optical depth estimated by the EROS team. This value represents an increase of $\sim 20\%$ with respect to the one obtained in our previous simulations (Torres et al., 2008). Obviously, the non-DA white dwarf population is responsible for this result, and this confirms our previous conclusion that there is a general agreement between the theoretical models and the results of the EROS team.

Moreover the EROS experiment used a set of selection criteria in the search of halo white dwarfs to distinguish halo objects from thick disk stars (Goldman et al., 2002). For those stars detectable by EROS, namely those with magnitudes brighter than $V = 21.5$ and $I = 20.5$, the selection criteria are implemented by two cuts. The first one uses the reduced proper motion and requires that the reduced proper motion of a halo object should be $H_V > 22.5$. The second cut is applied to the resulting sample and only selects those stars with large proper motions, $\mu > 0.8'' \text{yr}^{-1}$. In Fig. 5.3 we present a typical simulation of the halo white dwarf population adapted to the requirements of the EROS team. The previously mentioned criteria are displayed by dotted lines, while the resulting halo selection zone is represented by a bold solid line. For model A we obtain that at the 1σ confidence level, 4 ± 2 DA white dwarfs and 1 ± 1 non-DA white dwarfs should be found in the selection zone, while for model B we obtain 1 ± 1 and 1 ± 1 white dwarfs, respectively, and the same occurs for model C. These results indicate that the models which take into account the temperature dependence of the white dwarf spectral type (models B and C) seem to yield a more realistic and consistent estimate, given that it agrees well with the null results of the EROS team. It is also worth noting that the applied selection criteria, in particular the proper motion cut ($\mu > 0.8'' \text{yr}^{-1}$), are so restrictive that only a small (1%) fraction of the halo white dwarf population can be found in the selection zone.

5.3.3 The thick disk contribution

As already mentioned, the thick disk is characterized by higher velocity distributions and a larger scale height than those of the thin disk. Several studies on halo white dwarfs have considered the thick disk population as a possible source of contamination (Oppenheimer et al., 2001; Reid et al., 2001; Torres et al., 2002), but a comprehensive theoretical study remains to be done. Accordingly we evaluate in this section the joint contribution of thick disk white dwarfs and red dwarfs to the microlensing optical depth. We do that for both the MACHO and EROS experiments in the same way as for the halo simulations presented in the previous section. The

Magnitude	Canonical thick disk				Metal-weak thick disk			
	17.5	22.5	27.5	30.0	17.5	22.5	27.5	30.0
$\langle N_{\text{WD}} \rangle$	0 ± 1	0 ± 1	0 ± 1	0 ± 1	0 ± 1	0 ± 1	0 ± 1	0 ± 1
$\langle N_{\text{RD}} \rangle$	0 ± 1	0 ± 1	0 ± 1	0 ± 1	0 ± 1	0 ± 1	0 ± 1	0 ± 1
$\langle m_{\text{WD}} \rangle (M/M_{\odot})$	0.616	0.615	0.588	0.593	0.617	0.613	0.650	0.709
$\langle m_{\text{RD}} \rangle (M/M_{\odot})$	0.371	0.221	0.111	0.085	0.384	0.269	0.091	0.079
$\langle \eta \rangle$	0.348	0.348	0.443	0.999	0.431	0.452	0.947	0.999
$\langle \mu \rangle ('' \text{ yr}^{-1})$	0.005	0.004	0.003	0.002	0.009	0.008	0.007	0.001
$\langle d \rangle (\text{kpc})$	3.42	4.07	5.11	5.17	1.75	2.04	2.29	1.39
$\langle V_{\text{tan}} \rangle (\text{km s}^{-1})$	82	84	78	82	79	84	77	69
$\langle \hat{t}_{\text{E}} \rangle (\text{d})$	156	173	204	186	125	122	136	121
$\langle \tau/\tau_0 \rangle$	0.462	0.274	0.137	0.012	0.257	0.203	0.050	0.020

Table 5.5: Summary of the results obtained for the thick disk population of microlenses towards the LMC for the MACHO experiment with a thick disk age of 12 Gyr and several magnitude cuts.

model of spectral evolution of white dwarfs adopted for this study is our model B, which we consider to be the most realistic one. Before starting the discussion of our results, we would like to emphasize that the calculation of the microlensing optical depth involves the addition of individual contributions, which are proportional to the Einstein crossing time corrected by the efficiency function — see Eq. 2.4. The efficiency function in turn depends on the crossing time, which is directly proportional to the Einstein radius and inversely proportional to the velocity perpendicular to the observer. For a thick disk object the average distance is smaller than that of a typical halo object. Thus there are two competing effects, smaller distances clearly imply smaller individual contributions to the optical depth. However, thick disk stars have also lower velocities than those of the halo, thus implying more important individual contributions. The precise balance between these two effects determines the final contribution.

The results of these simulations are shown in Fig. 5.4 and Table 5.5. In the top panels of Fig. 5.4 we show the contribution of the different populations under study to the optical depth derived by the MACHO experiment for both the canonical thick disk — left panels — and the metal-weak thick disk of Carollo et al. (2010) — right panels. It is interesting to realize that in both cases DA and non-DA white dwarfs contribute by roughly the same amount. Additionally, the contribution of red dwarfs quickly decreases and becomes almost negligible for realistic magnitude cuts, while that of white dwarfs decreases only slightly. Consequently, for realistic magnitude cuts — say $m_V > 20^{\text{mag}}$ — the contributions to the microlensing optical depth of both DA and non-DA white dwarfs are much more significant than that of red dwarfs. In the bottom panels of Fig. 5.4 we show the contribution of the

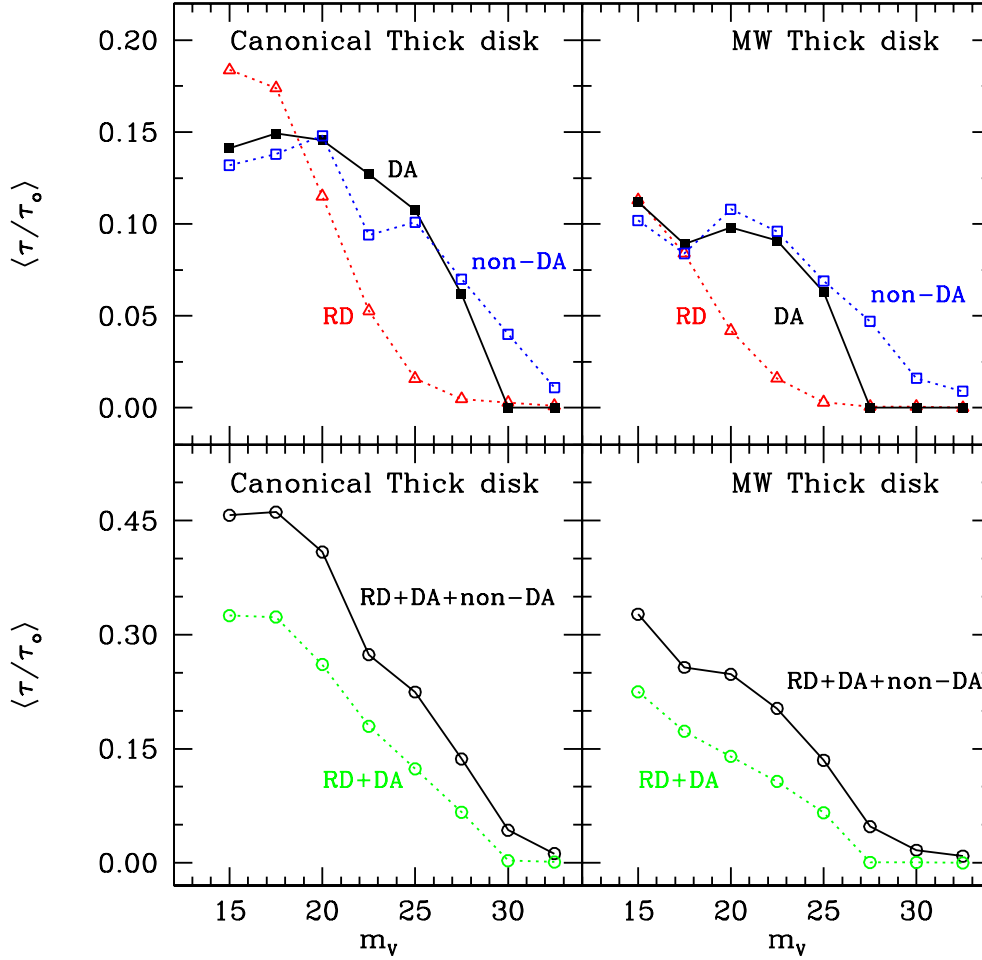


Figure 5.4: Microlensing optical depth towards the LMC as a function of the limiting magnitude for the thick disk population. Solid and open squares represent the DA and non-DA white dwarf populations, respectively. Red dwarfs are represented by open triangles, while the entire population is shown by open circles.

entire population to the microlensing optical depth for both thick disk models. We obtain that in the case of the MACHO experiment and for a typical magnitude cut of 22.5^{mag} the contribution of the populations of the canonical thick disk white dwarfs and red dwarfs to the optical depth can be as large as 30%, which is slightly more than that of the metal-weak thick disk model, which is on the order of 20%. At first glance, this result may seem to be in contrast with other recent estimates. For instance, Alcock et al. (2000) estimated the contribution of thick disk stars to be $\sim 2\%$ of the observed optical depth. This agrees with our model if we only consider the red dwarf population, for which we obtain a contribution to the optical depth of

Magnitude	Canonical thick disk				Metal-weak thick disk			
	17.5	22.5	27.5	30.0	17.5	22.5	27.5	30.0
$\langle N_{\text{WD}} \rangle$	0 ± 1	0 ± 1	0 ± 1	0 ± 1	0 ± 1	0 ± 1	0 ± 1	0 ± 1
$\langle N_{\text{RD}} \rangle$	0 ± 1	0 ± 1	0 ± 1	0 ± 1	0 ± 1	0 ± 1	0 ± 1	0 ± 1
$\langle m_{\text{WD}} \rangle (M/M_{\odot})$	0.629	0.636	0.651	0.746	0.584	0.595	0.619	0.604
$\langle m_{\text{RD}} \rangle (M/M_{\odot})$	0.200	0.221	0.106	0.080	0.325	0.177	0.085	0.076
$\langle \eta \rangle$	0.297	0.425	0.667	0.999	0.394	0.438	0.667	0.999
$\langle \mu \rangle ('' \text{ yr}^{-1})$	0.005	0.004	0.004	0.006	0.010	0.009	0.007	0.008
$\langle d \rangle (\text{kpc})$	3.37	4.08	4.41	3.73	1.68	1.95	2.55	2.09
$\langle V_{\text{tan}} \rangle (\text{km s}^{-1})$	87	88	94	98	83	85	86	77
$\langle t_{\text{E}} \rangle (\text{d})$	137	141	149	140	110	112	141	110
$\langle \tau/\tau_0 \rangle$	1.360	1.214	0.529	0.083	1.224	0.546	0.308	0.015

Table 5.6: Same as table 3 for the EROS experiment.

$\sim 3\%$, a value very similar to that obtained by Alcock et al. (2000). On the contrary, when thick disk white dwarfs are taken into account, the contribution of the thick disk is as large as that of the halo.

A more detailed analysis of the thick disk population can be done and reveals that in the case of the canonical thick disk the possible microlensing events have an Einstein crossing time $t_{\text{E}} \approx 170$ days for a magnitude cut of 22.5^{mag} , while for the case of the metal-weak thick disk the average Einstein crossing time amounts to $t_{\text{E}} \approx 120$ days. Both values are considerably higher than that of the halo population. Moreover, as can be seen in Table 5.5, the mean average tangential velocity is $\sim 80 \text{ km s}^{-1}$ for both models — which is what we would expect for a thick disk population, but the mean average distance of the lenses is $\sim 4 \text{ kpc}$ — which is comparable to that obtained for the halo population. This can be easily understood in terms of the selection criteria we use to decide when a star can be considered responsible of a microlensing event. In particular, we only consider as reliable microlensing events those in which the lens is dimmer than a certain magnitude cut and, given that the thick population is intrinsically brighter than the halo population, we only select those thick disk lenses which are far enough away. In any case, as can be seen in Table 5.5, our simulations show that the thick disk populations can produce at most one microlensing event. We emphasize that the results obtained using the canonical thick disk model appear to provide an upper limit for the contribution to the total microlensing optical depth — see Fig. 5.4.

We have also estimated the contribution to the optical depth of the thick disk populations in the case of the EROS experiment. The results are shown in Table 5.6. For a realistic magnitude cut of 22.5^{mag} , 1 ± 1 microlensing event is expected at a 1σ confidence level. The confirmation of this microlensing event would increase the value of the optical depth measured by the EROS team by $\sim 40\%$. However, we

point out that given the poor statistics, the number of microlensing events obtained in our simulations agrees reasonably well with the observations of the EROS team, who found none.

5.3.4 The event rate distribution

Besides the optical depth and the Einstein crossing time, a third quantity was proposed by Paczynski (1986) as relevant for the study of the microlensing experiments. This quantity is the microlensing event rate Γ , which provides the rate at which the lenses enter the microlensing tube. While the optical depth does not depend on the mass function, the event rate does, and consequently useful information about the different populations responsible for the microlensing events can be obtained by studying it.

In Fig. 5.5 we display with solid lines the normalized distributions of the microlensing event rate as a function of the event duration for the different populations of the canonical thick disk (left panels), the metal-weak thick disk (central panels) and the halo (right panels). We also show the results obtained by the MACHO team with a dashed line. The top panels show the distribution obtained for the population of red dwarfs, while the middle and the bottom panels show the distributions obtained for the populations of DA and non-DA white dwarfs respectively. To produce these distributions we have adopted a magnitude cut of 22.5^{mag} , which can be considered as representative of the current experiments. Although for this magnitude cut the contribution to the microlensing optical depth is approximately the same for the canonical thick disk (27.4%) and the halo populations (24.9%) and somewhat smaller for the metal-weak thick disk (20.3%), the event rate distributions are significantly different. We obtain for instance for the canonical thick disk population in all the cases very extended distributions with no clear maxima (except for the population of red dwarfs, which peaks at 70 days), while for the metal-weak thick disk population of red dwarfs a deficit of stars with long Einstein crossing times is found. Finally, for the halo populations the theoretical distributions of the microlensing event rate have clear maxima and moderate dispersions. Still, all the distributions are only marginally consistent with the observational distribution, which is characterized by event time scales in the range of 35 to 110 days. These results show the difficulty of explaining the MACHO microlensing events with a single population.

A more quantitative assessment of the compatibility of the different simulated populations with the observational data can be done using the Z^2 compatibility test. The Z^2 statistical test Lucy (2000) is specifically designed to deal with meagre data sets and is thus especially well suited for our case. The results of this compatibility test are presented in Table 5.7 for the different populations under study and for different magnitude cuts. As can be seen, the probability that for our reference magnitude cut (22.5^{mag}) the distributions of microlensing time scales of the canonical thick disk populations are compatible with the observational data are ~ 0.8 , while

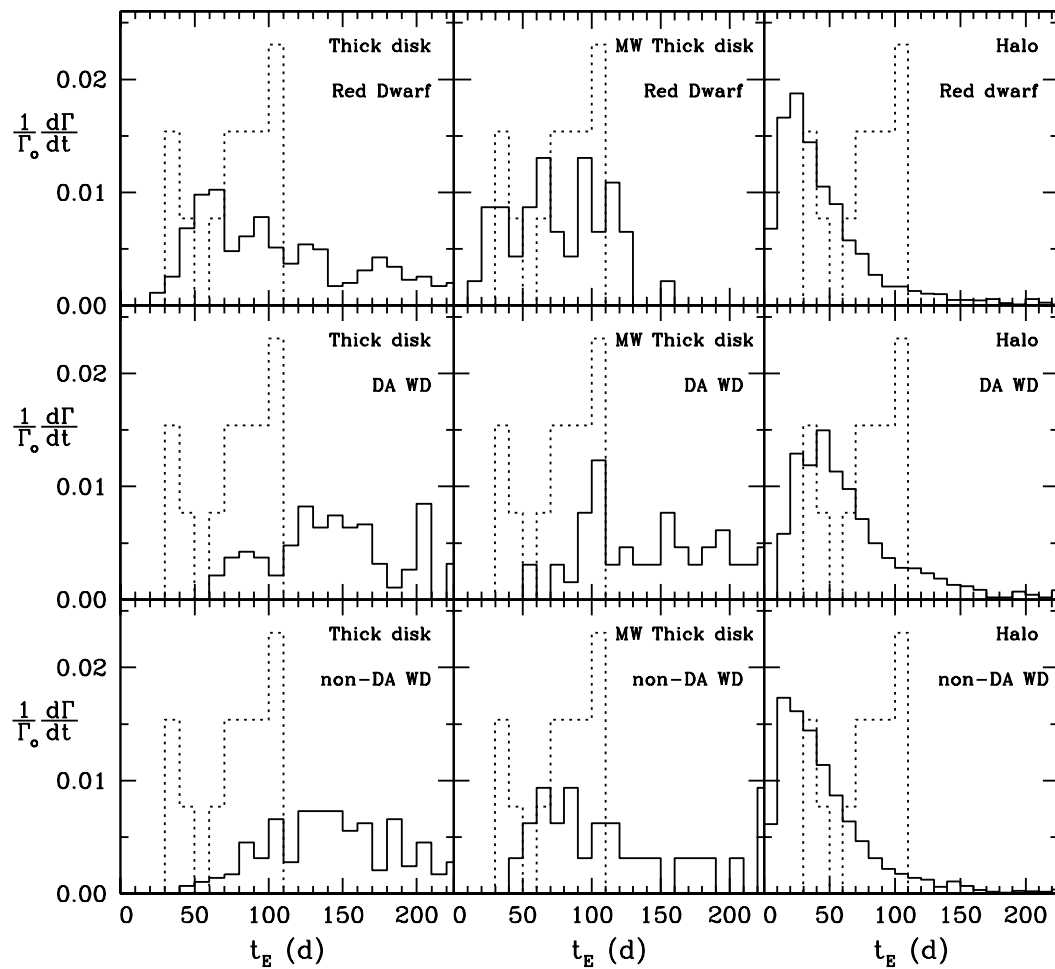


Figure 5.5: Normalized distributions of the microlensing event rate as a function of the event duration for the different population under study (solid lines) and also for the observed microlensing events of the MACHO experiment (dashed lines). All the distributions have been computed for a magnitude cut of 22.5^{mag} .

Z^2 COMPATIBILITY TEST				
Canonical thick disk				
Magnitude	17.5	22.5	27.5	30.0
Red dwarfs	0.87	0.86	0.64	0.39
DA white dwarfs	0.84	0.82	0.68	0.54
non-DA white dwarfs	0.84	0.86	0.82	0.67
Metal-weak thick disk				
Magnitude	17.5	22.5	27.5	30.0
Red dwarfs	0.84	0.73	0.43	0.08
DA white dwarfs	0.76	0.74	0.74	0.01
non-DA white dwarfs	0.70	0.73	0.70	0.41
Halo				
Magnitude	17.5	22.5	27.5	30.0
Red dwarfs	0.54	0.57	0.43	0.37
DA white dwarfs	0.56	0.62	0.71	0.61
non-DA white dwarfs	0.52	0.56	0.56	0.60

Table 5.7: Z^2 compatibility test between the Einstein crossing times obtained by the MA-CHO team and the simulated thick disk and halo populations for different magnitude cuts.

those of the metal-weak thick disk are less probable (~ 0.7) and those of the halo populations are significantly smaller, ~ 0.6 . In particular it is to be noted that the population of red dwarfs and DA white dwarfs of a metal-weak thick disk is practically incompatible with the observational data when a magnitude cut of 30^{mag} is adopted. As previously mentioned, the thick disk populations present wider time scale distributions than the halo (see Fig. 5.5) and, given that the observational results are to some extent spread over a wide range of time scales, the result is that the thick disk populations match the observational distribution better.

Finally, it is interesting to realize that as the magnitude cut becomes larger, the compatibility of the thick disk population with the observational data substantially decreases, while those of the halo white dwarf populations remain almost constant. That is a clear consequence of the different nature of the thick disk and halo white dwarf populations: while the population of thick disk white dwarfs is constituted by bright objects at sufficiently far away distances, the halo white dwarf population is made of intrinsically dim and distant objects.

5.3.5 The joint contribution of the thick disk and halo populations

We have also computed the joint contribution to the microlensing optical depth of the thick disk and halo populations of red dwarfs and white dwarfs. A summary of our results is displayed in Table 5.8 where the same quantities are displayed as

	Canonical thick disk+halo				Metal-weak thick disk+halo			
Magnitude	17.5	22.5	27.5	30.0	17.5	22.5	27.5	30.0
$\langle N_{\text{WD}} \rangle$	0 ± 2	0 ± 2	0 ± 2	0 ± 2	0 ± 2	0 ± 2	0 ± 2	0 ± 2
$\langle N_{\text{RD}} \rangle$	1 ± 2	1 ± 2	0 ± 2	0 ± 2	1 ± 2	1 ± 2	0 ± 2	0 ± 2
$\langle m_{\text{WD}} \rangle (M_{\odot})$	0.613	0.612	0.596	0.607	0.614	0.610	0.644	0.697
$\langle m_{\text{RD}} \rangle (M_{\odot})$	0.360	0.222	0.112	0.084	0.368	0.258	0.098	0.079
$\langle \eta \rangle$	0.446	0.450	0.546	0.998	0.528	0.548	0.944	0.998
$\langle \mu \rangle ('' \text{ yr}^{-1})$	0.008	0.006	0.005	0.005	0.120	0.010	0.009	0.004
$\langle d \rangle (\text{kpc})$	3.20	3.89	4.78	4.85	1.89	2.35	2.59	2.01
$\langle V_{\text{tan}} \rangle (\text{km s}^{-1})$	115	118	114	120	119	124	121	117
$\langle t_{\text{E}} \rangle (\text{d})$	131	146	171	159	103	103	114	106
$\langle \tau / \tau_0 \rangle$	0.738	0.523	0.316	0.093	0.533	0.460	0.238	0.105

Table 5.8: Summary of the results obtained for the thick disk and halo populations of microlenses towards the LMC for the MACHO experiment.

those in Table 5.3 for the case of the halo population and Table 5.5 for the case of the thick disk simulation. We present the outcome for both the cases in which a canonical thick disk (left section) and a metal-weak thick disk (right section) are adopted. Moreover, we only show in this table the results obtained for model B (which we remind is the most realistic model for the white dwarf population) when the results of the MACHO towards the LMC are simulated. The main effect is that the entire population under study can explain about half of the optical depth obtained by the MACHO experiment, irrespective of the adopted thick disk model. This value practically doubles the one obtained when only the halo population was considered. Clearly, these findings indicate that the thick disk population must be taken into account as a potential source of contamination in the current experiments. For a realistic magnitude cut of 22.5^{mag} , a maximum of three microlensing events is expected at the 1σ confidence level, which is far below the ~ 11 microlensing events of the MACHO experiment. Our results show that in the case in which a white dwarf is responsible of the microlensing event, the average mass of the lenses is approximately $0.6 M_{\odot}$, whereas in the case in which the one responsible for the microlensing event is a red dwarf the average mass is $\sim 0.2 M_{\odot}$. Both values are typical of their respective populations. Moreover, in the case of white dwarfs, half of the microlensing events are due to non-DA white dwarfs.

5.3.6 Halo dark matter

In this section we have computed the contribution of the halo populations to the baryonic dark matter density of the Galaxy. The fraction of dark matter in the form of MACHOs, f , can be directly obtained from the microlensing optical depth towards the LMC. Assuming a halo isothermal sphere we have $\tau_{\text{LMC}} = 5.1 \times 10^{-7} f$.

Thus we obtain from our simulations $f = 0.07$ in the case of model A, whereas for model B we derive $f = 0.06$. These values can be compared with our previous results of $f = 0.05$ (Torres et al., 2008). Hence when we include the population of non-DA white dwarfs we find a modest increase, which is still not enough to account for the bulk of halo dark matter.

5.4 Conclusions

We have analyzed the contribution to the microlensing optical depth towards the LMC of the halo population of white dwarfs with both hydrogen-rich and hydrogen-deficient atmospheres. We have used three models to describe the atmospheric evolution of white dwarfs. In the first of these models we have assumed a canonical ratio of hydrogen-rich white dwarfs, to 80% independent of the effective temperature. In our second model, which we consider to be the most realistic one, we have adopted a fraction of white dwarfs with helium-rich atmospheres which depend on the effective temperature. In these two models the cooling sequences of Salaris et al. (2000) for DA white dwarfs and those of Benvenuto & Althaus (1997) for non-DA white dwarfs were used. In the third set of calculations the fraction of non-DA white dwarfs was assumed to depend on the effective temperature, but the cooling tracks of Bergeron et al. (1995) for non-DA white dwarfs were adopted. We have found that when the contribution of hydrogen-deficient white dwarfs is considered, the theoretical optical depth towards the LMC for both the MACHO and EROS experiments is substantially increased by nearly 34%, with respect to previous calculations. Nevertheless, we have also found that no more than one third of the microlensing optical depth found by the MACHO team can be explained by the halo population of white dwarfs at the 1σ confidence level, and that no more than three microlensing events could be expected at the same confidence level in reasonable agreement with the results of the EROS experiment.

We have also studied the role played by the thick disk populations of white dwarfs and red dwarfs, thus extending our previous calculations. For this purpose we have used two thick disk models. The first one is a canonical thick disk model, while the second one corresponds to the most recent model of Carollo et al. (2010), which is based in the data of the Sloan Digital Sky Survey Data Release 7. We have obtained that for both thick disk models, the contribution of these populations to the microlensing optical depth is comparable to that of the halo populations, which is somewhat larger for the canonical thick disk model, which provides an upper limit to this contribution. In particular we have found that the thick disk contribution is dominated by the white dwarf population in both cases, as the contribution of thick disk red dwarfs is only half of that of halo red dwarfs. Besides, we have also found that the average distance of the simulated lenses is very similar for the thick and halo populations, ~ 3 kpc. This unexpected result can be easily explained in terms

of the selection criteria used to decide when a star can be considered responsible of a microlensing event. Since we only consider as reliable microlensing events those in which the lens is dimmer than a certain magnitude cut, intrinsically bright lenses must be located at larger distances. Consequently, since the thick population is intrinsically brighter than the halo population, we only select those thick disk lenses which are far enough away, at distances very similar to those of the halo population, which are naturally located at large distances. We have found as well that although both populations have similar average distances and thick disk objects have smaller average velocities, their event timescales are nearly three times more extended than those of the halo population. We have also assessed the compatibility of our simulated populations with the scarce observational data. We have found that the thick disk population agrees better with the MACHO observational distribution of event timescales than the halo population.

Finally, we found that when both the halo and the thick disk populations are considered, nearly half of the measured value of the microlensing optical depth towards the LMC can be explained at the 95% confidence level by our simulated halo and thick disk populations. According to our simulations, the fraction of halo dark matter that can be expected from MACHOs increases moderately (to $f = 0.06$) with respect to our previous simulations when hydrogen-deficient white dwarfs are taken into account.

Chapter 6

Monte Carlo simulations of the WD+MS population in the SDSS

6.1 Introduction

Close-compact binaries are at the heart of several interesting phenomena in our Galaxy and in other galaxies. In particular, cataclysmic variables, low mass X-ray binaries or double degenerate white dwarf binaries — just to mention the most important and well studied ones — are systems that not only deserve attention by themselves, but also because their statistical distributions are crucial to understand the underlying physics of the evolution during a common envelope episode. Actually, the vast majority of close-compact binaries are formed through at least one common envelope episode. This phase occurs when the more massive star, hereafter the primary, fills its Roche lobe during the first giant branch (FGB) or when it climbs the asymptotic giant branch (AGB). The mass transfer episode is dynamically unstable and the envelope of the giant star engulfs the less massive star, i.e. the secondary, forming a common envelope around both the core of the primary (the future compact star) and the secondary star. Drag forces transfer orbital energy and angular momentum from the orbit to the envelope, leading to a dramatic decrease of the orbital separation, and to the ejection of the common envelope. If the system survives the common envelope phase, the outcome is a post-common envelope binary (PCEB) formed by a compact object and the main sequence companion with an orbital period separation much smaller than that of the original main sequence binary system. The PCEBs studied in detail in this chapter are those in which the compact object is a white dwarf.

Binary systems formed by a white dwarf star and a main sequence companion (WD+MS) are intrinsically one of the most common, and structurally simplest,

population of PCEBs. Thus, the statistical properties of this population are expected to provide crucial observational inputs that are necessary to improve the theory of common envelope evolution (Davis et al., 2010; Zorotovic et al., 2010; De Marco et al., 2011). However, until now, detailed population synthesis studies have failed to effectively constrain the free parameters involved in the formulation of the common envelope phase, due to an utter lack of observational data — see e.g. de Kool (1992), Willems & Kolb (2004), Politano & Weiler (2007), and Davis et al. (2010). In particular, it has been shown that the early sample of well studied PCEBs is not only small but, being drawn mainly from “blue” quasar surveys, it is also heavily biased towards young systems with low-mass secondary stars (Schreiber & Gänsicke, 2003). However, the SDSS (Frieman et al., 2008; Abazajian et al., 2009) has allowed to identify a large number of WD+MS binaries (Heller et al., 2009; Rebassa-Mansergas et al., 2013), and a dedicated radial velocity survey among them has provided the so far largest and most homogeneous sample of close compact binaries with available orbital periods (Rebassa-Mansergas et al., 2008; Nebot Gómez-Morán et al., 2011). Hence, studying the populations of WD+MS binaries that have undergone a common envelope episode it is essential since the distribution of orbital periods and other characteristics of the populations, like the distributions of primary and secondary masses, can be used to constrain the values of the free parameters of the theory of common envelope evolution.

In this chapter we describe the results of a detailed population synthesis study of PCEBs in the Galaxy in which one of the components is a white dwarf whereas the other is a main sequence star. To model the observational selection effects affecting the observed population of WDMS binaries we use the large and well-characterized sample of PCEBs detected in the Sloan Digital Sky Survey (SDSS). A direct comparison of the simulated and the observed sample of PCEBs is performed as well, with the ultimate aim of constraining the current theories of common envelope evolution. The chapter is organized as follows. Sect. 6.2 describes the main features of the simulated population of WD+MS PCEBs. In particular, in this section we explain which are the color cuts employed to cull a representative sample (Sect. 6.2.1), and we also give a detailed description of each of the filters applied to the theoretical sample to take into account the biases of the observational procedure — Sects. 6.2.2, 6.2.3, and 6.2.4. Sect. 6.3 presents the main results of our simulations. Specifically, in this section we discuss the biases of the observational sample, followed by an exhaustive analysis of the mass and period distributions of the simulated sample, which are then compared with the observational distributions. In this section a comprehensive statistical study of some selected models is also done with the aim of constraining the parameters involved in the calculation of the common envelope phase. Finally, Sect. 6.4 closes the chapter with a summary of our main findings and our concluding remarks.

6.2 The simulated population of WD+MS PCEBs

We expanded an existing Monte Carlo code (García-Berro et al., 1999, 2004) specifically designed to study the Galactic population of single white dwarfs to deal with one observed population of binaries in which one of the components is a white dwarf. In Sect. 2.3 we described in detail the most important ingredients of our Monte Carlo simulator. Consequently, here we will only discuss the specific methods necessary to deal with the photometric and spectroscopic selection criteria, and their associated biases.

Specifically, in chapter 2 we thoroughly described how we simulated the WD+MS PCEB population in the Galaxy in the directions of the SDSS DR7 spectroscopic plates — see Fig. 6.1 — and how we computed the SDSS *ugriz* magnitudes of the entire simulated sample. Given that the main purpose of this chapter is to perform a detailed comparison of the simulated and the observed WD+MS binary populations in the SDSS that underwent a common envelope phase, it becomes necessary to incorporate the observational selection effects in a very realistic and detailed way. In the subsequent subsections we describe how we modeled these selection biases.

6.2.1 Color cuts

Our first step consisted in applying a color filter. The color cuts allow to observationally cull WD+MS binary systems from the spectroscopic SDSS DR7 WD+MS binary catalog (Rebassa-Mansergas et al., 2012). From this sample, we only considered systems observed by the SDSS Legacy survey (see Fig. 6.1), as WD+MS binaries identified by SEGUE — Sloan Extension for Galactic Understanding and Exploration (Yanny et al., 2009) — were selected following a completely different algorithm (Rebassa-Mansergas et al., 2012). For magnitudes within the range $15 < i < 19.5$ the color cuts we applied to the synthetic sample were the following — see also Rebassa-Mansergas et al. (2013):

$$(u - g) < 0.93 - 0.27 \times (g - r) - 4.7 \times (g - r)^2 + \\ + 12.38 \times (g - r)^3 + 3.08 \times (g - r)^4 - \\ - 22.19 \times (g - r)^5 + 16.67 \times (g - r)^6 - \\ - 3.89 \times (g - r)^7$$

$$-0.5 < (g - r) < 1.7$$

$$-0.4 < (r - i) < 1.8$$

and

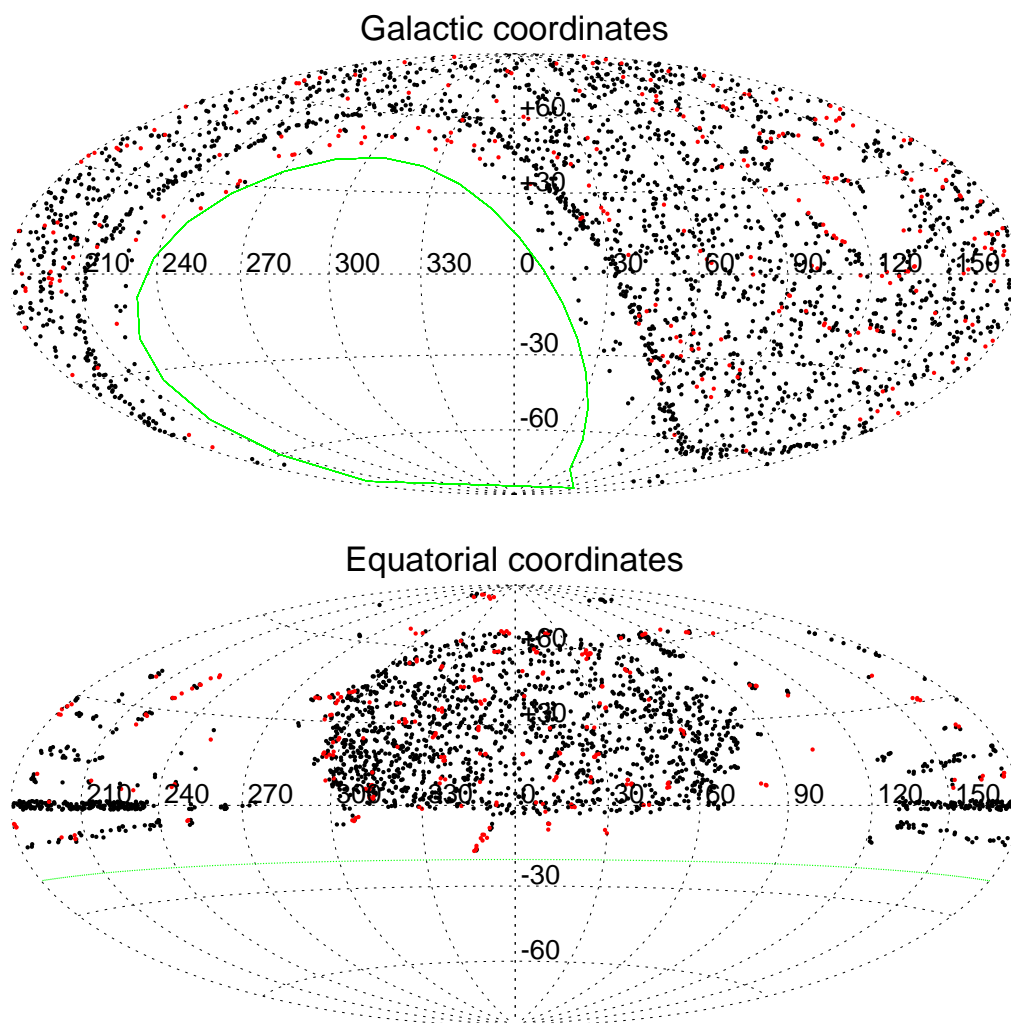


Figure 6.1: Position of Legacy (black) and SEGUE (red) SDSS DR7 WD+MS binaries in Galactic and equatorial coordinates. Taken from Rebassa-Mansergas et al. (2012).

Table 6.1: Total number and percentage of simulated WD+MS binary systems obtained after applying the successive selection criteria.

	Model 1				
	He	C/O - O/Ne	Total	Filtered (%)	Cumulative (%)
Unfiltered sample	8 344 (36%)	14 834 (64%)	23 178	—	100
Color cuts	980 (57%)	740 (43%)	1 720	7.42	7.42
Spectroscopic completeness	35 (70%)	15 (30%)	50	2.91	0.21
Intrinsic binary bias	13 (65%)	7 (35%)	20	40.00	0.86
Period filter	8 (67%)	4 (33%)	12	60.00	0.05
	Model 2				
	He	C/O - O/Ne	Total	Filtered (%)	Cumulative (%)
Unfiltered sample	12 499 (30%)	28 890 (70%)	41 389	—	100
Color cuts	1 478 (52%)	1 365 (48%)	2 843	6.87	6.87
Spectroscopic completeness	66 (62%)	41 (38%)	107	3.76	0.26
Intrinsic binary bias	22 (58%)	16 (42%)	38	35.51	0.09
Period filter	14 (61%)	9 (39%)	23	60.52	0.06
	Model 3				
	He	C/O - O/Ne	Total	Filtered (%)	Cumulative (%)
Unfiltered sample	17 674 (25%)	53 023 (75%)	70 697	—	100
Color cuts	2 596 (47%)	2 927 (53%)	5 523	7.81	7.81
Spectroscopic completeness	126 (56%)	99 (44%)	225	4.03	0.32
Intrinsic binary bias	40 (55%)	33 (45%)	73	32.44	0.10
Period filter	28 (65%)	15 (35%)	43	58.90	0.06

$$\begin{aligned}
(g-r) &< 2 \times (r-i) + 0.38 && \text{if } -0.4 < (r-i) \leq 0.1 \\
(g-r) &< 0.5 && \text{if } 0.1 < (r-i) \leq 0.3 \\
(g-r) &< 4.5 \times (r-i) - 0.85 && \text{if } 0.3 < (r-i) \leq 0.5 \\
(g-r) &< 0.25 \times (r-i) + 1.3 && \text{if } 0.5 < (r-i) \leq 1.8
\end{aligned}$$

6.2.2 Spectroscopic completeness

The main science driver of the SDSS Legacy survey was to acquire spectroscopy for magnitude-limited samples of galaxies (Strauss et al., 2002) and quasars (Richards et al., 2002). Because of their composite nature, WD+MS binaries form a “bridge” in the color space that connects the white dwarf locus with that of low-mass stars (Smolčić et al., 2004). The blue end of the bridge, characterized by WD+MS binaries with hot white dwarfs and/or late type companions, strongly overlaps with the color locus of quasars, and was therefore intensively targeted for spectroscopy by the SDSS Legacy Survey. In contrast, the red end of the bridge is dominated by WD+MS binaries containing cool white dwarfs, and excluded from the quasar program. Thus, the next step in producing realistic simulations of the PCEB population is to apply a spectroscopic completeness correction that takes into account the probability of a given simulated PCEB with appropriate colors to be spectroscopically observed by the SDSS Legacy survey.

To estimate this probability we proceeded as follows. We first calculated the spectroscopic completeness of each WD+MS binary observed by the SDSS DR 7 Legacy Survey — see Fig. 6.1, which is taken from Rebassa-Mansergas et al. (2012). It is important to keep in mind that these observed WD+MS binaries include wide systems that never interacted during their evolution and PCEBs, and that only PCEBs are considered in the numerical sample. Strictly speaking we should consider then only those observed WD+MS binaries that are PCEBs. However, the number of known PCEBs is just ~ 10 per cent of the entire WD+MS binary observed population. Besides, there is no reason to believe that the spectroscopic completeness will vary from wide to close WD+MS binaries. In order to avoid low number statistics in our calculations we thus decided to use the entire observed sample, i.e. wide WD+MS plus PCEBs. We did exclude however WD+MS binaries that are resolved in their SDSS images, as these are associated to large uncertainties in their photometric magnitudes. The resulting sample contains 1 645 systems.

We obtained the $u-g$, $g-r$, $r-i$ and $i-z$ colors of each of our 1 645 observed WD+MS binaries, and defined a four-dimension (one dimension per color) sphere of 0.2 color radius around each of them. Within each sphere we calculated via DR 7 `casjobs` (Li & Thakar, 2008) the number of point sources with clean photometry (M_{phot}) as well as the number of spectroscopic sources (N_{spec}). This search was restricted to those systems fulfilling the color cuts given in Sect. 6.2.1. The choice of a sphere radius of 0.2 ensures that N_{spec} is larger than 15 in each case. The spec-

troscopic completeness of each of the observed WD+MS systems is simply given by $N_{\text{spec}}/N_{\text{phot}}$. The probability for a simulated PCEB to be observed spectroscopically by the Legacy survey of SDSS finally corresponds to the spectroscopic completeness of the observed WD+MS binary with the most similar colors, i.e. the closest color distance (as defined by the four colors) between the simulated WD+MS binary and the observed systems.

6.2.3 Intrinsic WD+MS binary bias

It is expected that a certain fraction of the simulated WD+MS PCEBs should contain primary or secondary stars that would be undetectable in the spectrum if observed spectroscopically by the SDSS. This is the case when one of the stellar components is considerably brighter than the other and overshines the companion. For late-type secondary stars, this implies an upper limit on the white dwarf effective temperature, at which we would be able to discern the companion in the SDSS spectrum. Conversely, the detection of white dwarfs next to early-type companions results in a lower limit on the white dwarf effective temperature. In addition, SDSS spectra of farther objects are associated to lower signal-to-noise ratio. Our observed sample of WD+MS PCEBs is partially based on the visual identification of both binary components in the SDSS spectrum (Rebassa-Mansergas et al., 2010), and consequently objects with low signal-to-noise ratio may have not passed the identification criteria. This implies an upper limit in the distance of WD+MS binaries. These two effects need to be taken into account in our simulated sample of WD+MS PCEBs.

In order to evaluate the above described selection effects we followed the approach adopted by Rebassa-Mansergas et al. (2011) and used the white dwarf atmosphere models of Koester et al. (2005) and the M-dwarf templates of Rebassa-Mansergas et al. (2012) to obtain synthetic composite WD+MS binary spectra in the wavelength range and resolution provided by typical SDSS spectra for a wide range of white dwarf effective temperatures (T_{eff} ranging from 6 000 to 100 000 K in 37 steps nearly equidistant in $\log T_{\text{eff}}$) and surface gravities (covering from $\log g = 6.5$ to 9.5 in steps of 0.5), spectral type of the companions (M0–9, in steps of one subclass), and distances (from 50 to 1 700 pc in steps of 50 pc). To the complete set of synthetic composite spectra we added artificial Gaussian noise varying according to the distance used. Specifically, the noise level introduced to the composite spectra reproduces the signal-to-noise ratio that the observed WD+MS binary spectra have at the considered distance.

Once the synthetic spectra were obtained, we subjected the complete sample to the identification criteria defined for real WD+MS binary spectra in SDSS, namely a visual inspection of the spectra, and a search for blue and red excess in those spectra dominated by the flux of the secondary star and white dwarf components, respectively — see Rebassa-Mansergas et al. (2010) for details. In addition we calculated the *ugriz* magnitudes from the synthetic spectra and excluded all systems

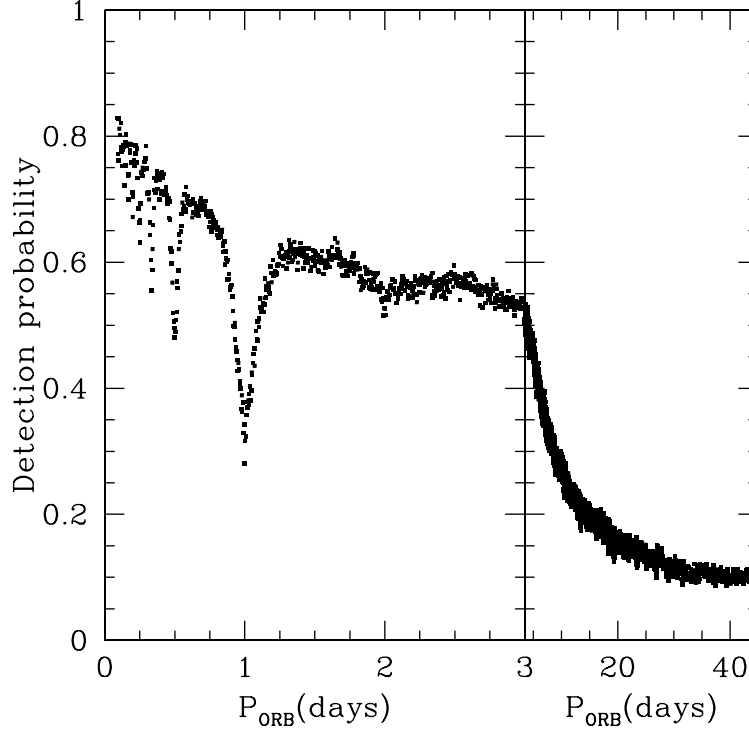


Figure 6.2: Detection probability of a PCEB as a function of the orbital period.

exceeding the magnitude limits given in Sect. 6.2.1. From the resulting sample we then evaluated the WD effective temperature and distance limits that were then applied accordingly to the sample of WD+MS binaries obtained from the Monte Carlo simulator.

6.2.4 PCEB orbital period filter

Finally, we filtered our simulated binary systems according to a period efficiency function, which measures the probability of identifying a PCEB among the WD+MS SDSS sample. The detection probability function (Nebot Gómez-Morán et al., 2011) is shown in Fig. 6.2. As can be seen, the probability of finding a binary system decreases for increasing periods, and drops rapidly for those systems with period larger than 3 days. For orbital periods of one day or multiples of one day the probability for sampling the same orbital phase increases, which translates in a decrease of the period efficiency function.

6.3 Results

6.3.1 The observational sample

The sample of binary systems that we use for comparison consisted on 53 WD+MS PCEBs from the SDSS DR7 catalogue with known periods — see Rebassa-Mansergas et al. (2012), Nebot Gómez-Morán et al. (2011) and Zorotovic et al. (2010), and references therein. As we already mentioned, SEGUE systems have been excluded. The periods are well determined, and therefore the distribution of periods is useful to compare with the period distribution obtained for the simulated systems. To compare with our models, we are also interested in knowing the core composition of the white dwarf in the observed systems, to estimate the fraction of systems containing He white dwarfs, and also the number of systems containing more massive oxygen-neon white dwarfs. To do this we proceeded as follows. If the mass of a white dwarf is smaller than $0.5 M_{\odot}$ we assumed that it has a He core. On the contrary, if the mass of a white dwarf is larger than $0.5 M_{\odot}$ but smaller than $1.1 M_{\odot}$ a carbon-oxygen core was adopted. Finally, if the mass of the white dwarf is larger than $1.1 M_{\odot}$ an oxygen-neon core was adopted. For 49 of the 53 PCEBs in the sample, it has been possible to determine the mass of the white dwarf using the method described by Rebassa-Mansergas et al. (2007). As in Zorotovic et al. (2010), in order to determine their compositions we decided to exclude systems with white dwarf temperatures below 12000 K, because the spectral fitting methods are not reliable for cooler white dwarfs and therefore their masses can not be trusted. This implies that reliable white dwarf masses can be obtained for 40 of the 53 systems that form our observed sample, of which 14 have a He white dwarf, 23 a carbon-oxygen white dwarf and 2 an oxygen-neon white dwarf. There is also one system with $M_{\text{WD}} = 0.5 M_{\odot}$ for which we can not decide which type of white dwarf it is. This corresponds to a fraction of $36 \pm 8\%$ of He white dwarfs in the sample, where we have assumed binomial errors.

6.3.2 Overview of the simulations

We computed a large number (~ 500) of Monte Carlo simulations covering a wide range of values of the common envelope efficiency parameter, $0.0 \leq \alpha_{\text{CE}} \leq 1.0$, and the fraction of the thermal energy available to eject the common envelope, $0.0 \lesssim \alpha_{\text{int}} \lesssim 0.3$, which can result in very large values of the binding energy parameter, λ . We also performed simulations in which λ was computed including the contribution of different fractions of the internal energy, α_{int} . All this was done for the three IMRDs, $n(q)$, previously mentioned in Sect. 2.3. For each of our models we generated 10 independent Monte Carlo simulations (with different initial seeds) and for each of these Monte Carlo realizations, we increased the number of simulated Monte Carlo realizations to 10^4 using bootstrap techniques. Using this procedure we ensure convergence in all the final values of the relevant quantities. In what

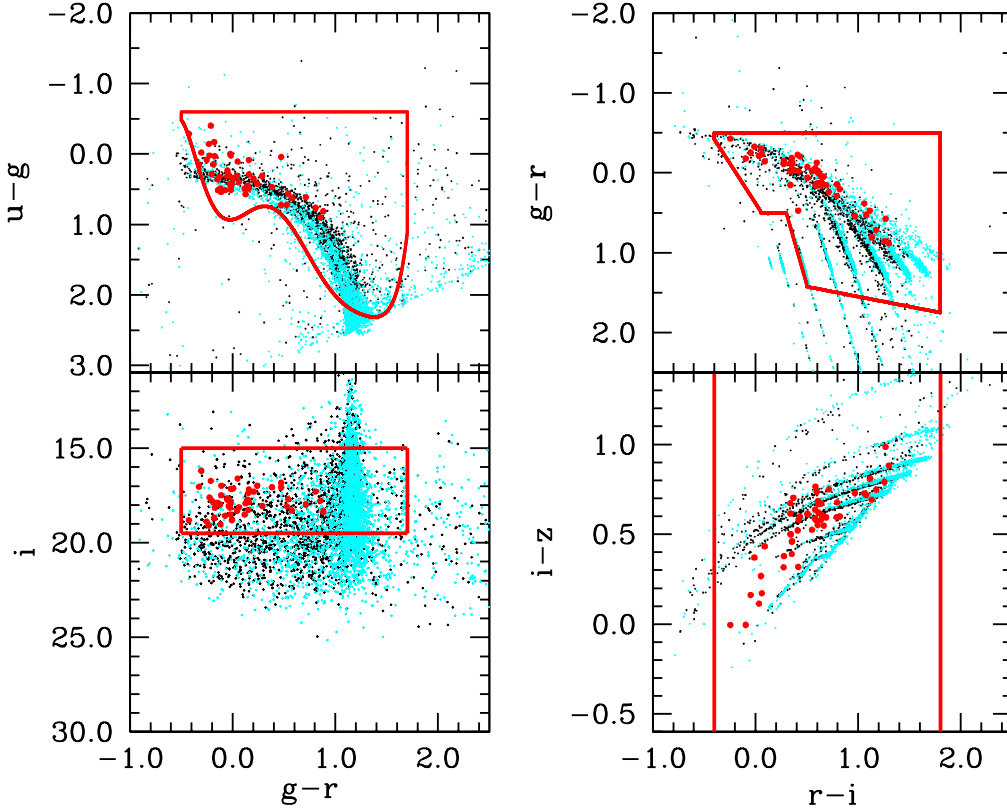


Figure 6.3: Color-color diagram of the synthetic WD+MS PCEBs obtained using our Monte Carlo simulator when our reference model ($\alpha_{\text{CE}} = 1.0$, $\lambda = 0.5$, and $n(q) = 1$) is employed. Systems containing He white dwarfs are represented using black dots, while light blue dots correspond to systems with carbon-oxygen or oxygen-neon white dwarfs. The observed WD+MS PCEB systems are displayed using red dots. The color selection criteria are shown using red lines (Sect. 6.2.1).

follows we describe the model predictions and compare them with the observations. Given that the parameter space of common envelope evolution is very large, we show in this paper only those results which imply some relevant differences between the corresponding models.

6.3.3 Color-color space

We first investigate whether the simulated PCEB population is placed in the same regions in the color-color space as the observed PCEBs. To that end, and for the sake of definiteness, we define a reference model for which we considered $\alpha_{\text{CE}} = 1.0$, $\lambda = 0.5$, and a flat IMRD, $n(q) = 1$. This choice of parameters should not be considered

as a representative case, and we use it just to illustrate the effects of the different filters applied to the simulated samples. Moreover, we adopted this model because it represents an extreme (albeit frequently employed) case among the many possible choices of the free parameters of common envelope evolution. Figure 6.3 shows an example of the color-color diagram of present-day WD+MS PCEBs obtained in a typical Monte Carlo realization for our reference model. Systems which underwent the common envelope phase before He ignition (case B) contain He white dwarfs and are represented by black dots. Systems which underwent the common envelope episode after He ignition during the early AGB (case C) or during the thermally pulsing AGB phase (TPAGB) contain carbon-oxygen or oxygen-neon white dwarfs and are displayed using light blue dots. Red dots correspond to the observational WD+MS PCEBs. The different color cuts discussed in the Sect. 6.2.1 are represented by red lines. A quick look at Fig. 6.3 reveals that our simulations recover fairly well the observed population of WD+MS PCEBs in the different color-color diagrams, and that our synthetic WD+MS PCEBs overlap with the real ones. Moreover, our simulated population lies within the region allowed by the different color cuts. However, as expected, the entire simulated Galactic population of PCEBs occupies a region larger than the observational one, especially in the i vs. $g-r$ color-magnitude diagram. Finally, we note as well that the discrete cyan tracks come from the fact that we are mapping main sequence stars onto discrete spectral types.

6.3.4 The effects of biases and selection criteria

The effect of each filter over the simulated WD+MS PCEBs is illustrated in Fig. 6.4 for our reference model in the $g-r$ versus i color-magnitude diagram. Each panel represents the systems that survive after consecutively applying the filter indicated on it. We show the effect of the color selection filter (upper-left panel), the result of applying the spectroscopic completeness filter (upper-right panel) to the previous sample, the effect of using the intrinsic binary bias filter (lower-left panel), and finally the result after using the period filter (lower-right panel). As can be seen, the different filters applied to the original synthetic sample (black and light blue dots) severely reduce the total number of observable objects, which is consistent (within an order of magnitude) with the observational sample (red symbols).

In order to quantitatively analyze the effects of the different selection criteria on the entire population of simulated WD+MS PCEBs, we show in table 6.1 the total number and percentage (in parentheses) of WD+MS PCEBs initially simulated and obtained after applying consecutively the selection criteria and observational biases described in Sects. 6.2.1 to 6.2.4. We also list in the last column of this table the cumulative percentage of the WD+MS population obtained after applying the selection cuts. We show the results for three representative models. Model 1 is our reference model, previously described. In model 2 we also used $\alpha_{\text{CE}} = 1.0$ and $\lambda = 0.5$, but we adopted $n(q) \propto q^{-1}$, to illustrate the effects of the IMRD. Finally,

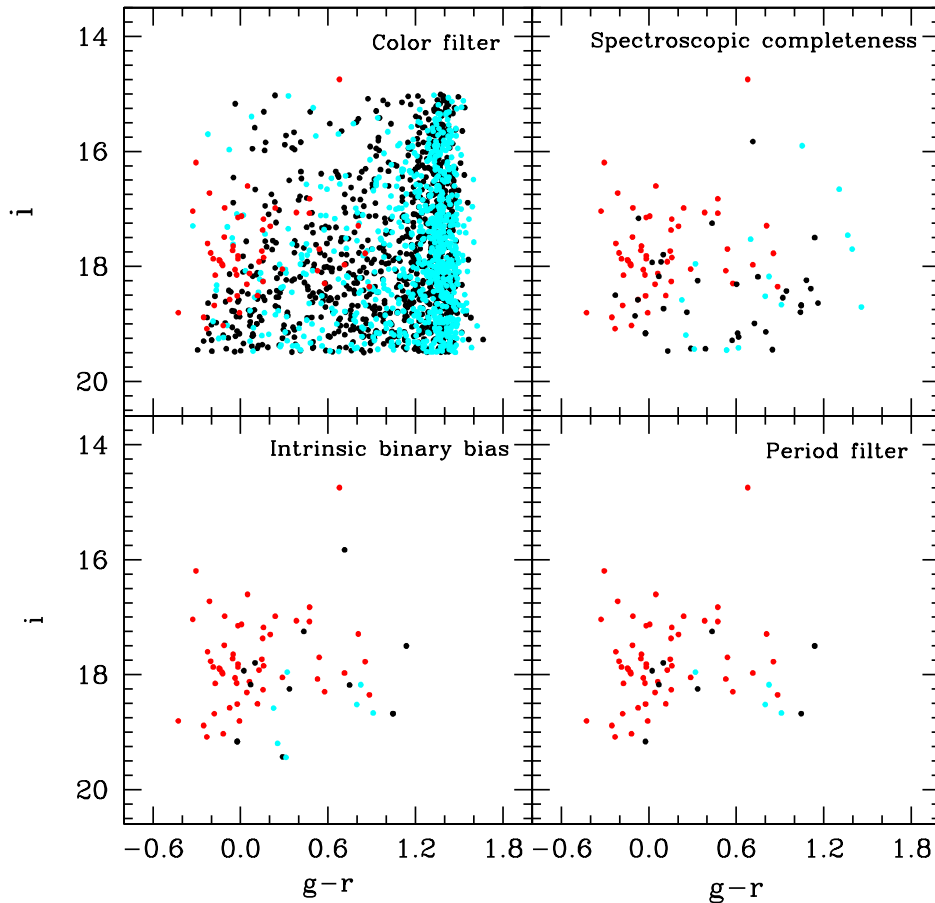


Figure 6.4: Color-magnitude diagram of the synthetic WD+MS PCEBs obtained using our Monte Carlo simulator (light blue and black dots) compared with the observational systems (red symbols) after applying the different filters explained in the text to our reference model. Colors are the same as in Fig. 6.3.

for model 3 we adopted $\alpha_{\text{CE}} = 0.3$, and $n(q) \propto q^{-1}$, while λ was computed for every binary assuming $\alpha_{\text{int}} = 0.2$. The selection criteria produce a dramatic decrease of the total number of simulated WD+MS PCEBs, independently of the adopted model. In particular, the final simulated population is smaller than 0.1% of the initial sample for all three models — see the last column of this table. The most restrictive selection criteria are the color cuts and the spectroscopic completeness filter. Only $\sim 7\%$ of the objects in the input sample pass the cuts in colors and magnitude for all three

models, while the spectroscopic completeness filter eliminates $\sim 97\%$ of those that survive the first filter. If only these two filters are applied the total population of potentially observable systems decreases drastically down to $0.2 - 0.3\%$ of the unfiltered sample. This behavior can be easily explained. First, the SDSS only covered $15 < i < 19.5$ and most WD+MS binaries in our Galaxy are obviously fainter. Second, the SDSS was primarily designed to detect galaxies and quasars and thus the probability for a WD+MS binary system to be spectroscopically detected by the SDSS is relatively small, specially for WD+MS binaries containing cool white dwarfs (Rebassa-Mansergas et al., 2013). The remaining filters, i.e. the intrinsic binary bias filter and the period filter, further reduce the size of the sample of simulated PCEBs systems. In particular, the intrinsic binary bias filter reduces the number of systems surviving the spectroscopic completeness filter to about $30 - 40\%$, whilst the period filter reduces the sample of systems that survive the spectroscopic completeness filter to $\sim 60\%$. Thus, the selection criteria play a crucial role since only $\sim 0.05\%$ of the simulated binary systems survive the successive filters.

The final number of WD+MS PCEBs predicted to be identified by the SDSS is in reasonable agreement with the observed number of systems (see table 6.1). This indicates that both our initial assumptions as well as the computation of the selection effects and biases are likely good representations of reality. However, it is important to realize that the number of predicted PCEBs depends somewhat on the adopted values of α_{CE} and λ during the common envelope phase. We obtain the best agreement (i.e. the largest number of predicted systems) assuming a variable binding energy parameter and a small common envelope efficiency, namely for model 3.

Interestingly, the selection criteria employed to select the sample introduce an unexpected bias in the observed population of WD+MS PCEBs, as the fraction of systems containing He WDs that are finally culled from the total population increases independently of the model, from $\sim 25 - 35\%$ to $\sim 60 - 70\%$. This implies that the observed population of WD+MS PCEBs is severely biased as a consequence of the selection criteria employed to cull it, and that WD+MS PCEBs containing a He white dwarf are over-represented in the final sample, independently of the adopted model, due to the observational selection effects.

6.3.5 The role of the enhanced mass-loss parameter

It has been suggested (Tout & Eggleton, 1988) that the presence of a close companion could enhance mass loss during the red giant phase. As shown in Eq. (2.7) the mass-loss tidal enhancement depends on a parameter, B_W , which at present is unknown. To evaluate the influence of this parameter on the resulting population of WD+MS PCEBs, and to better constrain the value of this enhancement parameter, we performed an additional set of simulations in which we adopted several values for B_W , ranging from 0 (no tidal enhancement) to 10^3 . The results of such simulations are presented in Table 6.2, where we show the percentages of He and

Table 6.2: Enhanced mass-loss parameter and white dwarf percentages.

Model 1				
B_W	0	10	10^2	10^3
He (%)	67 ± 12	72 ± 8	76 ± 8	77 ± 8
CO/ONe (%)	33 ± 12	28 ± 8	24 ± 8	23 ± 8
Model 2				
B_W	0	10	10^2	10^3
He (%)	61 ± 10	62 ± 7	65 ± 7	76 ± 7
CO/ONe (%)	39 ± 10	38 ± 7	35 ± 7	24 ± 7
Model 3				
B_W	0	10	10^2	10^3
He (%)	62 ± 10	63 ± 7	68 ± 7	75 ± 8
CO/ONe (%)	38 ± 10	37 ± 7	32 ± 7	25 ± 8

carbon-oxygen (or oxygen-neon) white dwarfs in WD+MS PCEBs for several values of B_W , after applying all the selection effects to the three models previously described in Sect. 6.3.4. These percentages are computed as the ensemble average of a sufficiently large number of individual Monte Carlo realizations, for which we also compute the corresponding standard deviations. Both are listed in Table 6.2. In general, the percentage of He white dwarfs increases as $\log B_W$ increases. We stress that even for a small value of the enhancement parameter, the percentage of He white dwarfs is somewhat large, at odds with the observational data set we are using to compare, for which the fraction of helium white dwarfs is $\sim 40\%$ (see Sect. 6.3.1). Consequently, small values of B_W seem to be more compatible with the observational data. For this reason in the simulations described in what follows we adopted $B_W = 0$, which is a conservative choice.

6.3.6 The effects of the binding energy parameter

Since more than a decade we know that assuming a constant binding energy parameter λ is probably not a good approximation (Dewi & Tauris, 2000). Instead λ depends on the mass and the evolutionary stage. We explore this issue in Figs. 6.5 and 6.6 where we show from top to bottom: the distributions of the binding energy parameter (λ), primary ZAMS masses, white dwarf masses and periods, as a function of the radius of the primary just prior to the common envelope episode, i.e. of its Roche-lobe radius. We compare here two models, both with $\alpha_{\text{CE}} = 0.3$ — which is consistent with the results of Zorotovic et al. (2010) — and $n(q) = 1$, but with $\alpha_{\text{int}} = 0.0$ or $\alpha_{\text{int}} = 0.2$, respectively. We have chosen these two particular models to highlight the effects of including a fraction of the internal energy of the envelope

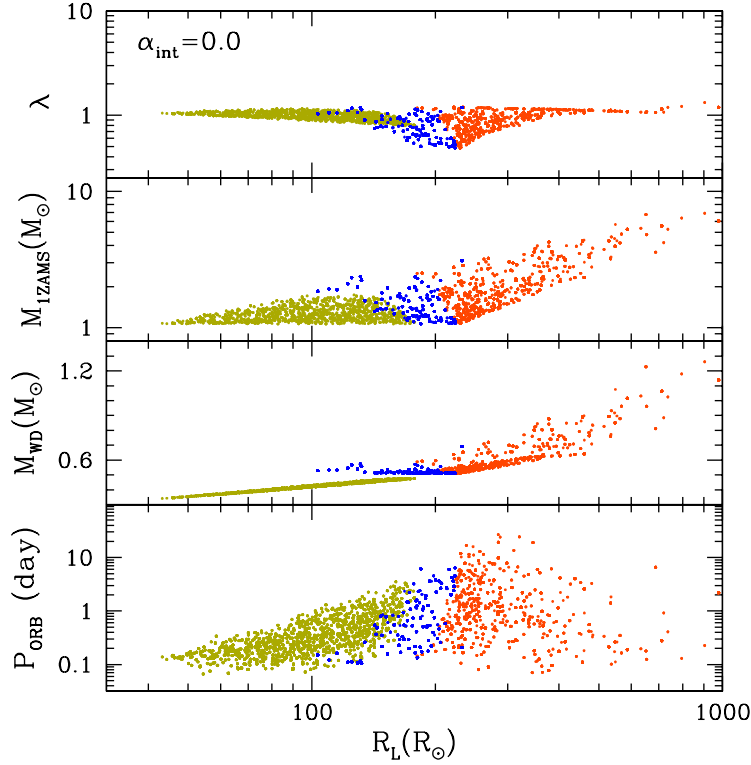


Figure 6.5: From top to bottom: binding energy parameter, primary ZAMS mass, white dwarf mass and orbital period as a function of the Roche-lobe radius. The case B, case C and TPAGB common envelope episodes are represented using green, blue and red dots, respectively. We show the results for a model in which $\alpha_{\text{CE}} = 0.3$, $n(q) = 1$ and without fraction of the internal energy contributing to expel the envelope ($\alpha_{\text{int}} = 0.0$).

that helps in the ejection process. Fig. 6.5 displays the results for the model in which $\alpha_{\text{int}} = 0.0$, while Fig. 6.6 displays the results for the model with $\alpha_{\text{int}} = 0.2$. Systems that have experienced a case B common envelope episode are displayed using green dots, while blue dots show the WD+MS systems which underwent a case C common envelope episode and red dots those in which a TPAGB common envelope episode took place. As can be seen in this figure, for those models in which no internal energy is available to eject the envelope, the value of λ remains practically constant and with a relatively small dispersion which increases first with increasing Roche-lobe radius, until it reaches a maximum at $R_L \sim 200 R_\odot$, and then decreases again for larger values of R_L (see the top panel of Fig. 6.5). On the other hand, when a moderate amount of internal energy is available to eject the envelope we find an overall enhancement of the resulting values of λ (top panel of Fig. 6.6). This was expected since the contribution of the internal energy becomes more important for more extended envelopes, where the gravitational energy becomes smaller and the

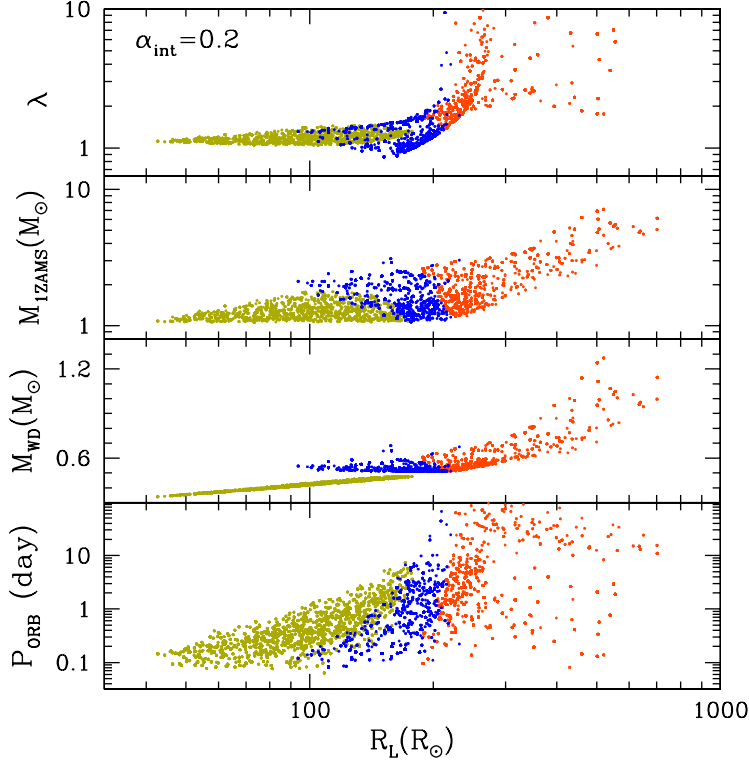


Figure 6.6: Same as Fig. 6.5, but for a model in which $\alpha_{\text{int}} = 0.2$, being the rest of the parameters the same.

envelope is less tightly bound. Moreover, this enhancement is more noticeable for the largest values of the Roche-lobe radius at which the CE episode occurs. We also find that the dispersion in the values of λ increases for wider systems. The distributions of primary ZAMS masses and white dwarf masses as a function of the Roche-lobe radius is rather similar for both models (second and third panel from top, respectively). Finally, the distribution of orbital periods is also very similar in both cases, except for a population of long period ($\gtrsim 10$ days) PCEBs, descending from the initially more separated systems. This is only observed when a fraction of the internal energy of the envelope is taken into account. In summary, the only relevant differences between both models are the distribution of the values of λ and the existence of systems with very long final periods, being the rest of the distributions very similar.

6.3.7 The fraction of PCEBs containing He white dwarfs

One important and relatively robust value that can be derived from the observed sample is the fraction of PCEBs containing He-core white dwarfs. We therefore here

Table 6.3: Percentage of systems with He white dwarfs and Kolmogorov-Smirnov test of the period distribution for six representative models with $\lambda = 0.5$.

	$n(q) \propto q^{-1}$		$n(q) = 1$		$n(q) \propto q$	
α_{CE}	1.0	0.25	1.0	0.25	1.0	0.25
He(%)	67 ± 12	47 ± 15	61 ± 10	47 ± 12	70 ± 10	45 ± 12
KS	0.46 ± 0.31	0.53 ± 0.31	0.54 ± 0.30	0.56 ± 0.29	0.58 ± 0.29	0.54 ± 0.29

compare the percentage of white dwarfs with He cores in the final sample of our simulations with that of the observational sample, which is around 40%.

In table 6.3 we display the percentage of He white dwarfs, as well as the results of a Kolmogorov-Smirnov test resulting from a comparison between the observed and the theoretical period distributions (we will describe and discuss the Kolmogorov-Smirnov test in Sect. 6.3.8), for some of the Monte Carlo simulations in which a fixed value of $\lambda = 0.5$ was adopted, for the three IMRDs. We emphasize that for the sake of conciseness in this table only a selected handful of models is shown. However, the actual number of models analyzed is much larger. The results displayed in table 6.3 — and those obtained from similar models not explicitly shown here — show that only the models for which a small value of α_{CE} is adopted produce the required percentage of helium white dwarfs. In all the models in which α_{CE} is larger than 0.3 the fraction of white dwarfs with helium cores is significantly larger than the observed value, $36 \pm 8\%$. This is true for all three IMRDs.

Table 6.4 shows the same results but for the case in which λ is computed for different values of α_{int} . Again we do this for several values of α_{CE} , α_{int} (with $\alpha_{\text{int}} \leq \alpha_{\text{CE}}$), and for the three IMRDs. Based on our previous results, we only show here the results for our models with $\alpha_{\text{CE}} \leq 0.3$. Again, the fraction of white dwarfs with helium cores depends sensitively on the adopted value of α_{CE} , and also a bit on α_{int} . In particular, as α_{CE} is increased the percentage of helium white dwarfs also increases, independently of the adopted IMRD.

6.3.8 The period distribution

The parameter of PCEBs that can be most accurately measured is the orbital period. Thus, comparing the predicted and observed orbital period distribution is crucial. We performed Kolmogorov-Smirnov tests to estimate the similitude of the theoretical and observational period distributions. We restrict ourselves to models with $\alpha \leq 0.3$ as otherwise the fraction of PCEBs containing He-core white dwarfs drastically disagrees with the observations (see previous section). All models with $\alpha_{\text{CE}} \leq 0.3$ reproduce reasonably well the observed orbital period distribution which is indicated by Kolmogorov-Smirnov values exceeding 0.2. This means that there are no significant indications for the simulated and the observed distribution to be dif-

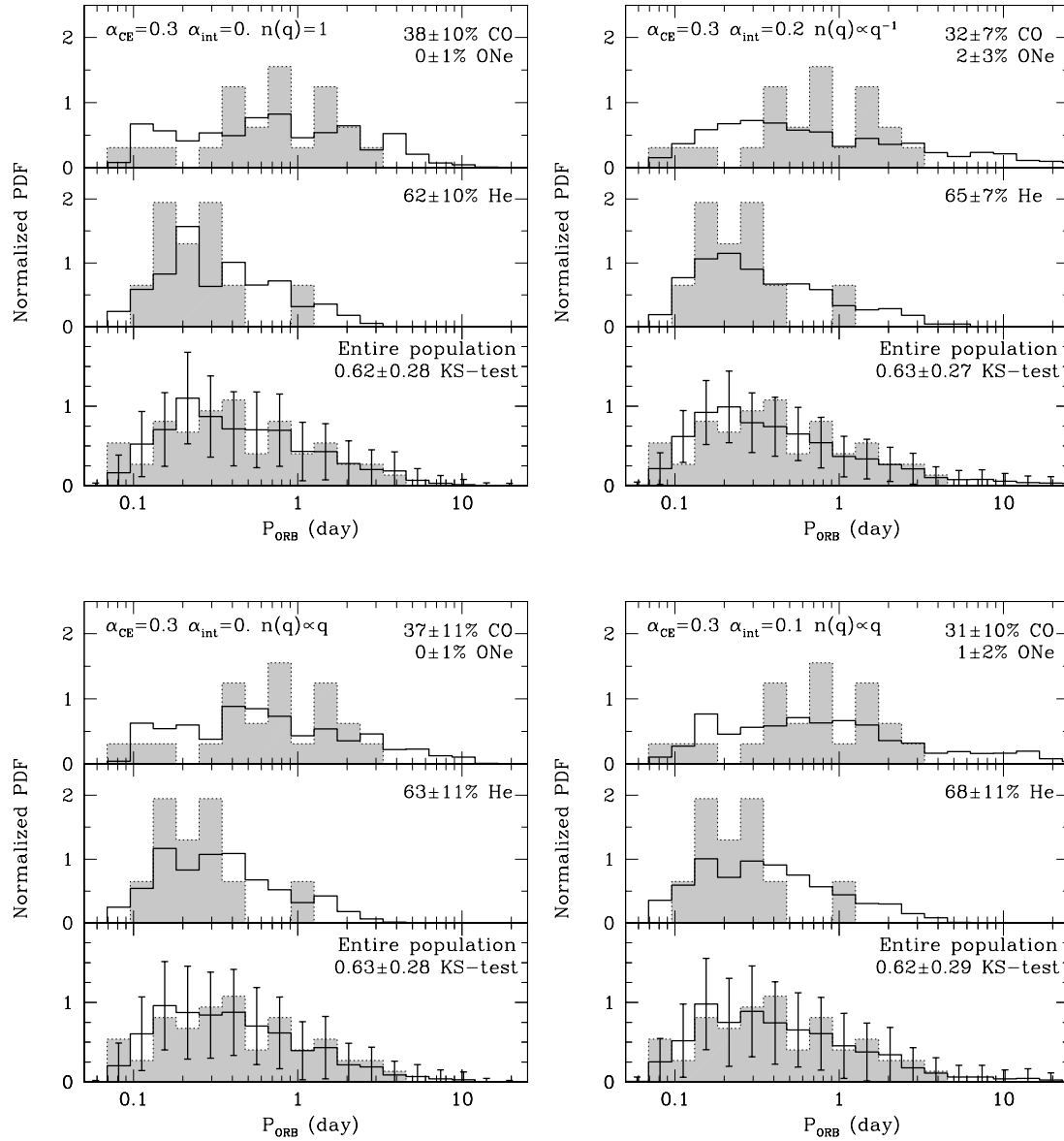


Figure 6.7: Period histograms (normalized to unit area) of the distribution of present-day WD+MS PCEBs for our four best models (black line) compared with the observational distribution (dotted line, gray histogram).

ferent. We obtain the largest Kolmogorov-Smirnov values (exceeding 0.6) for models with $\alpha_{\text{CE}} = 0.3$. In what follows we describe the results obtained for those models that best fit the period distribution in some more detail.

For the sake of conciseness we only considered those models with a Kolmogorov-Smirnov value larger than 0.6, and with a percentage of WD+MS PCEBs with He-core white dwarfs smaller than 70%. Once these criteria are employed we are left with only four models. The first model has $\alpha_{\text{int}} = 0.2$ and $n(q) \propto q^{-1}$, the second one has $\alpha_{\text{int}} = 0$ and $n(q) = 1$, the third one has $\alpha_{\text{int}} = 0$ and $n(q) \propto q$, and finally the fourth one has $\alpha_{\text{int}} = 0.1$ and $n(q) \propto q$. Note that all the models correspond to a common envelope prescription in which λ is computed for each binary. Among these four best models there is a degeneracy between the adopted prescription for the common envelope phase and the IMRD. This implies that on the basis of the present observational data we cannot determine which is the IMRD.

In Figure 6.7 we compare the distribution of periods of the present-day WD+MS PCEBs simulated sample (white histograms, solid lines) with the observational one (gray histograms, dotted lines). We show the period distributions for the entire sample of WD+MS PCEBs (bottom panel of each figure) but also separately for systems containing helium white dwarfs (middle panels) and carbon-oxygen or oxygen-neon white dwarfs (top panels). From the 40 systems with white dwarf mass determination and white dwarf temperature larger than 12 000 K described in Sect. 6.3.1, we found that six of them, with masses close to $0.5 M_{\odot}$, can contain either a helium white dwarf or a carbon-oxygen one, given their mass error. Of the 34 remaining systems, 11 contain a helium white dwarf and 23 a carbon-oxygen or an oxygen-neon one. These are the systems that were considered for the middle and top panels, respectively, while the bottom panels contain the 53 systems with available periods. In general, our Monte Carlo simulations agree well with the observational period distribution for the entire population. However, the still large observational error bars and the almost negligible differences between the different theoretical models preclude from drawing definite conclusions of which of these is the best one. This is indicative that the selection criteria dominate the final observational distribution. Nevertheless, a detailed inspection of Fig. 6.7 reveals that those models with non-zero internal energy present slightly extended tails in the long-period end of the distribution. Even though these tails possibly could not be statistically significant, their mere existence provides a hint that these models do not describe appropriately the ensemble properties of the period distribution of WD+MS PCEBs. Consequently, this compels us to consider as more convenient those models with a small amount of internal energy.

Table 6.4: Percentage of systems with He white dwarfs and Kolmogorov-Smirnov test of the period distribution for our models with $\alpha_{\text{CE}} \leq 0.3$ and λ properly computed for each system, where different fractions of internal energy are taken into account.

$n(q)$	$\propto q^{-1}$			1			$\propto q$		
	$\alpha_{\text{int}} = 0.0$								
α_{CE}	0.1	0.2	0.3	0.1	0.2	0.3	0.1	0.2	0.3
He (%)	37 ± 13	50 ± 14	58 ± 8	38 ± 15	53 ± 14	62 ± 10	41 ± 15	57 ± 12	63 ± 11
KS	0.20 ± 0.25	0.38 ± 0.31	0.49 ± 0.31	0.35 ± 0.30	0.52 ± 0.31	0.62 ± 0.28	0.37 ± 0.31	0.54 ± 0.30	0.63 ± 0.28
	$\alpha_{\text{int}} = 0.1$								
α_{CE}	0.1	0.2	0.3	0.1	0.2	0.3	0.1	0.2	0.3
He (%)	48 ± 13	55 ± 13	64 ± 8	47 ± 15	56 ± 14	65 ± 10	52 ± 15	63 ± 11	68 ± 11
KS	0.48 ± 0.31	0.53 ± 0.30	0.56 ± 0.29	0.48 ± 0.31	0.55 ± 0.30	0.57 ± 0.30	0.44 ± 0.31	0.59 ± 0.29	0.62 ± 0.29
	$\alpha_{\text{int}} = 0.2$								
α_{CE}	0.1	0.2	0.3	0.1	0.2	0.3	0.1	0.2	0.3
He (%)	—	59 ± 13	65 ± 7	—	57 ± 17	72 ± 10	—	64 ± 11	70 ± 10
KS	—	0.55 ± 0.30	0.63 ± 0.27	—	0.58 ± 0.29	0.61 ± 0.29	—	0.58 ± 0.29	0.62 ± 0.29
	$\alpha_{\text{int}} = 0.3$								
α_{CE}	0.1	0.2	0.3	0.1	0.2	0.3	0.1	0.2	0.3
He (%)	—	—	69 ± 9	—	—	70 ± 11	—	—	71 ± 10
KS	—	—	0.55 ± 0.30	—	—	0.50 ± 0.31	—	—	0.58 ± 0.30

Table 6.5 contains the statistics obtained for our four best models. This table also shows that those models with non-zero values of the internal energy parameter have maximum periods much larger (a factor of ~ 10) than the ones in which $\alpha_{\text{int}} = 0.0$ is adopted, while the minimum periods remain nearly the same. The average value for the periods is therefore larger when we include a fraction of internal energy, which is specially true for systems containing a carbon-oxygen or an oxygen-neon white dwarf. This is clearly expected. Those models in which no internal energy is available to eject the common envelope fit better the measured average period of the observed distribution of WD+MS PCEBs ($\langle P \rangle = 0.69$ days). It is as well interesting to remember that the internal energy becomes specially important for more evolved primaries, which have a more massive core (the future white dwarf) and a more extended envelope. For this reason those simulations in which $\alpha_{\text{int}} \neq 0$ have an enhanced production of WD+MS systems with an oxygen-neon white dwarf, because it becomes easier for these systems to survive a common envelope phase due to this additional source of energy. This is an important fact, because in the observational sample there are only two WD+MS PCEBs in which the resulting white dwarf has a mass larger than $1.1 M_{\odot}$. All in all, we conclude that to account for the ensemble properties of the distribution of periods and the detection of a small fraction of WD+MS PCEBs with very massive white dwarfs, the fraction of the internal energy available to eject the envelope must be small.

Finally, it is worth mentioning that the average periods for the two sub-populations of white dwarfs with helium and carbon-oxygen or oxygen-neon cores, are markedly different, being that of WD+MS systems with helium core white dwarfs significantly smaller than that of systems with more massive white dwarfs. This is in agreement with the observational analysis of Zorotovic et al. (2011). If one separates He-core and carbon-oxygen or oxygen-neon core systems, however, the number of observed systems becomes too small to separately compare model predictions and observations.

6.3.9 Period-mass distribution

Figures 6.8 and 6.9 show the period-mass distributions of the simulated PCEBs for two of our best models ($\alpha_{\text{CE}} = 0.3$ and $n(q) \propto q$) without and with the inclusion of internal energy ($\alpha_{\text{int}} = 0.0$ and $\alpha_{\text{int}} = 0.1$, respectively). For each model the left panels show the distribution of orbital periods as a function of the white dwarf mass, while the right panels show the same distribution as a function of the mass of the secondary. As in Fig. 6.7 the top panels show the sub-population of systems containing carbon-oxygen or oxygen-neon white dwarfs, the middle panels those with helium white dwarfs, whilst the bottom panels show the distributions for the entire population.

Clearly, our simulations match remarkably well the observed distribution of WD+MS PCEBs (magenta squares). It is interesting to note that the WD+MS

Table 6.5: Statistics for the best models.

$n(q)$	$\propto q^{-1}$	1	$\propto q$	$\propto q$
α_{CE}	0.3	0.3	0.3	0.3
α_{int}	0.2	0.0	0.0	0.1
$N_{\text{WD+MS}}$	42 ± 6	24 ± 5	19 ± 5	20 ± 5
He (%)	65 ± 7	61 ± 10	63 ± 11	68 ± 11
CO (%)	32 ± 7	38 ± 10	37 ± 11	31 ± 11
ONe (%)	3 ± 3	0 ± 1	0 ± 1	1 ± 2
$\langle P \rangle$ (days)	1.54 ± 7.20	0.80 ± 1.32	0.73 ± 1.33	1.36 ± 7.16
$\langle P \rangle_{\text{He}}$ (days)	0.57 ± 0.74	0.50 ± 0.50	0.51 ± 0.52	0.61 ± 0.67
$\langle P \rangle_{\text{CO}}$ (days)	3.52 ± 12.24	1.40 ± 1.24	1.17 ± 1.75	3.13 ± 12.27
P_{min} (days)	0.049	0.067	0.068	0.067
P_{max} (days)	325	32	41	313

binary systems that contain a helium white dwarf (middle panels of Figs. 6.8 and 6.9) occupy a narrow strip in white dwarf masses and, moreover, the periods of these systems cluster around 0.2–0.3 days. All this is in excellent agreement with the properties of the observed sub-population of WD+MS PCEBs with helium white dwarfs. For those WD+MS binaries containing carbon-oxygen or oxygen-neon white dwarfs (top panels of Figs. 6.8 and 6.9) the distribution of white dwarf masses is considerably broader, and most of the white dwarf masses of our synthetic sub-population are below $1.1 M_{\odot}$, and thus are carbon-oxygen white dwarfs. Our simulations also predict that WD+MS PCEBs containing an oxygen-neon white dwarf are possible, although these systems should be rare, specially when no internal energy is included. This is again consistent with the observational sample, where only 2 systems contain an oxygen-neon white dwarf. The periods of WD+MS PCEBs with carbon-oxygen or oxygen-neon white dwarfs also span a larger range, with typical periods ranging from ≤ 0.1 to ~ 4 days, also in good agreement with the observations. When all the WD+MS PCEBs with available period and masses are considered (bottom panels) the agreement with the observed distribution is excellent.

6.4 Summary and conclusions

In this chapter we presented a comprehensive set of Monte Carlo simulations of the population of WD+MS PCEBs in the SDSS. Our simulations encompass a very broad range of possible situations, including three IMRDs, different prescriptions for the treatment of the common envelope episode, and of the parameters controlling the tidally enhanced mass loss during this phase. In our simulations we included all the known systematic observational biases. We found that the color cuts reduce con-

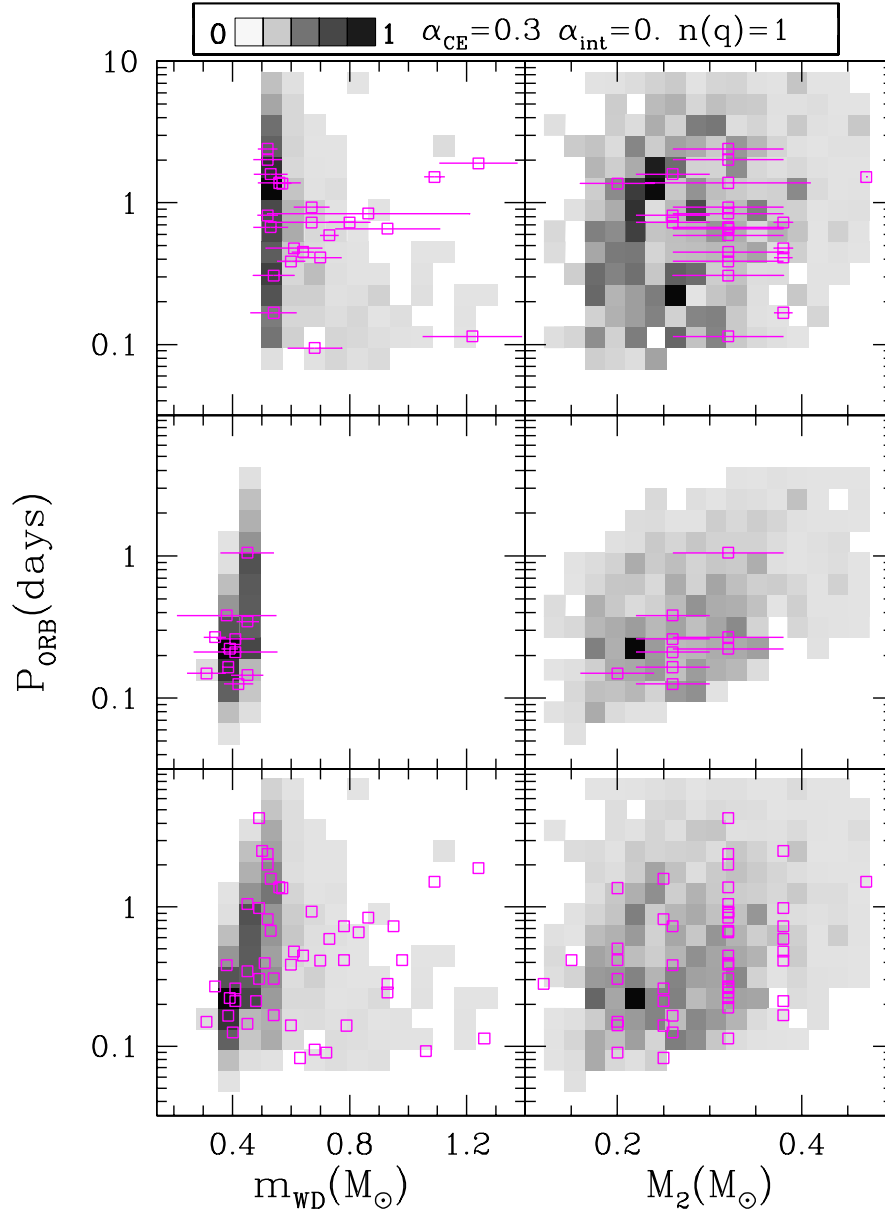


Figure 6.8: Period-mass density distribution of present-day WDMS systems for our best model with $n(q) = 1$ and no internal energy parameter compared with the observational distribution (magenta squares).

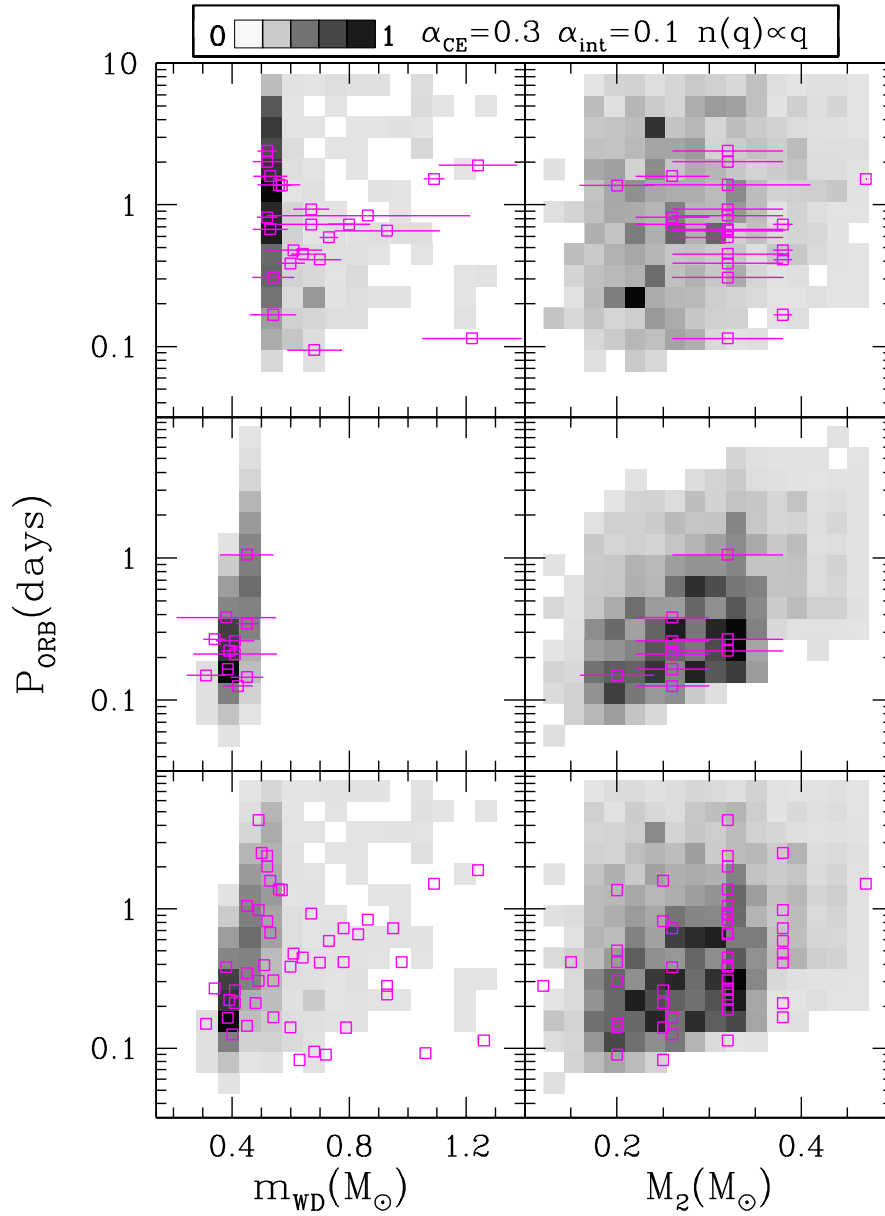


Figure 6.9: Period-mass density distribution of present-day WDMS systems for our best model with $n(q) \propto q$ and non-zero internal energy parameter compared with the observational distribution (magenta squares).

siderably the initial sample, and that typically only $\sim 7\%$ of the simulated WD+MS PCEBs survive the cuts. The number of surviving systems is further reduced when the spectroscopic completeness filter is applied, leaving only $\sim 3\%$ of the systems that previously survived the color cuts. The intrinsic binary bias and the period filter additionally reduce the total size of the simulated samples, resulting in total sample sizes which are of the order of $\sim 0.1\%$ of the initial one. All in all, our simulations show that, given the actual observational capabilities, we are probing a very limited number of WD+MS PCEBs, and that the observational sample suffers from poor statistics. This prevents from drawing definite conclusions about the overall properties of the WD+MS PCEB population, despite the huge observational efforts done so far. Additionally, we also find that the population of WD+MS PCEBs containing helium white dwarfs is over-represented within SDSS due to selection effects. Here we simulated the entire process of discovery, PCEB identification, and orbital period determination of PCEBs discovered by SDSS and compared model predictions and observations. Our results can be summarized as follows:

- Even for small values of the mass loss enhancement parameter the percentage of helium white dwarfs is at odds with that observationally found. However, small values of this parameter agree better with the observational data set.
- In agreement with our findings in Zorotovic et al. (2014), a small value of the common envelope efficiency ($\alpha_{\text{CE}} \leq 0.3$) is required to reproduce the observed fraction of PCEBs containing He-core white dwarfs.
- Models with a variable binding energy parameter seem to fit better the observed distribution of periods than models in which the binding energy parameter is assumed to be constant.
- Our results also show that large values of α_{int} are ruled out by the observations, although the ensemble properties of the population of WD+MS PCEBs do not allow us to discard small values of α_{int} , say smaller than 0.2, approximately.
- We have also compared the distribution of orbital periods as a function of the mass and find excellent agreement with the observational data. Our simulations can not only reproduce the distribution of orbital periods, but also the observed period distribution as a function of the mass of the white dwarf if small values for the common envelope efficiencies and a detailed prescription of the binding energy parameter are assumed.

The present analysis suffers from the still scarce number of WD+MS PCEBs that have been identified in an homogenous way. This prevents us to draw more definite conclusions. However, evidence for small common envelope efficiencies is growing.

Chapter 7

Conclusions

7.1 Gravitational microlensing and halo dark matter

We have designed and implemented a Monte Carlo simulator in order to understand the contribution of white dwarfs to the microlensing event rates towards the Large Magellanic Cloud (LMC) reported by the MACHOs and EROs surveys. This study takes as a reference previous studies which only analyzed the expected contribution of carbon-oxygen white dwarfs with pure hydrogen atmospheres. The studies presented in this work include both halo and thick disk populations of all types of white dwarfs in addition to the population of red dwarfs.

7.1.1 The contribution of oxygen-neon white dwarfs

In a first step we analyzed the contribution of oxygen-neon white dwarfs with pure hydrogen atmospheres to the MACHO content of the Galactic halo. We found that although oxygen-neon white dwarfs fade to invisibility very rapidly and, thus, they are good baryonic dark matter candidates, their contribution to the microlensing optical depth towards the LMC is rather limited. In particular, we found that when the contribution of oxygen-neon white dwarfs is taken into account the microlensing optical depth does not increase significantly, independently of the adopted initial mass function. If the microlensing optical depth is adopted to be that of the MACHO experiment, $\tau_0 = 1.2 \times 10^{-7}$ (Alcock et al., 2000) — which probably is an overestimate — we found that the fraction of the microlensing optical depth due to the entire white dwarf population, that is white dwarfs with carbon-oxygen cores and oxygen-neon cores with atmospheres made of pure hydrogen, is at most $\sim 13\%$ in the case in which a standard initial mass function is adopted and $\sim 19\%$ if the log-normal initial mass function of Adams & Laughlin (1996) is considered. These values are roughly $\sim 3\%$ larger than those already found by García-Berro et al. (2004), who only considered the contribution of carbon-oxygen white dwarfs. We also studied if some of the candidate white dwarfs of the Hubble Deep Field South could be oxygen-

neon white dwarfs, and we found that most probably this is not the case. Finally, we also discussed the contribution of the entire white dwarf population to the mass of the Galactic halo. We found that this contribution is of the order of a modest 5% in the most optimistic case. The specific reason for this is clear. Although oxygen-neon white dwarfs are more massive than their carbon-oxygen counterparts, their contribution is heavily suppressed by the steep decline of the initial mass function for increasing masses. All in all, we conclude that oxygen neon white dwarfs with pure hydrogen atmospheres are not significant contributors to the mass of the Galactic halo.

7.1.2 The contribution of halo red dwarfs

We also extended our previous study of the contribution to the halo dark matter of the white dwarf population and included the Galactic population of halo red dwarfs. Specifically, we computed the contribution of these objects to the microlensing optical depth towards the LMC and compared our estimate with the measurements of the MACHO and EROS collaborations. Our estimate is based on a series of Monte Carlo simulations that incorporate the most up-to-date evolutionary tracks for red dwarfs, carbon-oxygen white dwarfs, and oxygen-neon white dwarfs, and reliable models of our Galaxy and the LMC. We found that the contribution of the red dwarf population practically doubles the contribution found so far for the white dwarf population. Our results indicate that the entire population of these stars can account for at most ~ 0.3 of the optical depth found by the MACHO team. This value implies that the contribution of the full range of masses between 0.08 and $10 M_{\odot}$ represents 5% of the halo dark matter with an average mass of $0.4 M_{\odot}$. Although this result is in partial agreement with the 95% confidence level MACHO estimate for a standard isothermal sphere and no halo LMC contribution, the expected number of events obtained by our simulations (3 events at the 95% confidence level) is substantially below the 13 to 17 observed MACHO events. Moreover, we also assessed the compatibility between the observed event rate distribution and the ones obtained for the different populations under study. Our results show that the carbon-oxygen white dwarf population can reproduce fairly well the observed event rate distribution although, as mentioned earlier, the expected number of events is considerable smaller. On the other hand, the negative results obtained by the EROS team towards the LMC are in agreement with our standard halo simulation. Finally, and for the sake of completeness, we studied the effects of a log-normal biased initial mass function. In this case, the contribution of the red dwarf population is only marginal given that the production of low-mass stars is strongly inhibited. Accordingly, the total contribution to the microlensing optical depth is not different from that found in previous studies of the white dwarf contribution.

7.1.3 The contribution of hydrogen-deficient white dwarfs

We also analyzed the contribution to the microlensing optical depth towards the LMC of the population of halo white dwarfs with hydrogen-deficient atmospheres. We used three models to describe the atmospheric evolution of white dwarfs. In the first of these models we assumed a canonical ratio of hydrogen-rich to hydrogen-deficient white dwarfs, namely 80%, independently of the effective temperature. In our second model, which we consider to be the most realistic one, we adopted a fraction of white dwarfs with helium-rich atmospheres which depends on the effective temperature. In these two models the cooling sequences of Salaris et al. (2000) for DA white dwarfs and those of Benvenuto & Althaus (1997) for non-DA white dwarfs were used. In the third set of calculations the fraction of non-DA white dwarfs was assumed to depend on the effective temperature, but the cooling tracks of Bergeron et al. (1995) for non-DA white dwarfs were adopted. We found that when the contribution of hydrogen-deficient white dwarfs is considered, the theoretical optical depth towards the LMC for both the MACHO and EROS experiments is substantially increased, by nearly 34% with respect to previous calculations. Nevertheless, we also found that no more than one third of the microlensing optical depth found by the MACHO team can be explained by the halo population of white dwarfs at the 1σ confidence level, and that no more than three microlensing events could be expected at the same confidence level in reasonable agreement with the results of the EROS experiment.

We have also studied the role played by the thick disk populations of white dwarfs and red dwarfs, thus extending our previous calculations. For this purpose we used two thick disk models. The first one is a canonical thick disk model, while the second one corresponds to the most recent model of Carollo et al. (2010), which is based in the data of the Sloan Digital Sky Survey Data Release 7. We obtained that for both thick disk models, the contribution of these populations to the microlensing optical depth is comparable to that of the halo populations. We note that this contribution is somewhat larger for the canonical thick disk model, which therefore provides an upper limit to this contribution. In particular, we found that the thick disk contribution is dominated by the white dwarf population in both cases, as the contribution of thick disk red dwarfs is only half of that of halo red dwarfs. Besides, we have also found that the average distance of the simulated lenses is very similar for the thick and halo populations, ~ 3 kpc. This unexpected result can be easily explained in terms of the selection criteria used to decide when a star can be considered responsible of a microlensing event. Since we only consider as reliable microlensing events those in which the lens is dimmer than a certain magnitude cut, intrinsically bright lenses must be located at larger distances. Consequently, since the thick population is intrinsically brighter than the halo population, we only select those thick disk lenses which are far enough away, at distances very similar to those of the halo population, which are naturally located at large distances. We found as well that although both populations have similar average distances and thick disk

objects have smaller average velocities, their event timescales are nearly three times more extended than those of the halo population. We also assessed the compatibility of our simulated populations with the scarce observational data. We found that the thick disk population agrees better with the MACHO observational distribution of event timescales than the halo population. Finally, we found that when both the halo and the thick disk populations are considered, nearly half of the measured value of the microlensing optical depth towards the LMC can be explained at the 95% confidence level by our simulated halo and thick disk populations. According to our simulations, the fraction of halo dark matter that can be expected from MACHOs increases moderately (to $f = 0.06 - 0.07$) with respect to our previous results ($f = 0.05$) when hydrogen-deficient white dwarfs are taken into account.

7.1.4 Summary

To sum up, our findings show that neither white dwarfs nor red dwarfs can be major contributors to the microlensing optical depth towards the LMC. Hence, they cannot account for the bulk of dark matter. Our simulations are in good agreement with the results of the EROS survey (Goldman et al., 2002), and with other similar theoretical (although not as complete as ours) studies (Isern et al., 1998; Koopmans, 2002; Bennett, 2005), and also with studies based on the chemical evolution of our Galaxy (Canal et al., 1997; Gibson & Mould, 1997; Komatsu et al., 2011). Our findings reinforce the idea, previously pointed out by other studies, that the optical depth found by the MACHO survey is most likely an overestimate, probably due to contamination of self-lensing objects — see, for instance, Besla et al. (2013) — among other possible explanations.

7.2 White dwarf-main sequence binaries in the SDSS-DR7

We designed and implemented a Monte Carlo simulator aimed to study the properties of a sample of white dwarf-main sequence binaries, taking into account the different biases of the sample. Also, we carried on a comprehensive set of Monte Carlo simulations of the population of white dwarf plus main sequence binary systems in the Sloan Digital Sky Survey. Our simulations encompass a very broad range of possible situations, including three distributions of secondary masses, different prescriptions for the treatment of the common envelope episode, and of the parameters controlling the tidally enhanced mass loss during this phase. In our simulations we included all the known systematic observational biases, among which we mention the photometric selection effects (including detailed color cuts), the spectroscopic completeness of the sample, the intrinsic binary bias, and the efficiency detection resulting from the distribution of the observed period distribution. Additionally, our population

synthesis code incorporates detailed and up-to-date descriptions of the most important necessary physical and astronomical inputs. In particular, we use reliable white dwarf cooling sequences for helium, carbon-oxygen, and oxygen-neon white dwarfs, and main sequence lifetimes. We also employed a recent initial mass function and the most recent available initial-final mass relationship. We adopted as well the most commonly used distributions of initial orbital separations and eccentricities, and we also used standard prescriptions to compute the Galactic distributions of the binary systems.

Armed with these tools we first studied how the different photometric selection cuts affect the final size of the theoretical sample. We found that the color cuts reduce considerably the initial sample, and that typically only $\sim 7\%$ of the simulated systems survive the cuts. The number of surviving systems is further reduced when the spectroscopic completeness filter is applied, leaving only $\sim 3\%$ of the original synthetic systems. The intrinsic binary bias and the period filter additionally reduce the total size of the simulated samples, resulting in total sample sizes which are of the order of $\sim 0.2\%$ of the initial one. All in all, our simulations show that, given the actual observational capabilities, we are probing a very limited number of systems, and that most possibly the observational sample suffers from poor statistics. This, in conclusion, very likely prevents from drawing definite conclusions about the overall properties of the distribution of systems, despite the huge observational efforts done so far. Additionally, we also find that the population of pairs containing white dwarfs with helium cores is over-represented in the final sample.

Nevertheless, given that the size of the sample has noticeably increased during the last years we studied how the different theoretical prescriptions compare with the wealth of observational data. We started studying the role of the enhanced mass-loss parameter during the red giant phase due to the presence of a close companion. We found that even for small values of the enhancement parameter the percentage of helium white dwarfs is at odds with that observationally found, and that only small values of this parameter are compatible with the observational data set. We then studied the effects of a variable binding energy parameter, finding that the distributions of the most relevant quantities (mass of the primary at the common envelope episode, white dwarf mass and final orbital period) are not markedly affected by the choice of the fraction of the thermal energy available to eject the common envelope, α_{int} . The only distribution that changes noticeably is the distribution of binding energy parameters, λ , as it should be expected.

We then compared the results of our population synthesis studies with the observational data. Specifically, we compared the results of our Monte Carlo simulations with the observed period distribution of post-common envelope systems, and the fraction of systems with helium core white dwarfs in the SDSS. We computed a large number of simulations covering a wide range of values of the common envelope efficiency parameter, α_{CE} , and the binding energy parameter, λ in which we adopted the most standard inputs for the rest of the necessary prescriptions. We also com-

puted another set of Monte Carlo calculations in which a variable λ was adopted, for different values of the internal energy parameter, α_{int} . All this was done for three different secondary mass distributions, a flat one, a mass distribution inversely proportional to $q = M_2/M_1$, and a mass distribution of secondaries which increases linearly with q . Although the observational error bars are still large, we were able to discard a significant number of models, whereas a reduced set of models presented a nice agreement with the observational distributions. Using a Kolmogorov-Smirnov test we ended up with four models which are able to match both the percentage of helium white dwarfs in the SDSS sample, and the observed distribution of periods. All these models were computed adopting $\alpha_{\text{CE}} = 0.3$, but different distributions of secondary masses and different values of the fraction of thermal energy available to eject the common envelope, α_{int} . We found that a degeneracy between the distribution of secondary masses and the value of α_{int} exists. Nonetheless, our results show that large values of this parameter are ruled out by the observations, although the ensemble properties of the population of this kind of systems do not allow us to discard small values of α_{int} , say smaller than 0.2, approximately. Instead, our simulations show that models with a variable binding energy parameter seem to fit better the observed distribution of periods and the fraction of helium white dwarfs in the SDSS sample than models in which the binding energy parameter is assumed to be constant.

Finally, we studied as well the distribution of orbital periods as a function of the masses of the primary and the secondary, and for two of the simulations discussed before we found an excellent agreement with the observational data. These simulations were obtained using $\alpha_{\text{CE}} = 0.3$, $n(q) = 1$ and $\alpha_{\text{int}} = 0$, and $\alpha_{\text{CE}} = 0.3$, $n(q) = q$ and $\alpha_{\text{int}} = 0.1$, respectively. These simulations reproduce not only the distribution of orbital periods, the fraction of helium white dwarfs but also the observed period distribution as a function the mass of the white dwarf, for carbon-oxygen white dwarfs, helium white dwarfs and for the entire population of white dwarfs. Consequently our simulations yield support to the hypothesis that some moderate fraction (of the order of $\sim 10\%$) of the thermal energy is used to eject the common envelope. However, the scarce number of WDMS systems, although largely increased by the discoveries of the SDSS and the subsequent analysis, prevents us from drawing definite conclusions on this issue.

Appendix A

Schmidt's estimator

The Schmidt's estimator, also known as the $(1/V_{\max})$ method, is a non-parametric method used to calculate the luminosity function for a complete sample of objects. It was first designed and used by Schmidt (1968) in the studies of the quasar population, and later on it was extended to proper motion selected samples (Schmidt, 1975). Some time later Felten (1976) made a generalization of the method introducing the dependence on the direction of the sample. This issue results to be essential when considering non-uniform distributions of objects. For instance, when the effects of the Galactic scale height need to be considered. On the other hand, it has been mathematically demonstrated that the $(1/V_{\max})$ method is an unbiased estimator for a sample limited in proper motion and apparent magnitude. For all of these reasons the $(1/V_{\max})$ method is widely used to estimate the luminosity function of the white dwarf population. Here we describe the main ingredients of this method.

First of all we consider the radial distance from the observer. Thus, for each white dwarf of the sample we obtain the maximum distance r_{\max} and the minimum distance r_{\min} at which the white dwarf would still belong to the sample. These values are calculated using the expresions:

$$r_{\max} = \pi^{-1} \min \left[(\mu/\mu_l); 10^{0.2(m_f-m)} \right] \quad (\text{A.1})$$

$$r_{\min} = \pi^{-1} \max \left[(\mu/\mu_u); 10^{0.2(m_b-m)} \right] \quad (\text{A.2})$$

where π , μ and m are respectively the parallax, proper motion and apparent magnitude of a particular white dwarf of the sample. The lower and upper proper-motion survey limits are denoted by μ_l and μ_u , while the faintest and the brightest apparent magnitude survey limits are denoted by m_f and m_b , respectively. Secondly, we can now estimate the maximum volume V_{\max} over which each white dwarf contributes as

$$V_{\max} = (4/3)\pi\beta(r_{\max}^3 - r_{\min}^3) \quad (\text{A.3})$$

where β is the fraction of the sky covered by the sample. We note that since V_{\max} is the volume defined by the maximum and minimum distance for which a particular white dwarf would still appear as a member of the selected sample, it also provides the likelihood of detecting this particular white dwarf. Consequently, its contribution to the space density will be the inverse of this volume, $1/V_{\max}$.

Until now we have assumed that the spatial distribution of a given population does not depend on the distance, and hence that its luminosity function — that is, its space density — is not affected by the presence of gradients in the spatial distribution. However, for most Galactic samples this is not true, as the density of disk stars decreases rapidly as we move away from the Galactic plane. Therefore, the effects of the Galactic scale height law need to be taken into account. This can be done modifying conveniently the expression for the maximum volume in the following way:

$$V_{\max} = (4/3)\pi\beta(r_{\max}^3 - r_{\min}^3) \exp(-z/H) \quad (\text{A.4})$$

where H is the Galactic disk scale height and z is the perpendicular distance from the Galactic plane.

With all these considerations we can proceed to compute the luminosity function of any white dwarf population simply adding the individual values of $1/V_{\max}$ for each star of the sample. This is done, obviously, for each luminosity bin, and as a result the distribution of white dwarfs as a function of the bolometric magnitude is obtained. Moreover, it can be shown that a sample can be considered complete when the average of the individual white dwarf volumes divided by its maximum value is just half unit, $\langle V/V_{\max} \rangle = 0.5$.

Finally, we would like to recall that, as previously mentioned, the $(1/V_{\max})$ method in an unbiased estimator for a complete sample. However, Takeuchi et al. (2000) have pointed out that the $(1/V_{\max})$ method is seriously affected when the input data is clustered, that is, when the input data is not homogeneously scattered. Consequently, $(1/V_{\max})$ method should only be used when homogeneity and completeness of the sample is guaranteed. For a comprehensive analysis of the $(1/V_{\max})$ method — as well as other and more sophisticated ones, such as the C^- method, the STY method or the Choloniewski method — their statistical significance and the effects of the measurement errors and other biases, we refer the reader to Geijo et al. (2006) and Torres et al. (2007).

Bibliography

- ABAZAJIAN, K. N., ADELMAN-McCARTHY, J. K., AGÜEROS, M. A., ALLAM, S. S., ALLENDE PRIETO, C. ET AL., 2009. The Seventh Data Release of the Sloan Digital Sky Survey. *ApJS*, **182**, 543–558.
- ABRIKOSOV, A. A., 1960. Nekotorye svoistva sil no szhatogo veshchestva. *ZhETF*, **39**, 1797–1805.
- ADAMS, F. C. & LAUGHLIN, G., 1996. Implications of White Dwarf Galactic Halos. *ApJ*, **468**, 586–+.
- ALCOCK, C., ALLSMAN, R. A., ALVES, D., AXELROD, T. S., BECKER, A. C. ET AL., 1997. The MACHO Project Large Magellanic Cloud Microlensing Results from the First Two Years and the Nature of the Galactic Dark Halo. *ApJ*, **486**, 697–+.
- ALCOCK, C., ALLSMAN, R. A., ALVES, D., AXELROD, T. S., BENNETT, D. P., COOK, K. H., FREEMAN, K. C., GRIEST, K., GUERN, J., LEHNER, M. J., MARSHALL, S. L., PETERSON, B. A., PRATT, M. R., QUINN, P. J., RODGERS, A. W., STUBBS, C. W. & SUTHERLAND, W., 1995. First Observation of Parallax in a Gravitational Microlensing Event. *ApJ*, **454**, L125+.
- ALCOCK, C., ALLSMAN, R. A., ALVES, D. R., AXELROD, T. S., BECKER, A. C. ET AL., 2000. The MACHO Project: Microlensing Results from 5.7 Years of Large Magellanic Cloud Observations. *ApJ*, **542**, 281–307.
- ALTHAUS, L. G., GARCÍA-BERRO, E., ISERN, J., CÓRSICO, A. H. & ROHRMANN, R. D., 2007. The age and colors of massive white dwarf stars. *A&A*, **465**, 249–255.
- ALTHAUS, L. G., PANEI, J. A., MILLER BERTOLAMI, M. M., GARCÍA-BERRO, E., CÓRSICO, A. H., ROMERO, A. D., KEPLER, S. O. & ROHRMANN, R. D., 2009. New Evolutionary Sequences for Hot H-Deficient White Dwarfs on the Basis of a Full Account of Progenitor Evolution. *ApJ*, **704**, 1605–1615.
- ALTHAUS, L. G., SERENELLI, A. M. & BENVENUTO, O. G., 2001. Diffusion and the occurrence of hydrogen-shell flashes in helium white dwarf stars. *MNRAS*, **323**, 471–483.

- BARAFFE, I., CHABRIER, G., ALLARD, F. & HAUSCHILDT, P. H., 1998. Evolutionary models for solar metallicity low-mass stars: mass-magnitude relationships and color-magnitude diagrams. *A&A*, **337**, 403–412.
- BARSTOW, M. A., BURLEIGH, M. R., BANNISTER, N. P., HOLBERG, J. B., HUBENY, I., BRUHWEILER, F. C. & NAPIWOTZKI, R., 2001. Heavy Elements in DA White Dwarfs. In J. L. Provencal, H. L. Shipman, J. MacDonald & S. Goodchild, eds., *12th European Workshop on White Dwarfs*, vol. 226 of *Astronomical Society of the Pacific Conference Series*, 128.
- BARSTOW, M. A., FLEMING, T. A., DIAMOND, C. J., FINLEY, D. S., SANSOM, A. E., ROSEN, S. R., KOESTER, D., HOLBERG, M. C., MARSH, J. B. & KIDDER, K., 1993. ROSAT Studies of the Composition and Structure of DA White Dwarf Atmospheres. *MNRAS*, **264**, 16.
- BARSTOW, M. A., GOOD, S. A., HOLBERG, J. B., HUBENY, I., BANNISTER, N. P., BRUHWEILER, F. C., BURLEIGH, M. R. & NAPIWOTZKI, R., 2003. Heavy-element abundance patterns in hot DA white dwarfs. *MNRAS*, **341**, 870–890.
- BECKER, A. C., REST, A., STUBBS, C., MIKNAITIS, G. A., MICELI, A. ET AL., 2005. The SuperMACHO Microlensing Survey. In Y. Mellier & G. Meylan, ed., *Gravitational Lensing Impact on Cosmology*, vol. 225 of *IAU Symposium*, 357–362.
- BELCZYNSKI, K., BULIK, T. & RUDAK, B., 2002. Study of Gamma-Ray Burst Binary Progenitors. *ApJ*, **571**, 394–412.
- BELOKUROV, V., EVANS, N. W. & DU, Y. L., 2003. Light-curve classification in massive variability surveys - I. Microlensing. *MNRAS*, **341**, 1373–1384.
- BELOKUROV, V., EVANS, N. W. & LE DU, Y., 2004. Light-curve classification in massive variability surveys - II. Transients towards the Large Magellanic Cloud. *MNRAS*, **352**, 233–242.
- BENNETT, C. L., HALPERN, M., HINSHAW, G., JAROSIK, N., KOGUT, A. ET AL., 2003. First-Year Wilkinson Microwave Anisotropy Probe (WMAP) Observations: Preliminary Maps and Basic Results. *ApJS*, **148**, 1–27.
- BENNETT, D. P., 2005. Large Magellanic Cloud Microlensing Optical Depth with Imperfect Event Selection. *ApJ*, **633**, 906–913.
- BENVENUTO, O. G. & ALTHAUS, L. G., 1997. DB white dwarf evolution in the frame of the full spectrum turbulence theory. *MNRAS*, **288**, 1004–1014.
- BERGERON, P., GIANNINAS, A. & BOUDREAULT, S., 2007. The Mass Distribution of White Dwarfs: An Unwavering Obsession. In R. Napiwotzki & M. R. Burleigh, eds., *15th European Workshop on White Dwarfs*, vol. 372 of *Astronomical Society of the Pacific Conference Series*, 29.

- BERGERON, P. & LEGGETT, S. K., 2002. Model Atmosphere Analysis of Two Very Cool White Dwarfs. *ApJ*, **580**, 1070–1076.
- BERGERON, P., LEGGETT, S. K. & RUIZ, M. T., 2001. BVRIJHK photometry of cool white dwarfs (Bergeron+, 2001). *VizieR Online Data Catalog*, **2133**, 30413–+.
- BERGERON, P., WESEMAEL, F. & BEAUCHAMP, A., 1995. Photometric Calibration of Hydrogen- and Helium-Rich White Dwarf Models. *Pub. Ast. Soc. Pacific*, **107**, 1047–+.
- BERGERON, P., WESEMAEL, F., DUFOUR, P., BEAUCHAMP, A., HUNTER, C., SAFFER, R. A., GIANNINAS, A., RUIZ, M. T., LIMOGES, M.-M., DUFOUR, P., FONTAINE, G. & LIEBERT, J., 2011. A Comprehensive Spectroscopic Analysis of DB White Dwarfs. *ApJ*, **737**, 28.
- BESLA, G., HERNQUIST, L. & LOEB, A., 2013. The origin of the microlensing events observed towards the LMC and the stellar counterpart of the Magellanic stream. *MNRAS*, **428**, 2342–2365.
- BESSEL, F. W., 1844. On the variations of the proper motions of Procyon and Sirius. *MNRAS*, **6**, 136–141.
- BINNEY, J. & TREMAINE, H., 1987. Book Review: Galactic dynamics. / Princeton U Press, 1988. *Nature*, **326**, 219–+.
- BOCHANSKI, J. J., HAWLEY, S. L. & WEST, A. A., 2011. The Sloan Digital Sky Survey Data Release 7 Spectroscopic M Dwarf Catalog. II. Statistical Parallax Analysis. *AJ*, **141**, 98.
- BOCHANSKI, JR., J. J., 2008. *M dwarfs in the local Milky Way: The field low-mass stellar luminosity and mass functions*. Ph.D. thesis, University of Washington.
- CALCHI NOVATI, S., DE LUCA, F., JETZER, P. & SCARPETTA, G., 2006. Microlensing towards the Large Magellanic Cloud: a study of the LMC halo contribution. *A&A*, **459**, 407–414.
- CAMACHO, J., TORRES, S., ISERN, J., ALTHAUS, L. G. & GARCÍA-BERRO, E., 2007. The contribution of oxygen-neon white dwarfs to the MACHO content of the Galactic halo. *A&A*, **471**, 151–158.
- CANAL, R., ISERN, J. & RUIZ-LAPUENTE, P., 1997. Further Constraints on White Dwarf Galactic Halos. *ApJ*, **488**, L35+.
- CAROLLO, D., BEERS, T. C., CHIBA, M., NORRIS, J. E., FREEMAN, K. C., LEE, Y. S., IVEZIĆ, Ž., ROCKOSI, C. M. & YANNY, B., 2010. Structure and

- Kinematics of the Stellar Halos and Thick Disks of the Milky Way Based on Calibration Stars from Sloan Digital Sky Survey DR7. *ApJ*, **712**, 692–727.
- CATALÁN, S., ISERN, J., GARCÍA-BERRO, E. & RIBAS, I., 2008a. The initial-final mass relationship of white dwarfs revisited: effect on the luminosity function and mass distribution. *MNRAS*, **387**, 1693–1706.
- CATALÁN, S., ISERN, J., GARCÍA-BERRO, E., RIBAS, I., ALLENDE PRIETO, C. & BONANOS, A. Z., 2008b. The initial-final mass relationship from white dwarfs in common proper motion pairs. *A&A*, **477**, 213–221.
- CHABRIER, G., 2004. The Glow of Primordial Remnants. *ApJ*, **611**, 315–322.
- CHABRIER, G., SEGRETAIN, L. & M'ERA, D., 1996. Contribution of Brown Dwarfs and White Dwarfs to Recent Microlensing Observations and to the Halo Mass Budget. *ApJ*, **468**, L21+.
- CHANDRASEKHAR, S., 1931. The Maximum Mass of Ideal White Dwarfs. *ApJ*, **74**, 81.
- CHANDRASEKHAR, S., 1933. The equilibrium of distorted polytropes. I. The rotational problem. *MNRAS*, **93**, 390–406.
- CHARLOT, S. & SILK, J., 1995. Signatures of white dwarf galaxy halos. *ApJ*, **445**, 124–132.
- CHAYER, P. & DUPUIS, J., 2010. Effect of Radiative Levitation on Calculations of Accretion Rates in White Dwarfs. In K. Werner & T. Rauch, eds., *American Institute of Physics Conference Series*, vol. 1273 of *American Institute of Physics Conference Series*, 394–399.
- CHAYER, P., FONTAINE, G. & WESEMAEL, F., 1995a. Radiative Levitation in Hot White Dwarfs: Equilibrium Theory. *ApJS*, **99**, 189.
- CHAYER, P., LEBLANC, F., FONTAINE, G., WESEMAEL, F., MICHAUD, G. & VENNES, S., 1994. On the predicted abundances of iron and nickel supported by radiative levitation in the atmospheres of hot DA white dwarfs. *ApJ*, **436**, L161–L164.
- CHAYER, P., VENNES, S., PRADHAN, A. K., THEJLL, P., BEAUCHAMP, A., FONTAINE, G. & WESEMAEL, F., 1995b. Improved Calculations of the Equilibrium Abundances of Heavy Elements Supported by Radiative Levitation in the Atmospheres of Hot DA White Dwarfs. *ApJ*, **454**, 429.
- CHERNICK, M., 2007. *Bootstrap methods: A guide for practitioners and researchers*, vol. 619. Wiley-Interscience.

- CHIBA, M. & BEERS, T. C., 2000. Kinematics of Metal-poor Stars in the Galaxy. III. Formation of the Stellar Halo and Thick Disk as Revealed from a Large Sample of Nonkinematically Selected Stars. *AJ*, **119**, 2843–2865.
- CHOLONIEWSKI, J., 1986. New method for the determination of the luminosity function of galaxies. *MNRAS*, **223**, 1–9.
- CUTRI, R. M., SKRUTSKIE, M. F., VAN DYK, S., BEICHMAN, C. A., CARPENTER, J. M. ET AL., 2003. 2MASS All-Sky Catalog of Point Sources (Cutri+ 2003). *VizieR Online Data Catalog*, **2246**, 0+.
- DAVIS, P. J., KOLB, U. & WILLEMS, B., 2010. A comprehensive population synthesis study of post-common envelope binaries. *MNRAS*, **403**, 179–195.
- DE GENNARO, S., VON HIPPEL, T., WINGET, D. E., KEPLER, S. O., NITTA, A., KOESTER, D. & ALTHAUS, L., 2008. White Dwarf Luminosity and Mass Functions from Sloan Digital Sky Survey Spectra. *AJ*, **135**, 1–9.
- DE KOOL, M., 1990. Common envelope evolution and double cores of planetary nebulae. *Astrophys. J.*, **358**, 189–195.
- DE KOOL, M., 1992. Statistics of cataclysmic variable formation. *A&A*, **261**, 188–202.
- DE MARCO, O., PASSY, J.-C., MOE, M., HERWIG, F., MAC LOW, M.-M. & PAXTON, B., 2011. On the α formalism for the common envelope interaction. *MNRAS*, **411**, 2277–2292.
- DE MARTINO, D. & SILVOTTI, R., 2004. The role of Eddington in variability studies of accreting white dwarfs. In F. Favata, S. Aigrain & A. Wilson, eds., *Stellar Structure and Habitable Planet Finding*, vol. 538 of *ESA Special Publication*, 305–308.
- DEHNEN, W. & BINNEY, J. J., 1998. Local stellar kinematics from HIPPARCOS data. *MNRAS*, **298**, 387–394.
- DEUTSCH, A. J., 1956. The Circumstellar Envelope of Alpha Herculis. *ApJ*, **123**, 210.
- DEWI, J. D. M. & TAURIS, T. M., 2000. On the energy equation and efficiency parameter of the common envelope evolution. *A&A*, **360**, 1043–1051.
- DI STEFANO, R., 2011. Transits and Lensing by Compact Objects in the Kepler Field: Disrupted Stars Orbiting Blue Stragglers. *AJ*, **141**, 142.
- DI STEFANO, R., HOWELL, S. B. & KAWALER, S. D., 2010. A Search for Asteroids, Moons, and Rings Orbiting White Dwarfs. *ApJ*, **712**, 142–146.

- DREIZLER, S. & WERNER, K., 1996. Spectral analysis of hot helium-rich white dwarfs. *A&A*, **314**, 217–232.
- DUFOUR, P., FONTAINE, G., LIEBERT, J., SCHMIDT, G. D. & BEHARA, N., 2008. Hot DQ White Dwarfs: Something Different. *ApJ*, **683**, 978–989.
- DUFOUR, P., KILIC, M., FONTAINE, G., BERGERON, P., LACHAPELLE, F.-R., KLEINMAN, S. J. & LEGGETT, S. K., 2010. The Discovery of the Most Metal-rich White Dwarf: Composition of a Tidally Disrupted Extrasolar Dwarf Planet. *ApJ*, **719**, 803–809.
- DUFOUR, P., LIEBERT, J., FONTAINE, G. & BEHARA, N., 2007. White dwarf stars with carbon atmospheres. *Nature*, **450**, 522–524.
- DUPUIS, J., CHAYER, P. & HÉNAULT-BRUNET, V., 2010a. Applying the accretion-diffusion model to a sample of DAZ without IR excess. In K. Werner & T. Rauch, eds., *American Institute of Physics Conference Series*, vol. 1273 of *American Institute of Physics Conference Series*, 412–417.
- DUPUIS, J., CHAYER, P., HÉNAULT-BRUNET, V., VENNES, S. & KRUK, J. W., 2010b. Radiative Accelerations and Equilibrium Abundances of Metals for DA White Dwarfs below 25,000K. In *American Astronomical Society Meeting Abstracts*, vol. 42 of *Bulletin of the American Astronomical Society*, 452.05.
- EGGLETON, P. P., 1983. Approximations to the radii of Roche lobes. *Astrophys. J.*, **268**, 368–+.
- EISENSTEIN, D. J., LIEBERT, J., HARRIS, H. C., KLEINMAN, S. J., NITTA, A., SILVESTRI, N., ANDERSON, S. A., BARENTINE, J. C., BREWINGTON, H. J., BRINKMANN, J., HARVANEK, M., KRZESIŃSKI, J., NEILSEN, JR., E. H., LONG, D., SCHNEIDER, D. P. & SNEDDEN, S. A., 2006a. A Catalog of Spectroscopically Confirmed White Dwarfs from the Sloan Digital Sky Survey Data Release 4. *ApJS*, **167**, 40–58.
- EISENSTEIN, D. J., LIEBERT, J., HARRIS, H. C., KLEINMAN, S. J., NITTA, A., SILVESTRI, N., ANDERSON, S. A., BARENTINE, J. C., BREWINGTON, H. J., BRINKMANN, J., HARVANEK, M., KRZESINSKI, J., NEILSEN, E. H. J., LONG, D., SCHNEIDER, D. P. & SNEDDEN, S. A., 2008. SDSS4 confirmed white dwarfs catalog (Eisenstein+, 2006). *VizieR Online Data Catalog*, **2167**, 70040–+.
- EISENSTEIN, D. J., LIEBERT, J., KOESTER, D., KLEINMANN, S. J., NITTA, A., SMITH, P. S., BARENTINE, J. C., BREWINGTON, H. J., BRINKMANN, J., HARVANEK, M., KRZESIŃSKI, J., NEILSEN, J. E. H., LONG, D., SCHNEIDER, D. P. & SNEDDEN, S. A., 2006b. Hot DB White Dwarfs from the Sloan Digital Sky Survey. *AJ*, **132**, 676–691.

- FARIHI, J., BARSTOW, M. A., REDFIELD, S., DUFOUR, P. & HAMBLBY, N. C., 2010. Rocky planetesimals as the origin of metals in DZ stars. *MNRAS*, **404**, 2123–2135.
- FELTEN, J. E., 1976. On Schmidt’s V_m estimator and other estimators of luminosity functions. *ApJ*, **207**, 700–709.
- FIGUERAS, F., GARCÍA-BERRO, E., TORRA, J., JORDI, C., LURI, X., TORRES, S. & CHEN, B., 1999. GAIA Science Output: White Dwarfs. *Baltic Astronomy*, **8**, 291–300.
- FINLEY, D. S., KOESTER, D. & BASRI, G., 1997. The Temperature Scale and Mass Distribution of Hot DA White Dwarfs. *ApJ*, **488**, 375–+.
- FLEMING, T. A., LIEBERT, J. & GREEN, R. F., 1986. The luminosity function of DA white dwarfs. *ApJ*, **308**, 176–189.
- FLYNN, C., GOULD, A. & BAHCALL, J. N., 1996. Hubble Deep Field Constraint on Baryonic Dark Matter. *ApJ*, **466**, L55.
- FLYNN, C., HOLMBERG, J., PORTINARI, L., FUCHS, B. & JAHREISS, H., 2006. On the mass-to-light ratio of the local Galactic disc and the optical luminosity of the Galaxy. *MNRAS*, **372**, 1149–1160.
- FLYNN, C., SOMMER-LARSEN, J., FUCHS, B., GRAFF, D. S. & SALIM, S., 2001. A search for nearby counterparts to the moving objects in the Hubble Deep Field. *MNRAS*, **322**, 553–560.
- FONTAINE, G., BRASSARD, P. & DUFOUR, P., 2008. Might carbon-atmosphere white dwarfs harbour a new type of pulsating star? *A&A*, **483**, L1–L4.
- FONTAINE, G., WESEMAEL, F., VENNES, S. & PELLETIER, C., 1987. The Case for Thin Hydrogen Layers in Hot DA White Dwarfs. In *Bulletin of the American Astronomical Society*, vol. 19 of *Bulletin of the American Astronomical Society*, 1115.
- FRIEMAN, J. A., BASSETT, B., BECKER, A., CHOI, C., CINABRO, D. ET AL., 2008. The Sloan Digital Sky Survey-II Supernova Survey: Technical Summary. *AJ*, **135**, 338–347.
- GÄNSICKE, B. T., KOESTER, D., GIRVEN, J., MARSH, T. R. & STEEGHS, D., 2010. Two White Dwarfs with Oxygen-Rich Atmospheres. *Science*, **327**, 188–.
- GARCIA-BERRO, E., HERNANZ, M., ISERN, J. & MOCHKOVITCH, R., 1988a. Properties of high-density binary mixtures and the age of the universe from white dwarf stars. *Nature*, **333**, 642–644.

- GARCIA-BERRO, E., HERNANZ, M., ISERN, J. & MOCHKOVITCH, R., 1995. The rate of change of the gravitational constant and the cooling of white dwarfs. *MNRAS*, **277**, 801–810.
- GARCIA-BERRO, E., HERNANZ, M., MOCHKOVITCH, R. & ISERN, J., 1988b. Theoretical white-dwarf luminosity functions for two phase diagrams of the carbon-oxygen dense plasma. *A&A*, **193**, 141–147.
- GARCÍA-BERRO, E., TORRES, S., ISERN, J. & BURKERT, A., 1999. Monte Carlo simulations of the disc white dwarf population. *MNRAS*, **302**, 173–188.
- GARCÍA-BERRO, E., TORRES, S., ISERN, J. & BURKERT, A., 2004. Monte Carlo simulations of the halo white dwarf population. *A&A*, **418**, 53–65.
- GATES, E., GYUK, G., HARRIS, H. C., SUBBARAO, M., ANDERSON, S., KLEINMAN, S. J., LIEBERT, J., BREWINGTON, H., BRINKMANN, J., HARVANEK, M., KRZESINSKI, J., LAMB, D. Q., LONG, D., NEILSEN, JR., E. H., NEWMAN, P. R., NITTA, A. & SNEDDEN, S. A., 2004. Discovery of New Ultracool White Dwarfs in the Sloan Digital Sky Survey. *ApJ*, **612**, L129–L132.
- GEIJO, E. M., TORRES, S., ISERN, J. & GARCÍA-BERRO, E., 2006. The white dwarf luminosity function - I. Statistical errors and alternatives. *MNRAS*, **369**, 1654–1666.
- GIAMMICHELE, N., BERGERON, P. & DUFOUR, P., 2012. Know Your Neighborhood: A Detailed Model Atmosphere Analysis of Nearby White Dwarfs. *ApJS*, **199**, 29.
- GIANNINAS, A., BERGERON, P. & RUIZ, M. T., 2011. A Spectroscopic Survey and Analysis of Bright, Hydrogen-rich White Dwarfs. *ApJ*, **743**, 138.
- GIBSON, B. K. & MOULD, J. R., 1997. The Chemical Residue of a White Dwarf-dominated Galactic Halo. *ApJ*, **482**, 98.
- GILMORE, G., WYSE, R. F. G. & JONES, J. B., 1995. A determination of the thick disk chemical abundance distribution: Implications for galaxy evolution. *AJ*, **109**, 1095–1111.
- GOLDMAN, B., AFONSO, C., ALARD, C., ALBERT, J.-N., AMADON, A. ET AL., 2002. EROS 2 proper motion survey: Constraints on the halo white dwarfs. *A&A*, **389**, L69–L73.
- GRAFF, D. S., LAUGHLIN, G. & FREESE, K., 1998. MACHOs, White Dwarfs, and the Age of the Universe. *ApJ*, **499**, 7.
- GREEN, R. F., SCHMIDT, M. & LIEBERT, J., 1986. The Palomar-Green catalog of ultraviolet-excess stellar objects. *ApJS*, **61**, 305–352.

- GRIEST, K., 1991. Galactic microlensing as a method of detecting massive compact halo objects. *ApJ*, **366**, 412–421.
- GYUK, G., DALAL, N. & GRIEST, K., 2000. Self-lensing Models of the Large Magellanic Cloud. *ApJ*, **535**, 90–103.
- GYUK, G. & GATES, E., 1999. Large Magellanic Cloud microlensing and very thick discs. *MNRAS*, **304**, 281–287.
- HAKKILA, J., MYERS, J. M., STIDHAM, B. J. & HARTMANN, D. H., 1997. A Computerized Model of Large-Scale Visual Interstellar Extinction. *AJ*, **114**, 2043.
- HAMBLY, N. C., IRWIN, M. J. & MACGILLIVRAY, H. T., 2001. The Super-COSMOS Sky Survey - II. Image detection, parametrization, classification and photometry. *MNRAS*, **326**, 1295–1314.
- HAN, Z., PODSIADLOWSKI, P. & EGGLETON, P. P., 1995. The formation of bipolar planetary nebulae and close white dwarf binaries. *MNRAS*, **272**, 800–820.
- HANSEN, B. M. S., 1998. Old and blue white-dwarf stars as a detectable source of microlensing events. *Nature*, **394**, 860–862.
- HANSEN, B. M. S. & LIEBERT, J., 2003. Cool White Dwarfs. *ARA&A*, **41**, 465–515.
- HARRIS, H. C., MUNN, J. A., KILIC, M., LIEBERT, J., WILLIAMS, K. A. ET AL., 2006. The White Dwarf Luminosity Function from Sloan Digital Sky Survey Imaging Data. *AJ*, **131**, 571–581.
- HEGGIE, D. C., 1975. Binary evolution in stellar dynamics. *Month. Not. Roy. Astron. Soc.*, **173**, 729–787.
- HELLER, R., HOMEIER, D., DREIZLER, S. & ØSTENSEN, R., 2009. Spectral analysis of 636 white dwarf-M star binaries from the sloan digital sky survey. *A&A*, **496**, 191–205.
- HERSCHEL, W., 1786. Catalogue of One Thousand New Nebulae and Clusters of Stars. by William Herschel, LL.D. F. R. S. *Royal Society of London Philosophical Transactions Series I*, **76**, 457–499.
- HOLBERG, J. B., BARSTOW, M. A. & SION, E. M., 1998. A High-Dispersion Spectroscopic Survey of the Hot White Dwarfs: The IUE NEWSIPS SWP Echelle Data Set. *ApJS*, **119**, 207–238.
- HOLBERG, J. B., SION, E. M., OSWALT, T., MCCOOK, G. P., FORAN, S. & SUBASAVAGE, J. P., 2008. A New Look at the Local White Dwarf Population. *AJ*, **135**, 1225–1238.

- HOLMBERG, J. & FLYNN, C., 2000. The local density of matter mapped by Hipparcos. *Month. Not. Roy. Astron. Soc.*, **313**, 209–216.
- HOLOPAINEN, J., FLYNN, C., KNEBE, A., GILL, S. P. & GIBSON, B. K., 2006. Microlensing in dark matter haloes. *MNRAS*, **368**, 1209–1222.
- HOLTZMAN, J. A., BURROWS, C. J., CASERTANO, S., HESTER, J. J., TRAUGER, J. T., WATSON, A. M. & WORTHEY, G., 1995. The Photometric Performance and Calibration of WFPC2. *Pub. Ast. Soc. Pacific*, **107**, 1065–+.
- HUFNAGEL, B., 1995. Old Open Clusters as Probes of Stellar and Galactic Disk Evolution. *Pub. Ast. Soc. Pacific*, **107**, 1016.
- HÜGELMEYER, S. D., DREIZLER, S., HOMEIER, D., KRZESIŃSKI, J., WERNER, K., NITTA, A. & KLEINMAN, S. J., 2006. Spectral analyses of eighteen hot H-deficient (pre-) white dwarfs from the Sloan Digital Sky Survey Data Release 4. *A&A*, **454**, 617–624.
- HURLEY, J. R., TOUT, C. A. & POLS, O. R., 2002. Evolution of binary stars and the effect of tides on binary populations. *Month. Not. Roy. Astron. Soc.*, **329**, 897–928.
- IBATA, R. A., RICHER, H. B., GILLILAND, R. L. & SCOTT, D., 1999. Faint, Moving Objects in the Hubble Deep Field: Components of the Dark Halo? *ApJ*, **524**, L95–L97.
- IBEN, JR., I. & LAUGHLIN, G., 1989. A study of the white dwarf luminosity function. *ApJ*, **341**, 312–326.
- IBEN, JR., I. & LIVIO, M., 1993. Common envelopes in binary star evolution. *Pub. Ast. Soc. Pacific*, **105**, 1373–1406.
- ISERN, J., GARCÍA-BERRO, E., ALTHAUS, L. G. & CÓRSICO, A. H., 2010. Axions and the pulsation periods of variable white dwarfs revisited. *A&A*, **512**, A86.
- ISERN, J., GARCIA-BERRO, E., HERNANZ, M., MOCHKOVITCH, R. & TORRES, S., 1998. The Halo White Dwarf Population. *ApJ*, **503**, 239–+.
- IVANOVA, N., 2011. Common Envelope: The Progress and the Pitfalls. In L. Schmidtbreick, M. R. Schreiber & C. Tappert, eds., *Evolution of Compact Binaries*, vol. 447 of *Astronomical Society of the Pacific Conference Series*, 91.
- JAMES, F., 1990. A review of pseudorandom number generators. *Computer Physics Communications*, **60**, 329–344.
- JEANS, J. H., 1922. The motions of stars in a Kapteyn universe. *MNRAS*, **82**, 122–132.

- JORDI, K., GREBEL, E. K. & AMMON, K., 2006. Empirical color transformations between SDSS photometry and other photometric systems. *A&A*, **460**, 339–347.
- KAHN, S. M., WESEMAEL, F., LIEBERT, J., RAYMOND, J. C., STEINER, J. E. & SHIPMAN, H. L., 1984. Photospheric soft X-ray emission from hot DA white dwarfs. *ApJ*, **278**, 255–265.
- KALIRAI, J., 2006. Probing stellar evolution with open star clusters. *Bulletin of the Astronomical Society of India*, **34**, 141.
- KALLIVAYALIL, N., VAN DER MAREL, R. P., ALCOCK, C., AXELROD, T., COOK, K. H., DRAKE, A. J. & GEHA, M., 2006. The Proper Motion of the Large Magellanic Cloud Using HST. *ApJ*, **638**, 772–785.
- KAPTEYN, J. C., 1922. First Attempt at a Theory of the Arrangement and Motion of the Sidereal System. *ApJ*, **55**, 302.
- KEPLER, S. O., KLEINMAN, S. J., NITTA, A., KOESTER, D., CASTANHEIRA, B. G., GIOVANNINI, O., COSTA, A. F. M. & ALTHAUS, L., 2007. White dwarf mass distribution in the SDSS. *MNRAS*, **375**, 1315–1324.
- KERINS, E. & EVANS, N. W., 1998. Microlensing Halo Models with Abundant Brown Dwarfs. *ApJ*, **503**, L75+.
- KILIC, M., BROWN, W. R. & MCLEOD, B., 2010. A Spitzer Search for Substellar Companions to Low-Mass White Dwarfs. *ApJ*, **708**, 411–418.
- KILIC, M., KOWALSKI, P. M. & VON HIPPEL, T., 2009. A Near-Infrared Spectroscopic Survey of Cool White Dwarfs in the Sloan Digital Sky Survey. *AJ*, **138**, 102–109.
- KILIC, M., MENDEZ, R. A., VON HIPPEL, T. & WINGET, D. E., 2005. Faint Blue Objects in the Hubble Deep Field-South Revealed: White Dwarfs, Subdwarfs, and Quasars. *ApJ*, **633**, 1126–1141.
- KILIC, M., MUNN, J. A., HARRIS, H. C., LIEBERT, J., VON HIPPEL, T., WILLIAMS, K. A., METCALFE, T. S., WINGET, D. E. & LEVINE, S. E., 2006. Cool White Dwarfs in the Sloan Digital Sky Survey. *AJ*, **131**, 582–599.
- KIRZHNITS, D. A., 1958. Correlation energy of a non-ideal Fermi gas. *Zh. Eksp. Teor. Fiz*, **35**, 1198–1208 [Engl. transl.: 1960, Soviet Phys. JETP 8, 1081].
- KITAMURA, M., 1959. On the Close Binary Stars of W Ursae Majoris Type. *"Publ. Astron. Soc. Japan"*, **11**, 216.

- KLEINMAN, S. J., HARRIS, H. C., EISENSTEIN, D. J., LIEBERT, J., NITTA, A. ET AL., 2004. A Catalog of Spectroscopically Identified White Dwarf Stars in the First Data Release of the Sloan Digital Sky Survey. *ApJ*, **607**, 426–444.
- KLYPIN, A., ZHAO, H. & SOMERVILLE, R. S., 2002. Λ CDM-based Models for the Milky Way and M31. I. Dynamical Models. *ApJ*, **573**, 597–613.
- KOCHANEK, C. S., SCHNEIDER, P. & WAMBSGANSS, J., 2004. Gravitational lensing: strong, weak and micro. In G. Meylan, P. Jetzer & P.-V. B. North, eds., *Proceedings of the 33rd Saas-Fee Advanced Course: Gravitational Lensing: Strong, Weak and Micro*, D7.
- KOESTER, D., 1989. Can the EXOSAT observations of DA white dwarfs be explained by layered atmospheric structures? *ApJ*, **342**, 999–1002.
- KOESTER, D., NAPIWOTZKI, R., VOSS, B., HOMEIER, D. & REIMERS, D., 2005. HS 0146+1847 - a DAZB white dwarf of very unusual composition. *A&A*, **439**, 317–321.
- KOESTER, D. & WILKEN, D., 2006. The accretion-diffusion scenario for metals in cool white dwarfs. *A&A*, **453**, 1051–1057.
- KOMATSU, E., SMITH, K. M., DUNKLEY, J., BENNETT, C. L., GOLD, B. ET AL., 2011. Seven-year Wilkinson Microwave Anisotropy Probe (WMAP) Observations: Cosmological Interpretation. *ApJS*, **192**, 18.
- KONDO, Y., 1984. International Ultraviolet Explorer Observatory. *Astronomical Herald*, **77**, 19–20.
- KOOPMANS, L., 2002. The Structure of Early-Type Galaxies from Lensing and Stellar Dynamics. In *KITP Program: The New Cosmology Confronts Observation: The Cosmic Microwave Background, Dark Matter, Dark Energy, and Brane Worlds*.
- KOWALSKI, K., REMBIELIŃSKI, J. & SMOLIŃSKI, K. A., 2007. Relativistic ideal Fermi gas at zero temperature and preferred frame. *Phys. Rev. D*, **76**(12), 127701.
- KOWALSKI, P. M. & SAUMON, D., 2006. Found: The Missing Blue Opacity in Atmosphere Models of Cool Hydrogen White Dwarfs. *ApJ*, **651**, L137–L140.
- KROUPA, P., 2001. On the variation of the initial mass function. *MNRAS*, **322**, 231–246.
- KROUPA, P., TOUT, C. A. & GILMORE, G., 1993. The distribution of low-mass stars in the Galactic disc. *Month. Not. Roy. Astron. Soc.*, **262**, 545–587.

- KUIPER, G. P., 1941. On the Interpretation of β Lyrae and Other Close Binaries. *ApJ*, **93**, 133.
- KWOK, S., 2000. Book Review: The origin and evolution of planetary nebulae / Cambridge U Press, 2000. *Irish Astronomical Journal*, **27**, 235.
- LARSON, D., DUNKLEY, J., HINSHAW, G., KOMATSU, E., NOLTA, M. R. ET AL., 2011. Seven-year Wilkinson Microwave Anisotropy Probe (WMAP) Observations: Power Spectra and WMAP-derived Parameters. *ApJS*, **192**, 16.
- LASSERRE, T., AFONSO, C., ALBERT, J. N., ANDERSEN, J., ANSARI, R. ET AL., 2000. Not enough stellar mass Machos in the Galactic halo. *A&A*, **355**, L39–L42.
- LAUGHLIN, G., BODENHEIMER, P. & ADAMS, F. C., 1997. The End of the Main Sequence. *ApJ*, **482**, 420.
- LI, N. & THAKAR, A. R., 2008. CasJobs and MyDB: A Batch Query Workbench. *Computing in Science and Engineering*, **10**, 18–.
- LIEBERT, J., BERGERON, P. & HOLBERG, J. B., 2005. The Formation Rate and Mass and Luminosity Functions of DA White Dwarfs from the Palomar Green Survey. *ApJS*, **156**, 47–68.
- LIEBERT, J., DAHN, C. C. & MONET, D. G., 1988. The luminosity function of white dwarfs. *ApJ*, **332**, 891–909.
- LIEBERT, J., DAHN, C. C. & MONET, D. G., 1989. The luminosity function of white dwarfs in the local disk and halo. In G. Wegner, ed., *IAU Colloq. 114: White Dwarfs*, vol. 328 of *Lecture Notes in Physics*, Berlin Springer Verlag, 15–23.
- LIEBERT, J., HARRIS, H. C., DAHN, C. C., SCHMIDT, G. D., KLEINMAN, S. J. ET AL., 2003. SDSS White Dwarfs with Spectra Showing Atomic Oxygen and/or Carbon Lines. *AJ*, **126**, 2521–2528.
- LIMOGES, M.-M. & BERGERON, P., 2010. A Spectroscopic Analysis of White Dwarfs in the Kiso Survey. *ApJ*, **714**, 1037–1051.
- LUCY, L. B., 1973. The Common Convective Envelope Model for W Ursae Majoris Systems and the Analysis of their Light Curves. *Ap&SS*, **22**, 381–392.
- LUCY, L. B., 2000. Hypothesis testing for meagre data sets. *MNRAS*, **318**, 92–100.
- MARSH, T. R., DHILLON, V. S. & DUCK, S. R., 1995. Low-Mass White Dwarfs Need Friends - Five New Double-Degenerate Close Binary Stars. *MNRAS*, **275**, 828.

- MESTEL, L., 1952. On the theory of white dwarf stars. I. The energy sources of white dwarfs. *MNRAS*, **112**, 583.
- METCALFE, T. S., 2005. Lessons for asteroseismology from white dwarf stars. *Journal of Astrophysics and Astronomy*, **26**, 273.
- MOLLERACH, S. & ROULET, E., 2002. *Gravitational lensing and microlensing*. World Scientific Publishing.
- MUNARI, U. & RENZINI, A., 1992. Are symbiotic stars the precursors of type IA supernovae? *ApJ*, **397**, L87–L90.
- MURAKI, Y., SUMI, T., ABE, F., BOND, I., CARTER, B. ET AL., 1999. Search for Machos by the MOA Collaboration. *Progress of Theoretical Physics Supplement*, **133**, 233–246.
- MYSZKA, J., SION, E. M., HOLBERG, J. B., OSWALT, T. D., MCCOOK, G. P. & WASATONIC, R., 2012. The Distribution of Spectroscopic Subtypes and Kinematics of White Dwarfs within 25 pc of the Sun. In *American Astronomical Society Meeting Abstracts*, vol. 220 of *American Astronomical Society Meeting Abstracts*, 430.02.
- NAVARRO, J. F., FRENK, C. S. & WHITE, S. D. M., 1997. A Universal Density Profile from Hierarchical Clustering. *ApJ*, **490**, 493–+.
- NEBOT GÓMEZ-MORÁN, A., GÄNSICKE, B. T., SCHREIBER, M. R., REBASSA-MANSERGAS, A., SCHWOPE, A. D. ET AL., 2011. Post common envelope binaries from SDSS. XII. The orbital period distribution. *A&A*, **536**, A43.
- NELEMANS, G. & TOUT, C. A., 2005. Reconstructing the evolution of white dwarf binaries: further evidence for an alternative algorithm for the outcome of the common-envelope phase in close binaries. *MNRAS*, **356**, 753–764.
- NELEMANS, G., VERBUNT, F., YUNGELSON, L. R. & PORTEGIES ZWART, S. F., 2000. Reconstructing the evolution of double helium white dwarfs: envelope loss without spiral-in. *A&A*, **360**, 1011–1018.
- NELEMANS, G., YUNGELSON, L. R., PORTEGIES ZWART, S. F. & VERBUNT, F., 2001. Population synthesis for double white dwarfs . I. Close detached systems. *Astron. & Astrophys.*, **365**, 491–507.
- NOGUCHI, T., MAEHARA, H. & KONDO, M., 1980. A search for ultraviolet-excess objects. *Annals of the Tokyo Astronomical Observatory*, **18**, 55–70.
- OORT, J. H., 1932. The force exerted by the stellar system in the direction perpendicular to the galactic plane and some related problems. *Bulletin of the Astronomical Institutes of the Netherlands*, **6**, 249.

- ÖPIK, E., 1915. Selective absorption of light in space, and the dynamics of the Universe [An analysis of the dynamics of the Galaxy, and determination of the dynamical density of matter in the galactic plane from vertical motions of stars] . *Bull. de la Soc. Astr. de Russie*, 150–158.
- OPPENHEIMER, B. R., HAMBLBY, N. C., DIGBY, A. P., HODGKIN, S. T. & SAUMON, D., 2001. Direct Detection of Galactic Halo Dark Matter. *Science*, **292**, 698–702.
- PACZYNSKI, B., 1976. Common Envelope Binaries. In P. Eggleton, S. Mitton & J. Whelan, eds., *Structure and Evolution of Close Binary Systems*, vol. 73 of *IAU Symposium*, 75.
- PACZYNSKI, B., 1986. Gravitational microlensing by the galactic halo. *ApJ*, **304**, 1–5.
- PASSY, J. C., DE MARCO, O., FRYER, C. L., HERWIG, F., DIEHL, S., OISHI, J. S., MAC LOW, M.-M., BRYAN, G. L. & ROCKEFELLER, G., 2012. Simulating the Common Envelope Phase of a Red Giant Using Smoothed-particle Hydrodynamics and Uniform-grid Codes. *ApJ*, **744**, 52.
- PELLETIER, C., FONTAINE, G., WESEMAEL, F., MICHAUD, G. & WEGNER, G., 1986. Carbon pollution in helium-rich white dwarf atmospheres Time-dependent calculations of the dredge-up process. *ApJ*, **307**, 242–252.
- PERLMUTTER, S., ALDERING, G., GOLDBABER, G., KNOP, R. A., NUGENT, P. ET AL., 1999. Measurements of Omega and Lambda from 42 High-Redshift Supernovae. *ApJ*, **517**, 565–586.
- PERRYMAN, M. A. C., LINDEGREN, L. & TURON, C., 1997. The Scientific Goals of the GAIA Mission. In R. M. Bonnet, E. Høg, P. L. Bernacca, L. Emiliani, A. Blaauw, C. Turon, J. Kovalevsky, L. Lindegren, H. Hassan, M. Bouffard, B. Strim, D. Heger, M. A. C. Perryman & L. Woltjer, eds., *Hipparcos - Venice '97*, vol. 402 of *ESA Special Publication*, 743–748.
- POLITANO, M. & WEILER, K. P., 2007. Population Synthesis Studies of Close Binary Systems Using a Variable Common Envelope Efficiency Parameter. I. Dependence on Secondary Mass. *ApJ*, **665**, 663–679.
- POLS, O. R., SCHRÖDER, K.-P., HURLEY, J. R., TOUT, C. A. & EGGLETON, P. P., 1998. Stellar evolution models for $Z = 0.0001$ to 0.03. *MNRAS*, **298**, 525–536.
- PRESS, W. H., FLANNERY, B. P. & TEUKOLSKY, S. A., 1986. *Numerical recipes. The art of scientific computing*. Cambridge University Press.

- RAHVAR, S., 2005. Microlensing by halo MACHOs with a spatially varying mass function. *MNRAS*, **356**, 1127–1132.
- RAUCH, T., RINGAT, E. & WERNER, K., 2010. Spectral Analyses Of The Hottest White Dwarfs: Grids Of Spectral Energy Distributions For Extremely Hot, Compact Stars In The Framework Of The Virtual Observatory. *ArXiv e-prints*.
- REBASSA-MANSERGAS, A., AGURTO-GANGAS, C., SCHREIBER, M. R., GÄNSICKE, B. T. & KOESTER, D., 2013. White dwarf main-sequence binaries from SDSS DR 8: unveiling the cool white dwarf population. *MNRAS*, **433**, 3398–3410.
- REBASSA-MANSERGAS, A., GAENSICKE, B. T., SCHREIBER, M. R., KOESTER, D. & RODRIGUEZ-GIL, P., 2010. Post-common envelope binaries from SDSS - VII: A catalogue of white dwarf-main sequence binaries. *MNRAS*, **406**, 620–640.
- REBASSA-MANSERGAS, A., GÄNSICKE, B. T., RODRÍGUEZ-GIL, P., SCHREIBER, M. R. & KOESTER, D., 2007. Post-common-envelope binaries from SDSS - I. 101 white dwarf main-sequence binaries with multiple Sloan Digital Sky Survey spectroscopy. *MNRAS*, **382**, 1377–1393.
- REBASSA-MANSERGAS, A., GÄNSICKE, B. T., SCHREIBER, M. R., SOUTHWORTH, J., SCHWOPE, A. D., NEBOT GOMEZ-MORAN, A., AUNGWEROJWIT, A., RODRÍGUEZ-GIL, P., KARAMANAVIS, V., KRUMPE, M., TREMOU, E., SCHWARZ, R., STAUDE, A. & VOGEL, J., 2008. Post-common envelope binaries from SDSS - III. Seven new orbital periods. *MNRAS*, **390**, 1635–1646.
- REBASSA-MANSERGAS, A., NEBOT GÓMEZ-MORÁN, A., SCHREIBER, M. R., GÄNSICKE, B. T., SCHWOPE, A., GALLARDO, J. & KOESTER, D., 2012. Post-common envelope binaries from SDSS - XIV. The DR7 white dwarf-main-sequence binary catalogue. *MNRAS*, **419**, 806–816.
- REBASSA-MANSERGAS, A., NEBOT GÓMEZ-MORÁN, A., SCHREIBER, M. R., GIRVEN, J. & GÄNSICKE, B. T., 2011. Post-common envelope binaries from SDSS-X: the origin of low-mass white dwarfs. *MNRAS*, **413**, 1121–1131.
- REDFIELD, S. & LINSKY, J. L., 2008. The Structure of the Local Interstellar Medium. IV. Dynamics, Morphology, Physical Properties, and Implications of Cloud-Cloud Interactions. *ApJ*, **673**, 283–314.
- REID, I. N., 2005. High-Velocity White Dwarfs and Galactic Structure. *ARA&A*, **43**, 247–292.
- REID, I. N., GIZIS, J. E. & HAWLEY, S. L., 2002. The Palomar/MSU Nearby Star Spectroscopic Survey. IV. The Luminosity Function in the Solar Neighborhood and M Dwarf Kinematics. *AJ*, **124**, 2721–2738.

- REID, I. N., SAHU, K. C. & HAWLEY, S. L., 2001. High-Velocity White Dwarfs: Thick Disk, Not Dark Matter. *ApJ*, **559**, 942–947.
- REIMERS, D. & KUDRITZKI, R. P., 1978. On the absolute scale of mass-loss in red giants. II. Circumstellar absorption lines in the spectrum of alpha Sco B and mass-loss of alpha Sco A. *Astron. & Astrophys.*, **365**, 227–239.
- RENEDO, I., ALTHAUS, L. G., MILLER BERTOLAMI, M. M., ROMERO, A. D., CÓRSICO, A. H., ROHRMANN, R. D. & GARCÍA-BERRO, E., 2010. New Cooling Sequences for Old White Dwarfs. *Astrophys. J.*, **717**, 183–195.
- RICHARDS, G. T., FAN, X. & NEWBERG, H. J. ET AL., 2002. Spectroscopic Target Selection in the Sloan Digital Sky Survey: The Quasar Sample. *AJ*, **123**, 2945–2975.
- RICKER, P. M. & TAAM, R. E., 2012. An AMR Study of the Common-envelope Phase of Binary Evolution. *ApJ*, **746**, 74.
- RIESS, A. G., FILIPPENKO, A. V., CHALLIS, P., CLOCCHIATTI, A., DIERCKS, A. ET AL., 1998. Observational Evidence from Supernovae for an Accelerating Universe and a Cosmological Constant. *AJ*, **116**, 1009–1038.
- ROWELL, N. & HAMBLY, N. C., 2011. White dwarfs in the SuperCOSMOS Sky Survey: the thin disc, thick disc and spheroid luminosity functions. *MNRAS*, **417**, 93–113.
- RUBIN, V. C., BURSTEIN, D., FORD, J. W. K. & THONNARD, N., 1985. Rotation velocities of 16 SA galaxies and a comparison of Sa, Sb, and SC rotation properties. *ApJ*, **289**, 81–98.
- RUBIN, V. C. & FORD, J. W. K., 1970. Rotation of the Andromeda Nebula from a Spectroscopic Survey of Emission Regions. *ApJ*, **159**, 379.
- RUBIN, V. C., FORD, W. K. J. & ROBERTS, M. S., 1979. Extended rotation curves of high-luminosity spiral galaxies. V - NGC 1961, the most massive spiral known. *ApJ*, **230**, 35–39.
- RUBIN, V. C., THONNARD, N. & FORD, J. W. K., 1977. Extended rotation curves of high-luminosity spiral galaxies. I - The angle between the rotation axis of the nucleus and the outer disk of NGC 3672. *ApJ*, **217**, L1–L4.
- SAHU, K. C., 1994. Stars Within the Large Magellanic Cloud as Potential Lenses for Observed Microlensing Events. *Nature*, **370**, 275.
- SALARIS, M., GARCÍA-BERRO, E., HERNANZ, M., ISERN, J. & SAUMON, D., 2000. The Ages of Very Cool Hydrogen-rich White Dwarfs. *ApJ*, **544**, 1036–1043.

- SALPETER, E. E., 1961. Energy and Pressure of a Zero-Temperature Plasma. *ApJ*, **134**, 669.
- SCALO, J., 1998. The IMF Revisited: A Case for Variations. In G. Gilmore & D. Howell, ed., *The Stellar Initial Mass Function (38th Herstmonceux Conference)*, vol. 142 of *Astronomical Society of the Pacific Conference Series*, 201–+.
- SCHLEGEL, D. J., FINKBEINER, D. P. & DAVIS, M., 1998. Maps of Dust Infrared Emission for Use in Estimation of Reddening and Cosmic Microwave Background Radiation Foregrounds. *ApJ*, **500**, 525–+.
- SCHMIDT, M., 1959. The Rate of Star Formation. *ApJ*, **129**, 243.
- SCHMIDT, M., 1968. Space Distribution and Luminosity Functions of Quasi-Stellar Radio Sources. *ApJ*, **151**, 393–+.
- SCHMIDT, M., 1975. The mass of the galactic halo derived from the luminosity function of high-velocity stars. *ApJ*, **202**, 22–29.
- SCHREIBER, M. R. & GÄNSICKE, B. T., 2003. The age, life expectancy, and space density of Post Common Envelope Binaries. *Astron. & Astrophys.*, **406**, 305–321.
- SERENELLI, A. M., ALTHAUS, L. G., ROHRMANN, R. D. & BENVENUTO, O. G., 2001. The ages and colours of cool helium-core white dwarf stars. *MNRAS*, **325**, 607–616.
- SILK, J., 2007. Galaxy Formation and Dark Matter. In L. Papantonopoulos, ed., *The Invisible Universe: Dark Matter and Dark Energy*, vol. 720 of *Lecture Notes in Physics*, Berlin Springer Verlag, 101–+.
- SION, E. M., BOHLIN, R. C., TWEEDY, R. W. & VAUCLAIR, G. P., 1992. The identification of highly ionized metal species in the hot DA1 white dwarf G191 - B2B with the Hubble Space Telescope faint object spectrograph. *ApJ*, **391**, L29–L32.
- SION, E. M., GREENSTEIN, J. L., LANDSTREET, J. D., LIEBERT, J., SHIPMAN, H. L. & WEGNER, G. A., 1983. A proposed new white dwarf spectral classification system. *ApJ*, **269**, 253–257.
- SMOLČIĆ, V., IVEZIĆ, Ž. & KNAPP, G. R. ET AL., 2004. A Second Stellar Color Locus: a Bridge from White Dwarfs to M stars. *ApJ*, **615**, L141–L144.
- STRAUSS, M. A., WEINBERG, D. H. & LUPTON, R. H. ET AL., 2002. Spectroscopic Target Selection in the Sloan Digital Sky Survey: The Main Galaxy Sample. *AJ*, **124**, 1810–1824.

- TAAM, R. E. & RICKER, P. M., 2010. Common envelope evolution. *New Astron. Rev.*, **54**, 65–71.
- TAKEUCHI, T. T., YOSHIKAWA, K. & ISHII, T. T., 2000. Tests of Statistical Methods for Estimating Galaxy Luminosity Function and Applications to the Hubble Deep Field. *ApJS*, **129**, 1–31.
- TISSERAND, P., LE GUILLOU, L., AFONSO, C., ALBERT, J. N., ANDERSEN, J. ET AL., 2007. Limits on the Macho content of the Galactic Halo from the EROS-2 Survey of the Magellanic Clouds. *A&A*, **469**, 387–404.
- TORRES, S., CAMACHO, J., ISERN, J. & GARCÍA-BERRO, E., 2008. The contribution of red dwarfs and white dwarfs to the halo dark matter. *A&A*, **486**, 427–435.
- TORRES, S., GARCÍA-BERRO, E., BURKERT, A. & ISERN, J., 2001. The impact of a merger episode in the galactic disc white dwarf population. *MNRAS*, **328**, 492–500.
- TORRES, S., GARCÍA-BERRO, E., BURKERT, A. & ISERN, J., 2002. High-proper-motion white dwarfs and halo dark matter. *MNRAS*, **336**, 971–978.
- TORRES, S., GARCÍA-BERRO, E. & ISERN, J., 1998. Neural Network Identification of Halo White Dwarfs. *ApJ*, **508**, L71–L74.
- TORRES, S., GARCÍA-BERRO, E. & ISERN, J., 2007. The white dwarf luminosity function - II. The effect of the measurement errors and other biases. *MNRAS*, **378**, 1461–1470.
- TORRES GIL, S., 2002. *Simulación Monte Carlo de la Población de Enanas Blancas de la Galaxia*. Ph.D. thesis, Universitat Politècnica de Catalunya.
- TOUT, C. A. & EGGLETON, P. P., 1988. Tidal enhancement by a binary companion of stellar winds from cool giants. *MNRAS*, **231**, 823–831.
- TREMBLAY, P.-E., BERGERON, P. & GIANNINAS, A., 2011. An Improved Spectroscopic Analysis of DA White Dwarfs from the Sloan Digital Sky Survey Data Release 4. *ApJ*, **730**, 128.
- UCHAIKIN, V. & ZOLOTAREV, V., 1999. *Chance and Stability: Stable Distributions and their applications*. De Gruyter.
- UDALSKI, A., KUBIAK, M., SZYMANSKI, M., KALUZNY, J., MATEO, M. & KRZEMINSKI, W., 1994. The Optical Gravitational Lensing Experiment. The Catalog of Periodic Variable Stars in the Galactic Bulge. I. Periodic Variables in the Center of the Baade’s Window. *Acta Astronomica*, **44**, 317–386.

- VAN HORN, H. M., 1968. Crystallization of White Dwarfs. *ApJ*, **151**, 227.
- VAN KERKWIJK, M. H., BASSA, C. G., JACOBY, B. A. & JONKER, P. G., 2005. Optical Studies of Companions to Millisecond Pulsars. In F. A. Rasio & I. H. Stairs, eds., *Binary Radio Pulsars*, vol. 328 of *Astronomical Society of the Pacific Conference Series*, 357.
- VASSILIADIS, E. & WOOD, P. R., 1993. Evolution of low- and intermediate- mass stars to the end of the asymptotic giant branch with mass loss. *Astrophys. J.*, **413**, 641–657.
- VENNES, S., SMITH, R. J., BOYLE, B. J., CROOM, S. M., KAWKA, A., SHANKS, T., MILLER, L. & LOARING, N., 2002. White dwarfs in the 2dF QSO Redshift Survey - I. Hydrogen-rich (DA) stars. *MNRAS*, **335**, 673–686.
- VIDRIH, S., BRAMICH, D. M., HEWETT, P. C., EVANS, N. W., GILMORE, G. ET AL., 2007. New ultracool and halo white dwarf candidates in SDSS Stripe 82. *MNRAS*, **382**, 515–525.
- WEBBINK, R., 2007. Overview of Outcomes from White Dwarf Mergers. In *Paths to Exploding Stars: Accretion and Eruption*.
- WEBBINK, R. F., 1984. Double white dwarfs as progenitors of R Coronae Borealis stars and Type I supernovae. *ApJ*, **277**, 355–360.
- WEBBINK, R. F., 2008. Common Envelope Evolution Redux. In E. F. Milone, D. A. Leahy & D. W. Hobill, eds., *Astrophysics and Space Science Library*, vol. 352 of *Astrophysics and Space Science Library*, 233.
- WEIDNER, C. & KROUPA, P., 2006. The maximum stellar mass, star-cluster formation and composite stellar populations. *MNRAS*, **365**, 1333–1347.
- WEST, A. A., 2011. Low-Mass Stars in the Sloan Digital Sky Survey. In *American Astronomical Society Meeting Abstracts #218*, 306.01.
- WEST, A. A., HAWLEY, S. L., BOCHANSKI, J. J., COVEY, K. R., REID, I. N., DHITAL, S., HILTON, E. J. & MASUDA, M., 2008. Constraining the Age-Activity Relation for Cool Stars: The Sloan Digital Sky Survey Data Release 5 Low-Mass Star Spectroscopic Sample. *AJ*, **135**, 785–795.
- WILLEMS, B. & KOLB, U., 2004. Detached white dwarf main-sequence star binaries. *A&A*, **419**, 1057–1076.
- WINGET, D. E., HANSEN, C. J., LIEBERT, J., VAN HORN, H. M., FONTAINE, G., NATHER, R. E., KEPLER, S. O. & LAMB, D. Q., 1987. An independent method for determining the age of the universe. *ApJ*, **315**, L77–L81.

- WOOD, M. A. & OSWALT, T. D., 1998. White Dwarf Cosmochronometry. I. Monte Carlo Simulations of Proper-Motion- and Magnitude-limited Samples Using Schmidt's $1/V$ max Estimator. *ApJ*, **497**, 870.
- YANNY, B., ROCKOSI, C., NEWBERG, H. J., KNAPP, G. R., ADELMAN-McCARTHY, J. K. ET AL., 2009. SEGUE: A Spectroscopic Survey of 240,000 Stars with $g = 14$ -20. *AJ*, **137**, 4377–4399.
- ZHAO, H., 1998. Microlensing of tidal debris on the Magellanic great circle. *MNRAS*, **294**, 139.
- ZOROTOVIC, M., SCHREIBER, M. R., GÄNSICKE, B. T. & NEBOT GÓMEZ-MORÁN, A., 2010. Post-common-envelope binaries from SDSS. IX: Constraining the common-envelope efficiency. *A&A*, **520**, A86.
- ZOROTOVIC, M., SCHREIBER, M. R., GÄNSICKE, B. T. & REBASSA-MANSERGAS, A. ET AL., 2011. Post common envelope binaries from SDSS. XIII. Mass dependencies of the orbital period distribution. *A&A*, **536**, L3.
- ZUCKERMAN, B., KOESTER, D., REID, I. N. & HÜNSCH, M., 2003. Metal Lines in DA White Dwarfs. *ApJ*, **596**, 477–495.
- ZWICKY, F., 1933. Die Rotverschiebung von extragalaktischen Nebeln. *Helvetica Physica Acta*, **6**, 110–127.
- ZWICKY, F., 1937. On the Masses of Nebulae and of Clusters of Nebulae. *ApJ*, **86**, 217.